Computationally Efficient Extended and Stabilized Finite Element Methods for Multiphase Carbon Sequestration Modelling

by

Chris Ladubec

A thesis

presented to the University of Waterloo

in fulfilment of the

thesis requirement for the degree of

Doctor of Philosophy

in

Civil Engineering

Waterloo, Ontario, Canada, 2016

Author's Declaration

I hereby declare that I am the sole author of this thesis. This is a true copy of the thesis, including any required final revisions, as accepted by my examiners.

I understand that my thesis may be made electronically available to the public.

Abstract

Carbon sequestration in deep saline aquifers has been proposed for long term storage of CO_2 as an alternative to the release of CO_2 into the atmosphere. In this thesis a computationally efficient numerical model that describes the physics of CO_2 injection into deep saline aquifers is presented. The model is based on the multiphase flow and vertically averaged mass balance equations, requiring the solution of two coupled, non-linear partial differential equations - a pressure equation and a saturation equation. The numerical formulation is based on sequentially coupled Finite Element Methods (FEMs). The Finite Difference Method (FDM) is used to discretize in time. The saturation equation is a non-linear advective equation for which the application of Galerkin Finite Element Method (FEM) can lead to non-physical oscillations in the solution.

Several stabilized methods are considered to control the oscillations that occur as a by-product of the approximation of the saturation equation. The methods developed are based on the the Streamline Upwind (SU) method, the Streamline Upwind Petrov Galerkin (SUPG) method, the Galerkin Least Squares (GLS) method, the Subgrid Scales (SGS) method, and the Least Squares Finite Element Method (LSFEM). Two sequential solution schemes are applied: a single step (SS) and a predictor-corrector (PC). The range of Courant numbers yielding smooth and oscillation-free solutions is investigated for each method. The useful range of Courant numbers depends upon both the sequential scheme

(SS vs PC) and also the time integration method used (Forward Euler, Backward Euler, or Crank-Nicolson). For complex problems such as when two plumes meet, only the SU stabilization with an amplified stabilization parameter (SU-8τ) gives satisfactory results when large timesteps are used.

The use of linear elements results in the omission of the second order term in the SUPG and LSFEM residuals. In addition, part of the perturbation operator for LSFEM also disappears. This loss of information may affect the stabilization properties of the SUPG and LSFEM methods. When linear elements are used, SUPG, GLS and SGS all result in the same formulation. Quadratic elements allow for GLS and SGS stabilizations, and permit more complete forms of SUPG and LSFEM stabilizations. The results show that SGS, GLS and SU-8τ (SU with an amplified value of the stabilization parameter) are the most robust stabilization methods considered. SGS and GLS are the preferred choice at small timesteps, and SU-8τ is the most suitable for relatively large timesteps. Quadratic elements are shown to better handle the case of merging CO_2 plumes compared with linear elements, but quadratic elements experience greater oscillations when encountering a Dirichlet boundary.

The proposed formulation is compared against an existing benchmark study where eleven different simulators were used to determine the arrival time of the CO_2 at a leaky well. Four examples consider non-uniform permeability, multiple injection wells, an upsloping aquifer, and a dome shaped aquifer. A new adaptive timestep strategy is implemented which allows stable solutions with increasing timesteps as time progresses. The adaptive timesteps reduce the computational cost by 75-82 % compared to constant timesteps in the four examples shown.

The eXtended Finite Element Method (XFEM) is introduced to accurately approx-

imate near-injection well pressure behaviour with elements significantly larger than the injection well diameter. A vertically averaged multiphase flow model is presented that combines XFEM to approximate the pressure field, with a Streamline Upwind/Finite Element/FDM (SU-FEM-FDM) to approximate the distribution of CO_2 in the aquifer. Near-well enrichment functions are presented along with the solution procedure for the coupled problem. Two examples are presented; in the first, CO_2 injection into a perfectly horizontal aquifer is modelled with both XFEM and FEM-based methods. The results suggest that XFEM is able to provide low relative errors in the pressure near the well at a reduced computational cost compared to FEM. The impact and selection of the stabilization coefficient of the SU-FEM-FDM is also discussed. In the second example, the XFEM and SU-FEM-FDM models are applied to a more realistic problem of an inclined aquifer to demonstrate the ability of the model to capture the buoyancy driven migration of CO_2 in a deep saline aquifer.

Acknowledgements

I would like to thank my supervisor, Dr. Robert Gracie, for his continued support and encouragement. I would also like to thank the committee for reviewing my thesis. I also want to acknowledge support from the Natural Sciences and Engineering Research Council (NSERC), NSERC Discovery Grant, NSERC-Network of Centres of Excellence-Carbon Management Canada, and the Ontario Graduate Scholarship (OGS).

Dedication

Dedicated to my loving and patient wife, Robilyn and our wonderful son James.

Table of Contents

List of Figures

List of Tables

List of Abbreviations

CCS - Carbon Capture and Storage

FEM - Finite Element Method

FDM - Finite Difference Method

FVM - Finite Volume Method

XFEM - eXtended Finite Element Method

IMPES - IMplicit Pressure Explicit Saturation method

CN - Crank-Nicolson method

FE - Forward Euler method

BE - Backward Euler method

LSFEM - Least Squares Finite Element Method

SU - Streamline Upwind method

SUPG - Streamline Upwind Petrov Galerkin method

GLS - Galerkin Least Squares method

SGS - Subgrid Scales method

SS - Single Step sequential solution

PC - Predictor-Corrector sequential solution

List of Symbols

ϕ - porosity of aquifer

S^B_{RES} - residual saturation of brine

h_B - depth of brine

h_C - depth of CO_2

ρ_B - density of brine

ρ_C - density of CO_2

$\Delta\rho$ - density difference between brine and CO_2

z_{top} - depth of the top boundary of aquifer

z_{bot} - depth of the bottom boundary of aquifer

p_{bot} - pressure at the bottom of the aquifer

H - thickness of the aquifer

k - permeability

κ - hydraulic conductivity

k^C_{rel} - relative permeability of CO_2 compared to brine

μ_B - dynamic viscosity of brine

μ_C - dynamic viscosity of CO_2

a - advective velocity

v - diffusion coefficient

σ -reaction term

q_C^{inj} - injection rate of CO_2

u - general unknown

$\dot{u}$ - time rate of change of u

x - longitudinal direction

y - lateral direction

z - downward direction

ρ - density

m - mass

V - volume

V_{voids} - volume of voids

V_{matrix} - volume of solid matrix

V_{rock} - volume of rock (matrix and voids)

g - gravitational constant

μ - dynamic viscosity

ϕ - porosity

h - hydraulic head

f - Neumann boundary condition

$\hat{\mathbf{q}}_\mathbf{B}$ - vertically averaged brine flux

$\hat{\mathbf{q}}_\mathbf{C}$ - vertically averaged CO_2 flux

$\overline{\mathbf{q}}_\mathbf{B}$ - Neumann boundary, where brine flux is specified

$\overline{\mathbf{q}}_\mathbf{C}$ - Neumann boundary, where CO_2 flux is specified

Γ_p - Dirichlet boundary, where pressure is specified

Γ_q - Neumann boundary, where total flux is specified

Γ_h - Dirichlet boundary, where depth of brine is specified

Γ_D - Dirichlet boundary

Γ_N - Neumann boundary

h_o - initial brine depth

Ω - domain

δu - weight (test) function

δh_B - weight (test) function

δp_{bot} - weight (test) function

H^1 - Hilbert space

U - function space

W - function space

u_D - prescribed value of unknown quantity u at Dirichlet boundary Γ_D

u_t - time rate of change of u

s - source term

Cr - Courant number

Pe - Peclet number

D - Damkohler number

∇ - gradient operator

$\nabla\cdot$ - divergence operator

Δ - denotes a difference between two quantities

$\mathbf{N}$ - matrix of Finite Element shape functions

$\mathbf{B}$ - matrix of the spatial derivatives Finite Element shape functions

$P()$ - perturbation function for stabilized FEMs

$R()$ - residual

τ - stabilization parameter

$\mathbf{C}$ - mass or storage matrix

$\mathbf{K}$ - diffusion or advection matrix

$\mathbf{F}$ - flux Vector

$\mathbf{K_{eff}}$ - effective advection matrix

$\mathbf{F_{eff}}$ - effective flux vector

α - well number

r_α - radius of well α

r_w - radius of well

$\overline{p}_{\alpha,j}$ - enriched degrees of freedom

I - standard degree of freedom counter

J - enriched degree of freedom counter

$\overline{\mathbf{N}}$ - matrix of enriched shape functions

$\overline{p}$ - vector containing enriched degrees of freedom

$\overline{\mathbf{F}}$ - enriched flux vector

$\mathbf{K_{aquifer}}$ - diffusion matrix for the eXtended Finite Element Method

$\overline{\mathbf{K}}$ - enriched diffusion matrix

$\overline{\overline{\mathbf{K}}}$ - enriched diffusion matrix

$\mathcal{N}$ - set of all nodes

$\mathcal{S}_\alpha$ - set of nodes in enriched domain for well α

$\overline{\mathbf{B}}$ - matrix of derivatives of enriched shape functions

$\psi_\alpha(\mathbf{x})$ - enrichment function of well α

Chapter 1

Introduction to Carbon Sequestration and Objectives

1.1 Carbon Capture and Storage (CCS)

Carbon Dioxide (CO_2) is a greenhouse gas that is widely understood to contribute to global warming, which has become a significant international issue. Fossil fuels, when combusted, release large amounts of greenhouse gases which trap heat in the atmosphere and cause an increase in the average global temperature. As worldwide use of fossil fuels continues to grow, so do the emissions of CO_2. Global warming will continue to induce climate change unless the release of greenhouse gases into the atmosphere is reduced.

An intergovernmental panel (IPCC) produced a study [2] examining the problem of global warming. It determined that immediate action is necessary to reduce CO_2 emissions. In 2005, global CO_2 emissions associated with use of fossil fuels were 26 gigatons per year and without a unified effort, over 9,000 gigatons were projected to be released over the next century [1]. In order to slow climate change CO_2 emissions must be significantly reduced. This requires a large scale reduction in the amount of CO_2 released

into the atmosphere [1]. There are three main ways that emissions can be reduced [2]: improved fuel efficiency; development of reduced carbon footprint energy sources; and carbon capture and storage (CCS).

Improving fuel efficiency seeks to find ways to do more work with less energy. For example, cars are made more fuel efficient by reducing their weight, improving aerodynamics and improving the efficiencies of engines. Climate change presents an incentive for the development of technologies which harness renewable sources of energy. In order to decrease the global dependence on fossil fuels, achieving a portfolio of dependable renewable energy sources is paramount. Wind energy, solar energy and geothermal energy are continually replenished and, if exploited, offer an alternative to burning fossil fuels. Unfortunately, technologies which harness these sources generally lack the efficiency required to produce massive quantities of energy in a cost effective manner. Further development is required to make these technologies competitive with fossil fuels.

Carbon capture and storage (CCS) provides a method to dispose of the CO_2 emissions created during fossil fuel use. A thorough overview of CCS can be found in [9]. A schematic of the CCS process is shown in Figure 1.1. In this example, a power plant creates CO_2 emissions which are separated from the flue gas. The CO_2 is then compressed, and sent by pipeline to the injection site. At the injection site the CO_2 is pumped into the injection zone. The injection well is monitored and sealed to prevent leakage. CCS focuses on large volume emitters, since it is more feasible to capture and store CO_2 from a few large sources (i.e., stationary point sources) than many smaller ones. Power generation is the largest emitter of CO_2 [2]. Coal power plants are ideal for CCS because the source is localized, which facilitates capture of the CO_2. Before the carbon can be stored or sequestered it must be separated from flue gas. Once the CO_2 has been captured it is

then transported to the injection site, where it is compressed and injected below the ground in a process known as carbon sequestration.

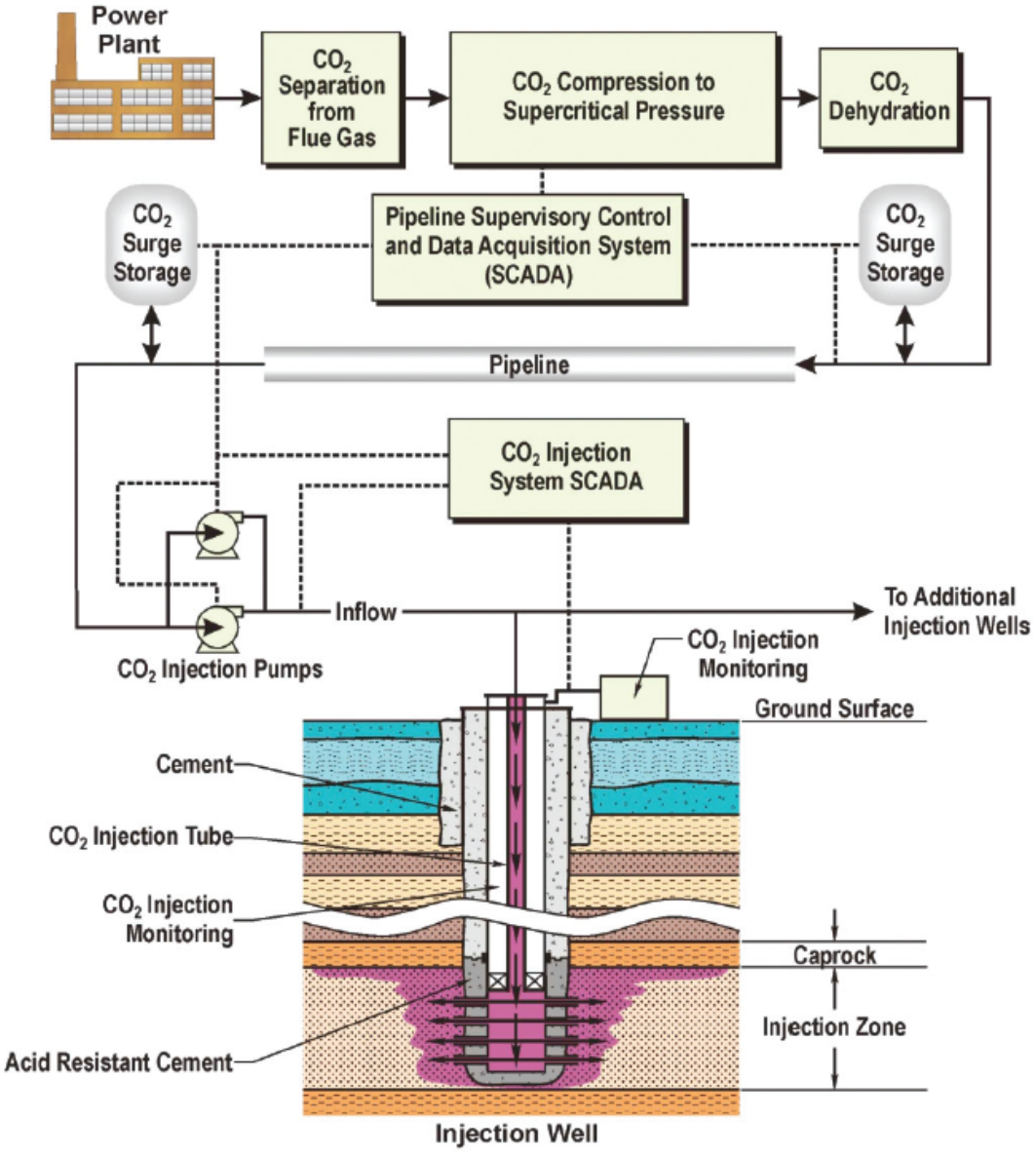

Figure 1.1: Overview of CCS process [1].

Carbon capture and storage is an expensive undertaking. There are three main components of CCS: capture, transport and sequestration (storage). In order to assess the feasibility of CCS the economics must be considered. There are four major costs to CCS [10]: capture ($30-50 per tonne CO_2); compression ($8-10 per tonne CO_2); transportation ($0.70-4 per tonne CO_2 per km); and injection ($2-8 per tonne CO_2). The largest cost

associated with CCS is the capture process. Therefore CCS can be made much more economical and viable if significant progress is made in technologies that can capture the CO_2 from the flue gas in a more economical way than current technology allows.

1.2 Carbon Sequestration

There are several potential storage possibilities for the carbon dioxide (CO_2), which can be categorized into three main groups [10]: biosphere sinks; material sinks; and geosphere sinks. Biosphere sinks are where the CO_2 is stored in natural systems (e.g., oceans, forests and soils). Material sinks are where the CO_2 is used to produce materials (wood products, chemicals, plastic). In geosphere sinks, the CO_2 is stored in geological structures (e.g., depleted oil reservoirs, coal beds, deep saline aquifers).

Geological structures provide several important options for carbon sequestration (as shown in Figure 1.2) including [2]: injection into old depleted oil and gas reservoirs; deep unmineable coal seams; deep saline aquifers; or use during enhanced oil or methane recovery. While many options for CO_2 storage exist, deep saline aquifers appear to present the most potential. A thorough overview of carbon sequestration in geological structures can be found in [11].

Deep saline aquifers are composed of porous rock such as sandstone and initially contain brine (salt water). The resident brine is displaced when the CO_2 is injected. These aquifers are promising due to the large potential capacity to store CO_2 and the potential for long term storage. Figure 1.3 shows the capacity of storage in deep saline aquifers that is estimated to be available globally. It can be seen that much of the total global availability of this storage space is concentrated in North America.

Deep saline aquifers considered for CO_2 storage are greater than 800 m below the

ground level [12]. Excellent review articles on carbon sequestration in deep saline aquifers are found in [13, 14]. The temperature at these depths is typically 35 $^{\circ}C$ or higher. Under the pressures and temperatures that occur at these depths, the CO_2 is in a supercritical state. When CO_2 exists as a supercritical fluid it can exhibit properties of both a gas and a liquid. As the host aquifers contain a brine solution, the interaction of the supercritical CO_2 and the resident brine solution results in multiphase flow. The supercritical CO_2 is less dense than the host brine, and thus there will be a buoyancy drive causing the CO_2 to rise and float on top of the brine.

Ideal deep saline aquifers have an impermeable caprock above to prevent the CO_2 from leaking into overlaying aquifers. The locations that are ideal for deep saline storage of CO_2 typically happen to be the same areas that have been heavily drilled by the oil and gas industry, so there are many abandoned wells that act as possible leakage pathways.

The horizontal dimensions of the aquifer can be measured in kilometres, while the thickness of these aquifers is typically of the order of tens of metres. The large difference in scale between the horizontal and vertical dimensions permits the use of vertically averaged governing equations to study these systems. A second significant difference in scale exists between the horizontal dimensions of the aquifer and the diameters of injection wells (and leaky wells). Therefore, prohibitively fine spatial discretizations must be used near these wells to capture the large pressure gradients when traditional numerical methods are used.

CO_2 is injected at pressures that are below the fracture pressure of the formation to avoid inducing fractures. If vertical fractures are created, they present pathways through which the CO_2 (or brine) can migrate vertically and contaminate other aquifers. When injecting near faults, it is crucial to determine safe injection pressures that will not cause fault reactivation [15, 16]. CO_2 is injected at temperatures that are much colder than the

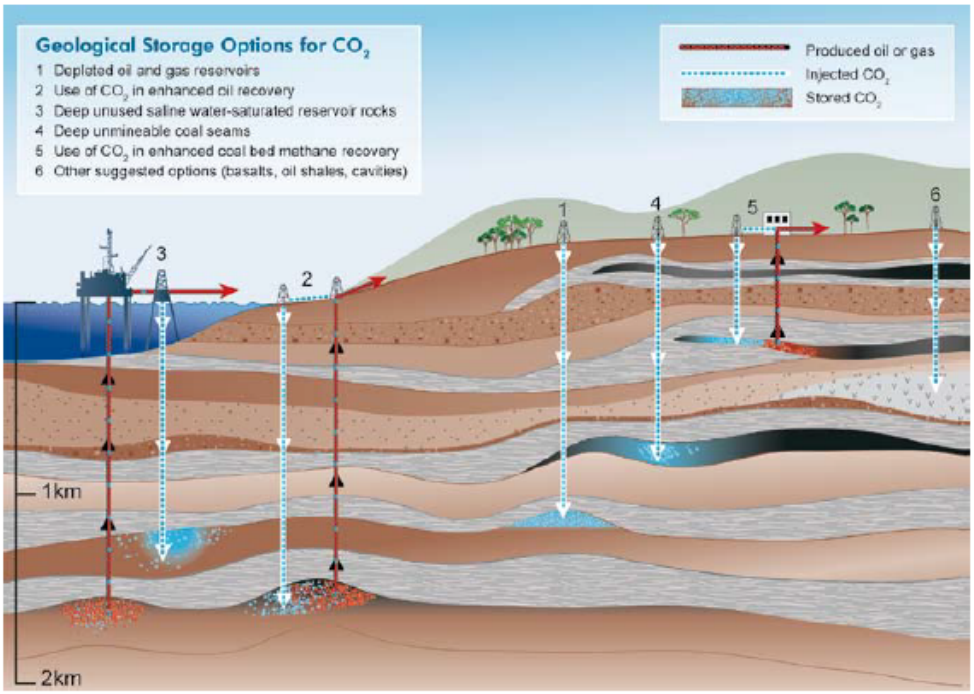

Figure 1.2: Options for geological storage of CO_2 [2].

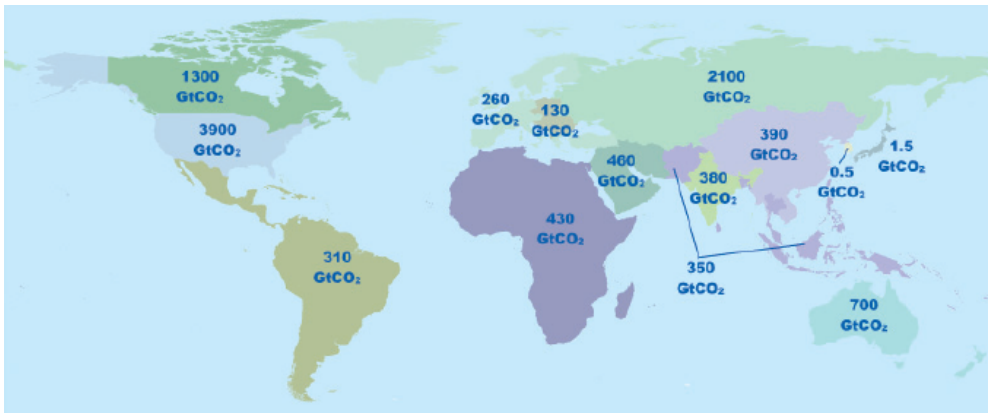

Figure 1.3: Estimated global CO_2 storage capacity [1].

formation fluids. This can contribute to the creation or reactivation of existing fractures in the caprock.

One of the key hazards of carbon sequestration is the CO_2 (or brine) migrating out of the storage aquifer. The density difference between the CO_2 and the brine create a buoyancy drive that forces the CO_2 upward. If the CO_2 plume encounters leakage pathways, the CO_2 can migrate out of the storage aquifer and potentially contaminate drinking water aquifers, or leak to the surface. If CO_2 contaminates the groundwater

above, it can result in acidification of the groundwater. Should the CO_2 reach the surface, it can present a suffocation hazard since air is less dense than CO_2.

As the carbon dioxide plume expands, many physical processes occur, and many leakage pathways may be encountered. Before CO_2 sequestration is implemented at a particular site, the potential for leakage must be properly understood, analysed and quantified. The risks involved need to be properly assessed in order to select sites for CO_2 sequestration, and to design safe injection procedures. The importance of understanding and mitigating against risk cannot be understated, as this underlies the feasibility of large scale CO_2 sequestration.

The CO_2 can propagate upward to reach above aquifers, and possibly ultimately the surface of the earth. There are several potential leakage pathways for the upward migration of CO_2. Three of the possible leakage pathways are: diffusion through caprock; migration through faults and fractures; and migration through abandoned oil and gas wells.

Figure 1.4 illustrates the leakage scenario through abandoned oil and gas wells. As the CO_2 is injected the plume rises above the resident brine solution. As the plume migrates updip a leakage pathway in the form of an abandoned well is encountered. The CO_2 travels through leakage pathways in the abandoned well driven by a buoyancy force. The low viscosity of the supercritical CO_2 makes it easier to travel through the pathways. As the CO_2 travels upward through the abandoned well, some of the CO_2 enters the aquifer above and spreads out. The remaining CO_2 continues upward and can enter the aquifers above in a similar process. Eventually some of the CO_2 may reach the surface.

Although abandoned wells are plugged, there are still several potential leakage pathways through which the CO_2 may migrate upward. Figure 1.5 shows that leakage may

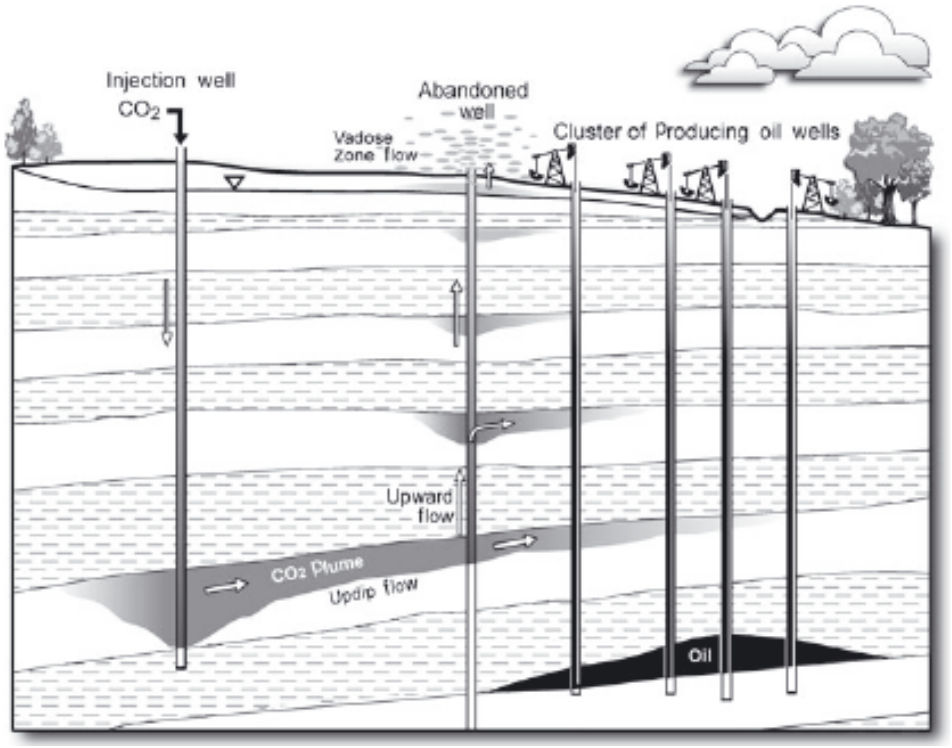

Figure 1.4: CO_2 injection and leakage [3].

occur through any of several pathways: a) between well casing and cement fill; b) between well casing and well plug; c) through the well plug; d) through the well casing; e) through cement fill; and f) between the cement fill and the ground. A small amount of the CO_2 may dissolve in the brine which can create an acidic solution that may degrade the cements in plugged wells.

1.2.1 Importance of Computational Efficiency

There is a large degree of uncertainty associated with carbon sequestration including: location and number of abandoned wells; leakage characteristics of abandoned wells; and formation properties such as porosity and permeability. As a consequence of the large uncertainties involved, stochastic methods must be used to assess potential sites. One of the most widely used of these methods is the Monte Carlo approach. In the Monte Carlo approach unknown parameters are assigned likelihood distributions. The governing

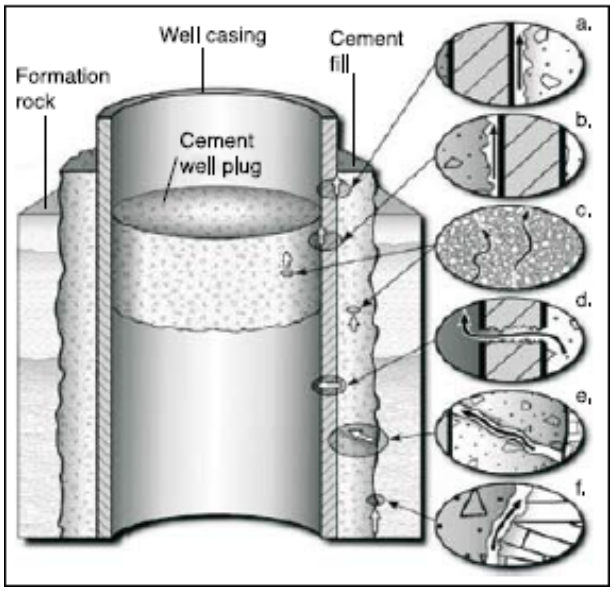

Figure 1.5: Leakage pathways through a plugged abandoned well [2].

equations are solved many times, each time with a set of parameters that is randomly sampled from assumed distributions of the uncertain parameters. For each set of randomly chosen parameters, the output is computed. This is repeated many times, and the result is a probability distribution for the unknown values. Since the calculations in this approach are repeated thousands of times it is necessary to have computationally efficient numerical techniques to model the carbon sequestration system. In addition to the uncertainty, carbon sequestration models involve very large domains (km^2) which require a large number of degrees of freedom, especially when near-well behaviour is important.

1.2.2 Solution Approaches

Efficiently modelling leakage in CO_2 sequestration requires the selection of the right approach. There are four main approaches that are found in the literature to studying injection and plume evolution in CO_2 sequestration systems: analytical; numerical; hybrid; and semi-analytical.

Analytical solutions provide very computationally efficient, accurate solutions. While

they are very efficient and accurate they are typically limited to simple cases. Analytical solutions can be useful for studying large scale injection and transport in addition to modelling flow through a single well. Analytical solutions that are applicable to studying leakage in a carbon sequestration system can be found in [17, 18, 19, 20, 21, 22, 23, 24, 25, 26, 27, 28, 29, 30, 31, 32, 33].

Most practical problems, however, are too complicated to be amenable to analytical solution, thus numerical solutions are usually the approach of choice. References [34] and [35] provide good introductions to numerical methods. Numerical methods suffer from the drawback of being computationally expensive.

Semi-analytical solutions have also been used recently with success. Semi-analytical solutions use analytical methods to solve for the spatial solutions, however, the solutions are stepped through time numerically. This type of approach can be very computationally efficient for many cases. The usefulness of semi-analytical solutions was demonstrated in [36, 37].

Hybrid solutions have also been used to study CO_2 leakage. In this class of methods numerical methods are used to calculate large scale flows. The analytical solutions are then applied locally (e.g., to correct for localized injection pressures or abandoned well leakage) using an analytical solution. For many problems, computational efficiency can be greatly improved over numerical solutions using hybrid solutions [38].

Analytical, semi-analytical, and hybrid solutions are typically more computationally efficient than numerical solutions, however, numerical solutions are still generally required to handle heterogeneity, anisotropy, irregular boundaries and other complexities in carbon sequestration systems. Two of the most common numerical methods for PDEs are the Finite Element Method (FEM), and the Finite Difference Method (FDM). While both

methods are often appropriate to discretize in space, the FEM has the advantage that it is able to handle complex geometries easily. FDM is often used to discretize in time. Many numerical models have been used in the literature to study carbon sequestration including [39, 40, 41, 42, 43, 44, 45, 46, 47]. Numerical solutions are described in more detail in the next sections.

1.3 The Finite Difference Method (FDM)

The Finite Difference Method (FDM) is a common approach to solving partial differential equations (PDEs) [48]. Difference equations are substituted into the strong form (original PDE) of the governing equations to obtain the discretization. FDM has been used as the main spatial and temporal discretization method in carbon sequestration modelling (e.g., [38, 41]). FDM is also commonly used in combination with FEM, where FEM is used to discretize space and FDM is used to discretize time.

1.4 The Finite Element Method (FEM)

The Finite Element Method (FEM) is another numerical method to solve PDEs. It is a very versatile approach that can be used to solve a wide variety of PDEs. The FEM has been successfully applied to many problems in mechanics, including: stress analysis, thermal analysis, seismic analysis, crash analysis, fluid flow analysis, and electromagnetic analysis [49]. A large selection of resources are available on the topic of FEM including [49, 50, 51, 52, 53, 54].

FEM generally uses simple functions such as polynomials to locally construct approximate solutions throughout the domain. The same shape functions are often used as

weight functions. This is the Galerkin Finite Element Method (FEM). Linear or quadratic elements in one dimension or bilinear or biquadratic elements in two dimensions are frequently used. The Finite Element Method begins with the weak form of the governing partial differential equation that is to be solved. This differs from the Finite Difference Method, which works with the strong form of the PDE. To obtain the weak form, the strong form is multiplied by a test function and integrated over the domain. Then Green's formula is used to reduce the highest order derivative of the results. FEM is able to handle irregular boundaries, unlike FDM, which generally has the restriction of regular boundaries. To the author's knowledge, no Finite Element Method has been described in literature which solves the vertically averaged multiphase flow equations described in this thesis. A general framework for these equations is developed with the Finite Element Method (FEM) and is described in Chapter 4, Chapter 5 and Chapter 6.

1.4.1 The eXtended Finite Element Method (XFEM)

The horizontal dimensions of the aquifers are measured in kilometers, but the diameter of the injection wells is measured in centimeters. To accurately resolve the pressure field and the pressure dependant leakage flux in the vicinity of an injection or abandoned well using traditional numerical methods would require a prohibitively fine discretization near the well.

XFEM has been widely used to model crack propagation (e.g., [55, 56]). XFEM has also been used to model interfaces (e.g., [57]). In addition, XFEM has been used to model point source injections and leaky wells in single phase simulations for carbon sequestration in [45, 46, 58]. The pressure distribution near wells was shown to be accurately resolved near wells using a coarse mesh. A more complete description of XFEM, with particular

focus on point source singularities, is presented in Chapter 6.

1.5 Objectives

The objectives of this thesis are:

1. Develop a computationally efficient numerical model for carbon sequestration based on a Finite Element Method framework using a vertically averaged formulation (Chapter 4).

2. Effectively deal with instabilities and oscillations that occur from FEM approximations of the advection equation and the coupled nature of this problem (Chapter 4).

3. Compare the developed numerical model with a benchmark problem from existing literature (Chapter 5).

4. Reduce the computational cost of carbon sequestration injection simulations by using adaptive timesteps (Chapter 5).

5. Improve the approximation of the pressure singularity due to the injection of CO_2 using XFEM (Chapter 6).

Chapter 2 provides a review of relevant concepts related to modelling flow in porous media, with a focus on carbon sequestration. It also discusses solution techniques for coupled models. Chapter 3 considers the oscillations that can occur when numerical modelling of an advection term. Stabilized Finite Element Methods are introduced and compared using one dimensional elements. These stabilized FEMs will be examined further in the context of coupled numerical models for carbon sequestration. Chapter 4

addresses objectives one and two and develops a framework based on FEM to solve the governing equations for vertically averaged multiphase flow. Several stabilized FEMs are considered to handle the numerical oscillations that occur in the numerical solution of the problem. Both linear and quadratic stabilization methods are considered and compared. Conclusions are drawn about the conditions where certain stabilization methods are preferred. A stabilization approach is identified as offering stable solutions across the widest range of conditions. In addition, this solution strategy offers consistently stable solutions with large timesteps. Chapter 5 addresses objectives three and four. The developed FEM framework is compared to a benchmark problem which compares several other numerical simulators. The computational cost of the solution strategy is further improved by using adaptive timesteps that allow larger timesteps as the simulation progresses. Chapter 6 addresses objective five by using the eXtended Finite Element Method (XFEM) to allow improved approximations of the pressure singularity at an injection well. This yields improved accuracy in the vicinity of wells, even with coarse spatial discretizations. Finally, Chapter 7 provides the major conclusions from the thesis and concludes with suggestions for future work.

Chapter 2

Numerical Modelling of Flow In Porous Media

2.1 Introduction

In this chapter the theoretical framework for modelling flow in porous media is presented. The chapter begins by explaining some basic concepts related to flow in porous media. First, the case of single phase flow is considered. Once the essential concepts of single phase flow are presented, the discussion moves to multiphase flow. In this case two fluids (or phases) are present in the porous medium. The chapter concludes with a description of vertically averaged multiphase flow. This concept is useful to reduce the dimensionality of multiphase flow problems, resulting in a more computationally efficient framework that can be successfully used to study carbon sequestration problems.

The remainder of this thesis is based on the following assumptions [3]:

- no rock deformation;
- laminar flow;
- incompressibility of CO_2 and brine;

- hydrostatic pressure distribution;
- constant relative permeability;
- constant viscosities;
- sharp interface between the brine and CO_2;
- no capillary pressure at the interface.

2.2 Single Phase Flow

2.2.1 Basic Concepts

This section discusses some essential key ideas related to flow in porous media. The governing equations of single phase flow are presented at the end of this section. The topic of flow in porous media is covered by many sources including [59], [60] and [61].

Representative Elementary Volume

A porous medium is actually composed of microscopic pores. In order to make the analysis tractable a continuum approach is used. A representative elementary volume (REV) is the smallest volume that has the same properties of interest as the whole volume. Multiple measurements of properties over the whole volume of samples the size of an REV should give the same results. The concept of an equivalent porous media (EPM) is used to model flow in fractured porous media using the concept of a continuum. An REV is required so that the flow can be modelled as a porous medium. For a thorough treatment of this top refer to [60].

Porosity

The porosity is a measure of the void space of the rock matrix. The porosity is calculated by:

$$\phi = \frac{V_{voids}}{V_{rock}} \tag{2.1}$$

where ϕ is the porosity of the rock, V_{voids} is the volume of void space, and V_{matrix} is the volume of the solid portion of rock matrix and $V_{rock} = V_{voids} + V_{matrix}$ is the total rock volume.

Density

The density of a fluid is the amount of mass in a given volume:

$$\rho = \frac{m}{V} \tag{2.2}$$

where ρ is the density of the fluid, m is the the mass of the fluid, and V is the volume of the fluid.

Permeability

The permeability (k) of an aquifer is a measure the aquifers abililty to allow fluid to flow through it. Permeability values can range vary across many orders of magnitude, for example from $10^{-20}\ m^2$ for shale to $10^{-13}\ m^2$ for sandstone [62].

Hydraulic Conductivity

Hydraulic conductivity is the ability of a fluid to flow through a given aquifer. This property depends on both the porous media and the fluid. Values can range vary across many

orders of magnitude, for example from 10^{-13} m/s for shale to 10^{-6} m/s for sandstone [62]. The hydraulic conductivity is calculated by:

$$\kappa = \frac{k\rho g}{\mu} \tag{2.3}$$

where k is the permeability of the aquifer, ρ is the density of the fluid, g is the gravitational constant, and μ is the dynamic viscosity of the fluid.

Dynamic Viscosity

The dynamic viscosity μ is a measure of the internal resistance of a fluid (or gas) to flow. The higher the dynamic viscosity, the greater the resistance. Air, for example has a much lower dynamic viscosity than water, which has a dynamic viscosity lower than honey.

2.2.2 Governing Equations

The governing equations for three dimensional porous media flow arise from the conservation of mass combined with Darcy's law. The conservation of mass of the system is expressed by the following differential equation:

$$\frac{\partial \rho\phi}{\partial t} + \nabla \cdot (\rho \mathbf{a}) = s \tag{2.4}$$

where $\mathbf{a}$ is the seepage velocity of the fluid, and s is a source term.

Darcy's Law is used to determine the fluid flux expressed as volumetric flow per unit matrix area. based on the gradient of the hydraulic head. Darcy's law can be written as:

$$\mathbf{q} = -\kappa \nabla h \tag{2.5}$$

where $\mathbf{q}$ is the flux (m/s), κ is the hydraulic conductivity (m^2), and h is the hydraulic head (m) The hydraulic head is given by:

$$h = \frac{p}{\rho g} + z \tag{2.6}$$

Substituting (2.3) and (2.6) into (2.5) gives:

$$\mathbf{q} = -\frac{\mathbf{k}}{\mu}(\nabla p + \rho g \nabla z) \tag{2.7}$$

Darcy's law is valid for laminar flow. When the Reynold's number is greater than 10 the validity of Darcy's law may be questionable [60].

2.3 Multiphase Flow

Injection of CO_2 into a brine-filled aquifer can be modelled by the governing equations for multiphase flow through porous media. This section builds upon the previous section to describe multiphase flow in porous media. First a few basic definitions are given, then the governing equations are presented.

2.3.1 Basic Concepts

Capillary Pressure

The capillary pressure is the pressure differential at the interface of two immiscible fluids such as water and air or water and CO_2. In carbon sequestration, for example, the interaction between brine and CO_2 is often of interest, in which case the capillary pressure

is given by:

$$p_{cap} = p_C - p_B \tag{2.8}$$

where p_C and p_B are the pressures along the interface in the CO_2 and brine respectively.

Relative Permeability

The relative permeability, k^C_{rel}, is the relative permeability of CO_2 relative to brine. If $k^C_{rel} = 1$ then effective permeability of the rock is the same for brine and CO_2.

Residual Saturation

When the CO_2 arrives and displaces the brine a certain amount of brine remains left behind. This is referred to as the residual brine saturation (S^B_{res}). On the other hand, when CO_2 is left behind, this is referred to as residual CO_2 saturation.

2.3.2 Governing Equations

The governing equations for immiscible two phase flow in porous media are derived from mass conservation principles combined with the multiphase flow extension of Darcy's law. For incompressible fluids and an incompressible medium the governing equations for each phase are given by:

$$\frac{\partial \phi S_\alpha \rho_\alpha}{\partial t} + \nabla \cdot \mathbf{q}_\alpha \rho_\alpha = q^s_\alpha \rho_\alpha \tag{2.9}$$

where S_α is the saturation for each phase (here α = C for CO_2, α = B for brine), q^s_α is a source/sink term, and $\mathbf{q}_\alpha$ is the volumetric flux of each phase and is given by the multiphase flow extension of Darcy's law:

$$\mathbf{q}_\alpha = -\frac{\mathbf{k} k^\alpha_{rel}}{\mu^\alpha} \cdot (\nabla p^\alpha - \rho^\alpha \mathbf{g}) \tag{2.10}$$

where $\mathbf{k}$ is the intrinsic permeability of the porous medium, k_{rel}^{α} is the relative permeability of each phase, μ^{α} is the viscosity of each phase, p^{α} is the pressure in each phase, ρ^{α} is the density of each phase, $\mathbf{g}$ is the gravitational vector. The relative permeability, k_{rel}^{α} reflects the fact that permeability of the medium to each phase is different.

Solving the full three-dimensional multiphase flow equations may be extremely computationally expensive. One can, however, take advantage of the fact that the vertical dimension of the aquifer is much smaller than the horizontal dimensions and use vertical averaging to reduce the dimensionality of the equations.

2.4 Vertically Averaged Multiphase Flow

The injection of CO_2 into a brine-filled aquifer is illustrated in Figure 2.1. The technique of vertical averaging has been used to reduce the complexity of CO_2 injection simulations and significantly improve the computational efficiency of carbon sequestration modelling [17, 18, 19, 20]. The approach reduces the dimensionality of the problem (e.g., from three dimensions to two dimensions) by integrating the continuity equations (2.9) vertically through each aquifer.

The vertically averaged formulation is based on several assumptions: incompressibility of brine; CO_2 and solid matrix; constant viscosity and density for brine and CO_2; constant intrinsic permeability; a sharp interface between the brine and CO_2; hydrostatic vertical pressure variation; and no capillary pressure at the interface [3]. The assumption that the boundary between the fluids is a sharp interface is common as it leads to a great simplification of the governing equations, for example in [38, 63, 64].

High permeability reservoirs are currently favored for sequestration [12]. Therefore, it is a reasonable first-order approximation to assume that the capillary forces are negligible

in comparison to the gravity forces. The large gravity forces result from the large density contrast and the height of the fluid columns. Therefore, to make the problem simpler, capillary forces will be neglected as was done in [3]. When more detailed case-specific modelling is required, such as design of a specific operation in a particular geological location, models that account for capillarity (e.g., TOUGH2) can be used to refine predictions.

CO_2 reacts with the brine to form carbonate minerals, which can lead to reduced porosity and permeability. However, these reactions occur over very long time scales (e.g., over a thousand years) [2, 3], and as such can safely be neglected in this thesis, where the focus is on plume migration during the injection period.

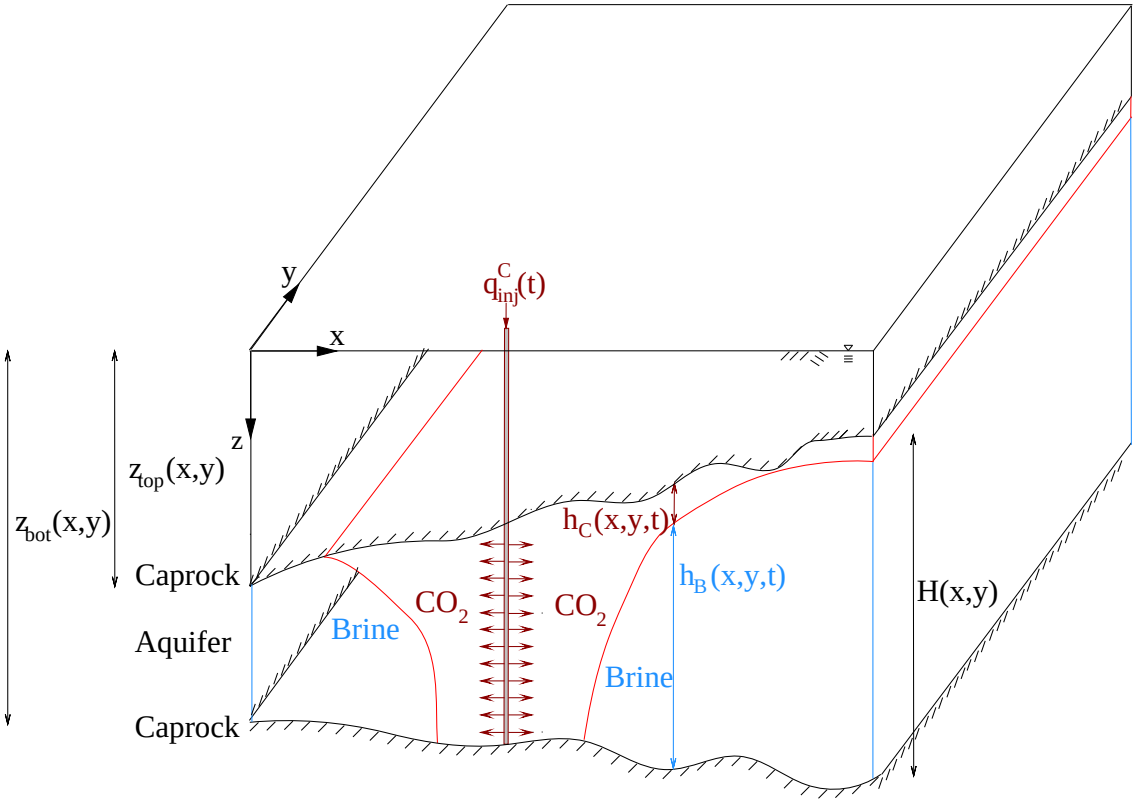

Figure 2.1: Parameters of carbon sequestration model.

The vertically averaged flow equations are obtained from mass balance equations for the CO_2 phase and the brine phase combined with the multiphase flow extensions of Darcy's Law for each phase [3]. The mass balance equations for the CO_2 and brine

phases are [3]:

$$\phi(1 - S_B^{res})\frac{\partial h_C}{\partial t} + \nabla \cdot \hat{\mathbf{q}}^C = q_{leak}^C \tag{2.11}$$

$$\phi(1 - S_B^{res})\frac{\partial h_B}{\partial t} + \nabla \cdot \hat{\mathbf{q}}^B = q_{leak}^B \tag{2.12}$$

where ϕ is the porosity of the aquifer, S_B^{res} is the brine residual saturation, h_C is the depth of the CO_2, h_B is the depth of the brine, $\hat{\mathbf{q}}^C$ is the vertically averaged CO_2 flux, $\hat{\mathbf{q}}^B$ is the vertically averaged brine flux, q_{leak}^C is a source term to account for the injection/leakage of CO_2, q_{leak}^B is a source term to account for the leakage of brine. In the equations above, the densities are eliminated from the mass balance equations by dividing both sides of the equation by the appropriate density. Figure 2.1 illustrates several key parameters from (2.11) and (2.12)

Vertical averaging begins with integrating the mass balance equations for each phase (2.11) and (2.12) over the thickness of the aquifer and substituting in the vertically averaged fluxes (2.13) and (2.14). Reference [41] provides a detailed description of the derivation.

The vertically average fluxes are given by the multiphase extension of Darcy's Law [3]:

$$\hat{\mathbf{q}}^C = -h_C\frac{\mathbf{k}k_{rel}^C}{\mu_C}(\nabla p_{bot} - \rho_B g\nabla H + \Delta\rho g\nabla h_C + \rho_C g\nabla z_{top}) \tag{2.13}$$

$$\hat{\mathbf{q}}^B = -h_B\frac{\mathbf{k}}{\mu_B}(\nabla p_{bot} + \rho_B g\nabla z_{bot}) \tag{2.14}$$

where $\mathbf{k}$ is the intrinsic permeability, k_{rel}^C is the relative permeability, μ_C is the viscosity of CO_2, μ_B is the viscosity of brine, p_{bot} is the pressure at the bottom of the formation, ρ_C is the density of CO_2, ρ_B is the density of the brine, $\Delta\rho = \rho_B - \rho_C$, g is the gravitational constant, z_{top} is the vertical height of the top of the aquifer, z_{bot} is the vertical height of

the bottom of the aquifer, and H is the thickness of the aquifer.

Pressure and Saturation Equations

In order to solve this system of non-linear coupled partial differential equations (PDEs) equations (2.11) and (2.12) are manipulated to arrive at one equation that can be solved for the pressure at the bottom of the aquifer and another equation that can be solved for the height of the interface between the two phases [41]. These two equations are called the pressure equation and the saturation equation.

The pressure equation is obtained using the mass balance equations (2.11) and (2.12). The mass balance equation for each phase is multiplied by the density of the other phase. These two equations are then added together. Using this approach leads to the transient terms cancelling out. The result is an steady-state elliptical pressure equation.

$$\nabla \cdot \left(h_C \frac{\mathbf{k} k_{REL}^C}{\mu_C} (\nabla p_{bot} + \Delta \rho g \nabla h_C) + h_B \frac{\mathbf{k}}{\mu_B} (\nabla p_{bot}) \right) = -q_{leak}^B - q_{leak}^C \tag{2.15}$$

$$p_{bot}(\mathbf{x}, t) = \overline{p}_{bot}(\mathbf{x}, t) \text{ on } \Gamma_p \tag{2.16}$$

$$\hat{\mathbf{q}}^C(\mathbf{x}, t) \cdot \mathbf{n} = \overline{\mathbf{q}}^C(\mathbf{x}, t) \text{ on } \Gamma_q \tag{2.17}$$

$$\hat{\mathbf{q}}^B(\mathbf{x}, t) \cdot \mathbf{n} = \overline{\mathbf{q}}^B(\mathbf{x}, t) \text{ on } \Gamma_q \tag{2.18}$$

The assumption of incompressibility is reflected in the loss of the transient term in 2.15. The compressibility of the CO_2 may be particularly important near injection wells. Further away from the wells, however, the pressure gradient is much smaller and thus the incompressibility assumption is quite reasonable. The focus of the models developed in this thesis is on the late time CO_2 plume evolution. As such, the assumption of incompressibility is a good approximation for the model described in this thesis.

The saturation equation is obtained by substituting the multiphase extension of Darcy's Law (2.14) into the mass balance for brine (2.12). The brine equation is selected as the saturation equation in this thesis, but the CO_2 mass balance equation could also have be used as the saturation equation.

$$\phi(1 - S_B^{res})\frac{\partial h_B}{\partial t} - \nabla \cdot \left(h_B \frac{\mathbf{k}}{\mu_B}(\nabla p_{bot} + \rho_B g \nabla z_{bot}) \right) = q_{leak}^B \tag{2.19}$$

$$h_B(\mathbf{x}, t) = \overline{h}_B(\mathbf{x}, t) \text{ on } \Gamma_h \tag{2.20}$$

$$h_B(\mathbf{x}, 0) = h_o(\mathbf{x}) \text{ on } \Omega \tag{2.21}$$

In Chapter 4, Chapter 5, and Chapter 6 a description is given of how these two equations are discretized in space using the FEM and integrated in time using the FDM.

2.5 Coupled Models

Most of the studies in the literature that deal with CO_2 sequestration consider uncoupled models that, in general, solve for only one physical process (e.g., flow) and ignore other physics involved (e.g., thermal, mechanical, chemical effects). It is often crucial, however, to understand the many physical process that occur during CO_2 injection and how they affect one another. For example, the thermal stresses induced during injection can create leakage pathways in the form of fractures through the caprock. A review of coupling approaches applicable to carbon sequestration is given in [65].

Numerical models for carbon sequestration can include the coupling of many processes such as: stress-temperature, stress-temperature-chemical, pressure-stress, pressure-stress-temperature. In the numerical framework developed in this thesis, the coupling exists between pressure and the average CO_2 (or brine) depth.

There are three main ways to handle the coupled physical processes discussed in numerical models: one-way coupling, sequential (iterative) coupling, and full coupling [66]. One-way coupling involves first obtaining solutions to the one of the unknowns. The second equation is updated with the solution to the first unknown and it is used to solve for the second unknown. This method is called a one-way coupling because there is only a one-way transfer of information. For example with pressure-stress coupling, solutions are first obtained for the fluid equations [66]. The pore pressures are then updated and used to solve the geomechanical equations of stress. The fluid solutions transfer the updated pore pressures to the geomechanical solution, but the geomechanical solution does not transfer any information to the fluid solutions.

In sequential coupling, the solution of the first unknown is used to solve for the second unknown. The second unknown is used to update the solution of the first unknown. The updated solution for the first unknown is used to update the second unknown. This process of updating the solutions to the unknowns can be repeated one or more times. As an example of sequential coupling consider a pressure-displacement coupling. The pressure equations are solved while the displacements remain constant, then the momentum equations are solved while the pressures remain constant [66]. Information is passed back and forth between solvers until convergence is achieved. Sequential coupling can be done using two separate software programs - a fluid flow solver and a geomechanics solver. Sequentially coupled solutions for fluid flow and geomechanics are studied in [67]. One useful sequential coupling strategy that has been useful to the reservoir simulation community is IMPES (IMplicit Pressure Explicit Saturation) [68]. A special case of sequential coupling is explicit (staggered) coupling, where only a single iteration is performed.

In full coupling, all of the equations are solved simultaneously. A fully coupled multi-

phase flow and thermo-poromechanical effects formulation is considered in [66] where the fully coupled solution was compared with one-way coupling and iterative coupling and superior accuracy of fully coupled solutions was demonstrated.

The importance of coupled models of various forms for carbon sequestration problems has been demonstrated in several studies. Using the In Salah project as a case study, a coupled reservoir-geomechanics analysis of CO_2 injection was performed [69]. Simulations were compared with ground deformation monitoring, to explain the ground deformations. In [47] coupled simulations of CO_2 injection were performed. The simulations included effects of Thermal-Hydraulic-Mechanical-Chemical (THMC). A stabilized FEM was used to assess stress and pressure changes near an injection. The results show that chemical and thermal processes can have significant effects near an injection well. Coupled simulations have also been demonstrated to be useful to estimate safe injection pressures near faults in [16, 47].

Coupled models are an important tool to help understand how various physical processes influence one another. By using coupled models carbon sequestration systems can be better understood. Coupled models can be used to test critical assumptions made in uncoupled models. A widespread acknowledgment of this importance is responsible for the recent publication of many good papers on the subject (e.g., [47, 66, 70, 65]).

2.6 Chapter Summary

In this chapter the fundamentals of flow in porous media were reviewed. Essential concepts were presented to understand single phase flow and then the governing equations for single phase flow were discussed. The related concepts and governing equations for multiphase flow were then described. Vertically averaged multiphase flow governing equa-

tions were presented as a basis for mathematical modelling of plume evolution in carbon sequestration. The chapter concluded with a discussion of solution strategies for coupled problems.

Chapter 3

Stabilized Finite Element Methods for Advection-Diffusion-Reaction Equations

3.1 Introduction

There are many possible forms of the Finite Element Method (FEM), but typically FEM refers to the Galerkin FEM where the weight functions and interpolation functions are of the same form. The standard Galerkin FEM is well suited for diffusion problems (i.e. Poisson's equation) since the diffusion operator is symmetric. This leads to symmetric system matrices and the best approximation property of FEM applies [71]. The best approximation property states that the error in the FEM approximation will be minimized by finding the optimal function from the approximation space. Therefore, the FEM approximation will find the optimal solution based on the assumed shape functions. The Galerkin FEM, however, can encounter non-physical oscillations and instabilities when discretizing PDEs with significant advection terms. An advection operator is of the first order and leads to unsymmetric system matrices. The Galerkin FEM discretization of a

PDE with an advection term leads to a truncation error in the form of negative artificial diffusion. Therefore spatial instabilities can occur in the solution when advection is present in the governing equation [72, 71] and dominates the diffuse term.

In the development of a carbon sequestration simulation framework, one of the two non-linear coupled PDEs is dominated by an advection term. This section discusses various alternative FEMs available to solve this problem. In order to do this, one dimensional model problems are used to elucidate some techniques that will prove useful in later chapters.

3.2 Types of Partial Differential Equations

In general there are three types of partial differential equations (PDEs): elliptical, parabolic, and hyperbolic. Mathematically these three classes of PDEs can be described by the following general form:

$$c_1(x,y)\frac{\partial^2 u}{\partial x^2}+c_2(x,y)\frac{\partial^2 u}{\partial x \partial y}+c_3(x,y)\frac{\partial^2 u}{\partial y^2}+c_4(x,y)\frac{\partial u}{\partial x}+c_5(x,y)\frac{\partial u}{\partial y}+c_6(x,y)u+c_7(x,y)=0 \tag{3.1}$$

where $c_1(x,y), c_2(x,y), c_3(x,y), c_4(x,y), c_5(x,y), c_6(x,y)$, and $c_7(x,y)$ are variables that in general vary in space.

If $c_2^2 - 4c_1c_3 < 0$ then (3.1) is an elliptical equation.

If $c_2^2 - 4c_1c_3 = 0$ then (3.1) is a parabolic equation.

If $c_2^2 - 4c_1c_3 > 0$ then (3.1) is a hyperbolic equation.

If $c_1 = c_2 = c_3 = 0$ then (3.1) is a first order PDE which is hyperbolic.

The Galerkin FEM provides excellent approximations for elliptical and parabolic equations since the system of equations are symmetric, and thus the best approximation prop-

erty holds. For advection equations, which are first order hyperbolic PDEs, the Galkerin FEM leads to unsymmetric systems which lose the best approximation property [71].

3.3 Advection-Diffusion-Reaction Equation

The governing equation that is the subject of this chapter is the advection-diffusion-reaction equation, which is given as:

$$\frac{\partial u}{\partial t} + a\frac{\partial u}{\partial x} - v\frac{\partial^2 u}{\partial x^2} + \sigma u = s \tag{3.2}$$

$$u(x,0) = u_o(x) \text{ on } \Omega \tag{3.3}$$

$$u = u_D \text{ on } \Gamma_D \tag{3.4}$$

$$vn\frac{\partial u}{\partial x} = h \text{ on } \Gamma_N \tag{3.5}$$

where u is an unknown scalar quantity, a is the velocity, v is the diffusion coefficient, σ is a reaction term, s is a source/sink term, Ω is the entire domain, Γ_D is the Dirichlet (essential) boundary, Γ_N is the Neumann (natural) boundary, u_o is the initial value of u, u_D is the prescribed value of u on the boundary Γ_D, n is a unit normal to the boundary Γ_N, and h is the prescribed flux on the boundary Γ_N.

The first term in (3.2) is the unsteady term, the second is the advection of the unknown quantity u, by the velocity a. The third is the diffusion of the unknown quantity u. The fourth term is the reaction, σ. If $\sigma > 0$ then it represents the dissipation of the quantity u and if $\sigma < 0$ then it represents the production of the quantity u.

The Galerkin FEM does not satisfy the original PDE, but instead implicitly solves a modified equation which has an additional term added to the original which represents negative artificial diffusion [71]. Quadratic elements have the added difficulty that the

mid and corner nodes have different forms of the negative diffusion operator [71]. The negative diffusion operator introduced by the Galerkin approximation is given by:

$$\overline{v}\frac{\partial^2 u}{\partial x^2} \tag{3.6}$$

where $\overline{v}$ is the artificial diffusion coefficient. The Galerkin FEM effectively solves (3.2) with (3.6) added to the left hand side of the equation.

3.3.1 Peclet Number

The Peclet number is a measure of the relative magnitude of advection to diffusion. The mesh Peclet number is given by:

$$Pe = \frac{a\Delta x}{2v} \tag{3.7}$$

where Δx is a measure of the element size.

When $|Pe| > 1$ spatial oscillations can occur with the Galerkin FEM. If diffusion is not present, Pe approaches infinity, and the Galerkin method gives a solution that is very likely to be contaminated by non-physical oscillations, which can be difficult to control.

3.3.2 Damkohler Number

The Damkohler number, D is a measure of the relative magnitude of the reaction term and the advection term. The mesh Damkohler number is calculated from:

$$D = \frac{\sigma\Delta x}{a} \tag{3.8}$$

The Damkohler number is used to compare the magnitudes of the reaction term and

the advection term.

3.4 Weak Form

Before (3.2) is discretized with the Galerkin Finite Element method the weak form is considered first. The weak form of (3.2) that results from the Galerkin approach is find $u(x,t) \in U$ such that:

$$\int_\Omega \delta u \frac{\partial u}{\partial t} d\Omega + \int_\Omega \delta u a \frac{\partial u}{\partial x} d\Omega + \int_\Omega \frac{\partial \delta u}{\partial x} v \frac{\partial u}{\partial x} d\Omega + \int_\Omega \delta u \sigma d\Omega = \int_\Omega \delta u s d\Omega + \int_{\Gamma_N} \delta u h d\Gamma, \forall \delta u \in U_0 \tag{3.9}$$

where δu is a weight function. The function spaces for u and δu are given as:

$$\begin{aligned} U &= \{u(x,t) | u(x,t) \in H^1, u(x,t) = \overline{u} \text{ on } \Gamma_u\} \\ U_0 &= \{\delta u(x) | \delta u(x) \in H^1, \delta u(x) = 0 \text{ on } \Gamma_q\} \end{aligned} \tag{3.10}$$

where $\overline{u}$ is the prescribed value of the Dirichlet boundary condition, Γ_u is the Dirichlet boundary, and Γ_q is the Neumann boundary.

3.5 Stabilization Techniques

For advection-diffusion-reaction equations, when the Peclet number is large, oscillations can occur in a Galerkin FEM solution. Oscillations can arise from the solution of (3.2) because the Galerkin FEM actually solves a modified form of (3.2) where the diffusion coefficient v is equal to $\overline{v}$ (see (3.6)). Sharp gradients in the solution, as occur at the start of CO_2 injection, when CO_2 plumes merge or when the CO_2 plume reaches the boundaries of the domain, are particularly problematic. There are several approaches to stabilize

these approximations including: the Streamline Upwind (SU) method [73], the Streamline Upwind Petrov Galerkin (SUPG) method [73], the Least Squares Finite Element Method (LSFEM) [74, 75, 76], the Subgrid Scales (SGS) method [77, 78], the Galerkin Least Squares (GLS) method [79], Upwinding [80, 81], the Taylor-Galerkin method [82], Bubble Functions [83], Finite Increment Calculus [84], and the Discontinuous Galerkin (DG) method [85].

In this chapter the discussion and examples will focus on five stabilized FEMs: the Streamline Upwind (SU) method [73], the Streamline Upwind Petrov Galerkin (SUPG) method [73], the Least Squares Finite Element Method (LSFEM) [74, 75, 76], the Subgrid Scales (SGS) method [77, 78] and the Galerkin Least Squares (GLS) method [79]. These five methods stabilize the Galerkin FEM by the use of a perturbation operator that operates on the weight function [71]. The modified weak form for the stabilized methods is given as: find $u(x,t) \in U$ such that:

$$\begin{aligned} \int_\Omega \delta u \frac{\partial u}{\partial t} d\Omega + \int_\Omega \delta u a \frac{\partial u}{\partial x} d\Omega + \int_\Omega \frac{\partial \delta u}{\partial x} v \frac{\partial u}{\partial x} d\Omega + \int_\Omega \delta u \sigma d\Omega \\ + \sum_e \int_{\Omega_e} P(\delta u) \tau R(u) d\Omega = \int_\Omega \delta u s d\Omega + \int_{\Gamma_N} \delta u h d\Gamma \end{aligned} \tag{3.11}$$

where $R(u)$ is the residual of (3.2), $P(\delta u)$ is a perturbation operator that distinguishes the stabilization methods, τ is a stabilization parameter, and e is the element number. Note that when $R(u) = 0$ the weak form (3.11) is equivalent to (3.9).

3.5.1 Streamline Upwind (SU) and Streamline Upwind Petrov Galerkin (SUPG)

The Streamline Upwind (SU) and Streamline Upwind Petrov Galerkin (SUPG) stabilizations [86] have a perturbation operator in the form of [71]:

$$P(\delta u) = a\frac{\partial \delta u}{\partial x} \tag{3.12}$$

where a is the velocity and δu is a weight function from the Galerkin method.

The difference between SU and SUPG is in a different form of the residual $R(u)$. SUPG uses the full residual from (3.2):

$$R(u) = \frac{\partial u}{\partial t} + a\frac{\partial u}{\partial x} - v\frac{\partial^2 u}{\partial x^2} + \sigma u - s \tag{3.13}$$

while SU only uses the advection term of the residual:

$$R(u) = a\frac{\partial u}{\partial x} \tag{3.14}$$

3.5.2 Stabilization Parameter

The stabilization parameter, τ in (3.11) scales the additional term that is added to the Galerkin formulation to stabilize the spatial oscillations. Many definitions of the stabilization parameter τ are presented in the literature. Two forms of the stabilization parameter for one dimension for use with the θ-family of time integration schemes are given by [87] and [88] respectively:

$$\tau = \left(\left(\frac{1}{\theta \Delta t}\right)^2 + \left(\frac{2a}{\Delta x}\right)^2 + 9\left(\frac{4v}{\Delta x^2}\right)^2 + \sigma^2 \right)^{-1/2} \tag{3.15}$$

$$\tau = \left(\frac{1}{\theta \Delta t} + \frac{2a}{\Delta x} + \frac{4v}{\Delta x^2} + \sigma \right)^{-1} \tag{3.16}$$

where Δt is the timestep size, Δx is the element size, and θ determines the time integration scheme. $\theta = 0$ is the Forward Euler (FE) method, $\theta = 0.5$ is the Crank-Nicolson (CN) method, and $\theta = 1$ is the Backward Euler (BE) method. At large Peclet numbers these two definitions of τ give the same result.

3.5.3 Galerkin Least Squares (GLS)

The Galerkin Least Squares (GLS) stabilization was first presented in [79]. The perturbation operator is derived from a least squares minimization of the residual [79]. The perturbation operator for the GLS stabilization is [71]:

$$P(\delta u) = a \frac{\partial \delta u}{\partial x} - v \frac{\partial^2 \delta u}{\partial x^2} + \sigma \delta u \tag{3.17}$$

$P(\delta u)$ for GLS is the same as SUPG for the advection diffusion equation when linear elements are used to approximate u and $\sigma = 0$. The residual is given by (3.13).

3.5.4 Subgrid Scales Method (SGS)

The Subgrid Scales (SGS) method was originally appeared in [77] and was adapted to the advection-diffusion equation in [89]. In the SGS method the perturbation operator takes the form [71]:

$$P(\delta u) = a \frac{\partial \delta u}{\partial x} + v \frac{\partial^2 \delta u}{\partial x^2} - \sigma \delta u \tag{3.18}$$

Just as with GLS stabilization this reduces to SUPG for linear elements when $\sigma = 0$. The residual is given by (3.13).

3.5.5 Least Squares Finite Element Method (LSFEM)

The Least Squares Finite Element Method (LSFEM) can be represented by the same weak form as the Galerkin FEM, but the weight functions are replaced by the LSFEM weight function. Two LSFEM formulations can be obtained for transient problems. The difference lies in the order of the discretization. The weak form for LSFEM can be written as find $u(x,t) \in U$ such that:

$$\int_\Omega \delta u^{LS} \frac{\partial u}{\partial t} d\Omega + \int_\Omega \delta u^{LS} a \frac{\partial u}{\partial x} d\Omega + \int_\Omega \frac{\partial \delta u^{LS}}{\partial x} v \frac{\partial u}{\partial x} d\Omega + \int_\Omega \delta u^{LS} \sigma d\Omega = \int_\Omega \delta u^{LS} s d\Omega + \int_{\Gamma_N} \delta u^{LS} h d\Gamma \tag{3.19}$$

where $\delta u^{LS,ST} = a\frac{\partial \delta u}{\partial x} - v\frac{\partial^2 \delta u}{\partial x^2} + \sigma \delta u$ if space is discretized first and $\delta u^{LS,TS} = \delta u + a\frac{\partial \delta \delta u}{\partial x} - v\frac{\partial^2 u}{\partial x^2} + \sigma \delta u$ if time is discretized first.

LSFEM and GLS are similar, but differ in two main ways. In LSFEM the entire weight function is applied throughout the domain, while GLS applies the Galerkin portion of the weight function throughout the entire domain, but the remainder of the weight function (the perturbation function) is applied only over the element interiors when $\tau \neq 0$.

The second difference between LSFEM and GLS is the stabilization parameter τ. In LSFEM $\tau = \theta \Delta t$ arises naturally from the derivation. GLS, on the other hand, requires the selection of a somewhat arbitrary value of τ such as that given in [88].

3.6 Finite Difference Method (FDM) Discretization in Time

When (3.9) or (3.11) is discretized in space, a system of equations of the following form must be solved:

$$[\mathbf{C}]\{\dot{\mathbf{u}}\} + [\mathbf{K}]\{\mathbf{u}\} = \{\mathbf{F}\} \tag{3.20}$$

where $[\mathbf{C}]$ is a storage matrix, $[\mathbf{K}]$ is a conductance matrix, and $\{\mathbf{F}\}$ is a flux vector. These matrices are defined in the next section for the various spatial discretization schemes. In this chapter, the time domain is discretized using the θ-family of FDMs, leading to the system of equations of the form:

$$\begin{aligned} &([\mathbf{C}] + \Delta t\theta[\mathbf{K}])\{\mathbf{u}\}^{n+1} = \\ &([\mathbf{C}] - \Delta t\,(1-\theta)\,[\mathbf{K}])\{\mathbf{u}\}^{n} + \Delta t\left(\theta\{\mathbf{F}\}^{n+1} + (1-\theta)\{\mathbf{F}\}^{n}\right) \end{aligned} \tag{3.21}$$

which can be rewritten as:

$$[\mathbf{K_{eff}}]\{\mathbf{u}\}^{n+1} = \{\mathbf{F_{eff}}\}^{n+1} \tag{3.22}$$

where

$$[\mathbf{K_{eff}}] = ([\mathbf{C}] + \Delta t\theta[\mathbf{K}]) \tag{3.23}$$

and

$$\{\mathbf{F_{eff}}\}^{n+1} = ([\mathbf{C}] - \Delta t\,(1-\theta)\,[\mathbf{K}])\{\mathbf{u}\}^{n} + \Delta t\left(\theta\{\mathbf{F}\}^{n+1} + (1-\theta)\{\mathbf{F}\}^{n}\right) \tag{3.24}$$

where $[\mathbf{K_{eff}}]$ is the effective conductance matrix, and $\{\mathbf{F_{eff}}\}$ is the effective flux vector. If $\theta = 0$ this is referred to as Forward Euler (FE), if $\theta = 0.5$ it is called Crank-Nicolson

(CN) and if $\theta = 1$ it is referred to as Backward Euler (BE).

3.7 Stabilized FEM Discretizations in Space

3.7.1 Galerkin FEM Discretization

The discrete equations are obtained by substituting the finite element shape functions into the weak form (e.g., (3.11)). The finite element approximation is given by:

$$u^h(x) = \sum_{I \in \mathcal{N}} N_I(x) u_I, x \in \Omega \tag{3.25}$$

where $N_I(x)$ are the shape functions, u_I is the unknown quantity at the node I, and $\mathcal{N}$ is the set of all nodes in the domain Ω. The Galerkin advection-reaction matrix is given by:

$$\mathbf{K}_G^e = \int_{\Omega^e} \mathbf{N^e}^\mathsf{T} a \mathbf{B^e} d\Omega^e + \int_{\Omega^e} \mathbf{N^e}^\mathsf{T} \sigma \mathbf{N^e} d\Omega^e \tag{3.26}$$

where $\mathbf{N^e}$ is the shape function vector for element e, $\mathbf{B^e}$ are the derivatives of the shape functions, and Ω^e is the domain of element e. The Galerkin storage matrix is given by:

$$\mathbf{C}_G^e = \int_{\Omega^e} \mathbf{N^e}^\mathsf{T} \mathbf{N^e} d\Omega^e \tag{3.27}$$

The Galerkin source flux vector is given by:

$$\mathbf{F}_G^e = \int_{\Omega^e} \mathbf{N^e}^\mathsf{T} s d\Omega^e \tag{3.28}$$

3.7.2 SU and SUPG FEM Discretizations

The SUPG and SU advection-reaction matrices are given by:

$$\mathbf{K}^e_{SUPG} = \int_{\Omega^e} \mathbf{N^e}^\mathsf{T} a \mathbf{B^e} d\Omega^e + \int_{\Omega^e} \mathbf{N^e}^\mathsf{T} \sigma \mathbf{N^e} d\Omega^e + \int_{\Omega^e} \mathbf{B^e}^\mathsf{T} \tau a^2 \mathbf{B^e} d\Omega^e + \int_{\Omega^e} \mathbf{B^e}^\mathsf{T} \tau a \sigma \mathbf{N^e} d\Omega^e \tag{3.29}$$

and

$$\mathbf{K}^e_{SU} = \int_{\Omega^e} \mathbf{N^e}^\mathsf{T} a \mathbf{B^e} d\Omega^e + \int_{\Omega^e} \mathbf{N^e}^\mathsf{T} \sigma \mathbf{N^e} d\Omega^e + \int_{\Omega^e} \mathbf{B^e}^\mathsf{T} \tau a^2 \mathbf{B^e} d\Omega^e \tag{3.30}$$

The SUPG and SU storage matrices are given by:

$$\mathbf{C}^e_{SUPG} = \int_{\Omega^e} \mathbf{N^e}^\mathsf{T} \mathbf{N^e} d\Omega^e + \int_{\Omega^e} (\mathbf{N^e} + a\mathbf{B^e})^\mathsf{T} \mathbf{N^e} d\Omega^e \tag{3.31}$$

and

$$\mathbf{C}^e_{SU} = \mathbf{C}^e_G \tag{3.32}$$

The SUPG and SU source flux vectors are given by:

$$\mathbf{F}^e_{SUPG} = \int_{\Omega^e} \mathbf{N^e}^\mathsf{T} s d\Omega^e + \int_{\Omega^e} \mathbf{B^e}^\mathsf{T} a s d\Omega^e \tag{3.33}$$

and

$$\mathbf{F}^e_{SU} = \mathbf{F}^e_G \tag{3.34}$$

3.7.3 GLS FEM Discretization

The GLS advection-reaction matrix is given by:

$$\mathbf{K}^e_{GLS} = \int_{\Omega^e} \mathbf{N^e}^\mathsf{T} a \mathbf{B^e} d\Omega^e + \int_{\Omega^e} \mathbf{N^e}^\mathsf{T} \sigma \mathbf{N^e} d\Omega^e + \int_{\Omega^e} (a\mathbf{B^e} + \sigma \mathbf{N^e})^\mathsf{T} \tau (a\mathbf{B^e} + \sigma \mathbf{N^e}) d\Omega^e \tag{3.35}$$

The GLS storage matrix is given by:

$$\mathbf{C}^e_{GLS} = \int_{\Omega^e} \mathbf{N^e}^\mathsf{T} \mathbf{N^e} d\Omega^e + \int_{\Omega^e} (a\mathbf{B^e} + \sigma \mathbf{N^e})^\mathsf{T} \tau \mathbf{N^e} d\Omega^e \tag{3.36}$$

The GLS source flux vector is given by:

$$\mathbf{F}^e_{GLS} = \int_{\Omega^e} \mathbf{N^e}^\mathsf{T} s d\Omega^e + \int_{\Omega^e} (a\mathbf{B^e} + \sigma \mathbf{N^e})^\mathsf{T} \tau s d\Omega^e \tag{3.37}$$

3.7.4 SGS FEM Discretization

The SGS advection-reaction matrix is given by:

$$\mathbf{K}^e_{SGS} = \int_{\Omega^e} \mathbf{N^e}^\mathsf{T} a \mathbf{B^e} d\Omega^e + \int_{\Omega^e} \mathbf{N^e}^\mathsf{T} \sigma \mathbf{N^e} d\Omega^e + \int_{\Omega^e} (a\mathbf{B^e} - \sigma \mathbf{N^e})^\mathsf{T} \tau (a\mathbf{B^e} + \sigma \mathbf{N^e}) d\Omega^e \tag{3.38}$$

The SGS storage matrix is given by:

$$\mathbf{C}^e_{SGS} = \int_{\Omega^e} \mathbf{N^e}^\mathsf{T} \mathbf{N^e} d\Omega^e + \int_{\Omega^e} (a\mathbf{B^e} - \sigma \mathbf{N^e})^\mathsf{T} \tau \mathbf{N^e} d\Omega^e \tag{3.39}$$

The SGS source flux vector is given by:

$$\mathbf{F}^e_{SGS} = \int_{\Omega^e} \mathbf{N^e}^\mathsf{T} s d\Omega^e + \int_{\Omega^e} (a\mathbf{B^e} - \sigma\mathbf{N^e})^\mathsf{T} \tau s d\Omega^e \tag{3.40}$$

3.7.5 LSFEM Discretization

If space is discretized first (or for a steady state problem) then the LSFEM advection-reaction matrix is given by:

$$\mathbf{K}^e_{LSFEM,ST} = \int_{\Omega^e} (a\mathbf{B^e} + \sigma\mathbf{N^e})^\mathsf{T} (a\mathbf{B^e} + \sigma\mathbf{N^e}) d\Omega^e \tag{3.41}$$

The LSFEM storage matrix is given by:

$$\mathbf{C}^e_{LSFEM,ST} = \int_{\Omega^e} (a\mathbf{B^e} + \sigma\mathbf{N^e})^\mathsf{T} \mathbf{N^e} d\Omega^e \tag{3.42}$$

The LSFEM source flux vector is given by:

$$\mathbf{F}^e_{LSFEM,ST} = \int_{\Omega^e} (a\mathbf{B^e} + \sigma\mathbf{N^e})^\mathsf{T} s d\Omega^e \tag{3.43}$$

On the other hand, if the discretization in time is performed first, then the LSFEM matrices and vectors are given below. The LSFEM advection-reaction matrix is:

$$\mathbf{K}^e_{LSFEM,TS} = \int_{\Omega^e} \mathbf{N^e}^\mathsf{T} a\mathbf{B^e} d\Omega^e + \int_{\Omega^e} \mathbf{N^e}^\mathsf{T} \sigma\mathbf{N^e} d\Omega^e + \int_{\Omega^e} (a\mathbf{B^e} + \sigma\mathbf{N^e})^\mathsf{T} (a\mathbf{B^e} + \sigma\mathbf{N^e}) d\Omega^e \tag{3.44}$$

The LSFEM storage matrix is:

$$\mathbf{C}^e_{LSFEM,TS} = \int_{\Omega^e} \mathbf{N^e}^\mathsf{T}\mathbf{N^e} d\Omega^e + \int_{\Omega^e} (a\mathbf{B^e} + \sigma\mathbf{N^e})^\mathsf{T}\mathbf{N^e} d\Omega^e \tag{3.45}$$

The LSFEM source flux vector is:

$$\mathbf{F}^e_{LSFEM,TS} = \int_{\Omega^e} \mathbf{N^e}^\mathsf{T} s d\Omega^e + \int_{\Omega^e} (a\mathbf{B^e} + \sigma\mathbf{N^e})^\mathsf{T} s d\Omega^e \tag{3.46}$$

The above matrices are substituted into (4.32) to complete the space-time discretization. These discretizations will be demonstrated in the next section.

3.8 Courant Number

The Courant number is a measure of the timestep size in relation to the advective velocity and the element size and is given by:

$$Cr = \frac{a\Delta t}{\Delta x} \tag{3.47}$$

where Δt is the timestep size and Δx is the element size.

3.9 A Comparison of Stabilization Methods for One Dimensional Advection / Advection-Reaction Equations

In this section four numerical examples are provided to compare the Galerkin FEM and five stabilized FEMs (SU, SUPG, GLS, SGS, LSFEM). The examples focus on four variants of (3.2): the steady state advection equation, the steady state advection-reaction

equation, the unsteady advection equation, and the unsteady advection-reaction equation. All of the examples presented in this section are in one dimension, but the methodologies are applicable to two dimensional and three dimensional systems. Diffusion is not considered as it is not present in the advection-reaction equation that is considered in the chapters that follow. The absence of a diffusion term makes stabilization more difficult, since the presence of diffusion can offset the negative diffusion introduced by the Galerkin FEM discretization of an advection-diffusion-reaction equation.

3.9.1 One Dimensional Steady State Advection Equation

The steady state advection equation is now considered in one dimension. The governing equation and boundary conditions are given by:

$$a\frac{\partial u}{\partial x} = s(x) \tag{3.48}$$

$$u = u_D \text{ on } \Gamma_D \tag{3.49}$$

$$n\frac{\partial u}{\partial x} = f \text{ on } \Gamma_N \tag{3.50}$$

Example 1

For this example $a = 1$ is assumed to be constant. At $x = 0$ a Dirichlet boundary condition is imposed of $u = 0$. At $x = L$ a no flow Neumann boundary condition is specified. In other words, $f = 0$ in (3.50).

The source function is given by:

$$s(x) = \frac{e^{(x-1)/\epsilon}}{\epsilon(1 - e^{-1/\epsilon})}; \tag{3.51}$$

where $\epsilon = 0.05$ [54]. The exact solution of this problem is given as:

$$u_{exact} = 1 - \frac{(1 - e^{(x-1)/\epsilon)})}{(1 - e^{-1/\epsilon)})}; \tag{3.52}$$

Figure 3.1 compares the exact solution with the solutions obtained with the Galerkin, SU, SUPG, LSFEM methods using 10 linear finite elements to discretize the domain. The exact solution is plotted at the nodal locations and shown by the solid black line. The Galerkin solution shows non-physical oscillations. The SU, SUPG, and LSFEM solutions do not contain these oscillations. For the pure advection equation, the SGS and GLS stabilizations are equivalent to SUPG. In the case of SU, the perturbation function is not applied to the source term and as such erroneous results can occur when the source term is not zero as can be seen here.

Figure 3.2 shows the effect of increasing the number of elements to 100. All of the methods, including Galerkin appear to give smooth results. However, the Galerkin method gives non-physical oscillations of a very small magnitude as shown in Figure 3.3. The SU, SUPG, and LSFEM solutions do not contain these oscillations and the solutions agree well with the exact solution. The oscillations are still present in the Galerkin approximation when the number of elements is increased to 1024, as shown in Figure 3.5, although they are not apparent in Figure 3.4.

Figure 3.6 shows the convergence of the L_2 error. The L_2 error is given by:

$$\|\epsilon_{L_2}\| = \left(\int_\Omega (u^{exact} - u^h)^2 d\Omega \right)^{\frac{1}{2}} \tag{3.53}$$

where u^{exact} is the exact solution and u^h is the approximate solution. The normalized L_2

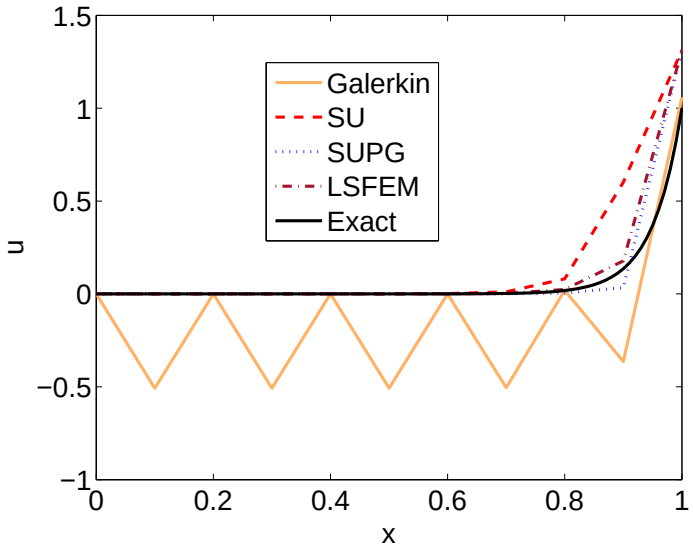

Figure 3.1: Solution to steady state advection problem using 10 elements.

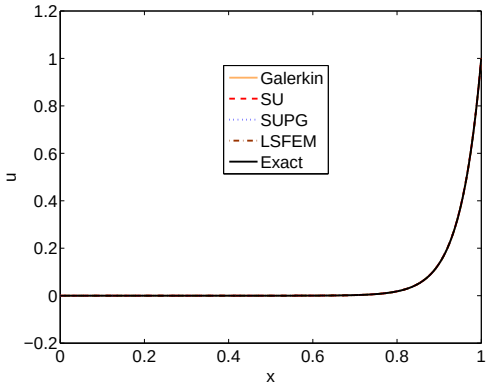

Figure 3.2: Solution to steady state advection problem using 100 elements.

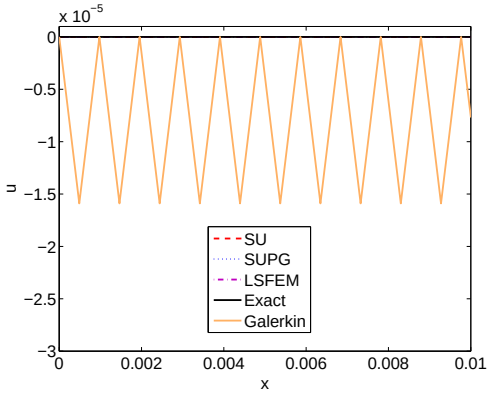

Figure 3.3: Solution to steady state advection problem using 100 elements. Close-up of small magnitude oscillations in Galerkin FEM solution.

error is given by:

$$\bar{\epsilon}_{L_2} = \frac{\left(\int_\Omega (u^{exact} - u^h)^2 d\Omega\right)^{\frac{1}{2}}}{\left(\int_\Omega (u^{exact})^2 d\Omega\right)^{\frac{1}{2}}} \tag{3.54}$$

From Figure 3.6 it can be seen that SUPG and LSFEM converge at the optimal rate of 2. SU converges at much lower rate of 1.02 because it is an inconsistent method as not every term in the residual is stabilized. The Galerkin FEM converges at a slightly slower rate and the L_2 error associated with Galerkin is larger for each element size than SUPG

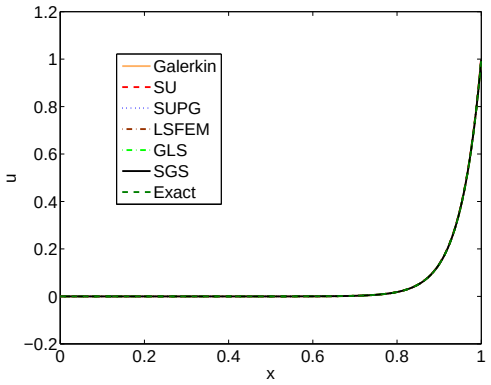

Figure 3.4: Solution to steady state advection problem using 1024 elements.

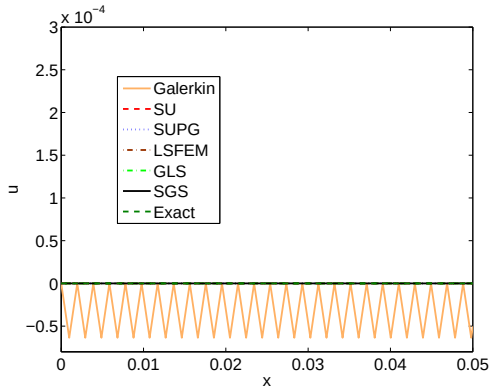

Figure 3.5: Solution to steady state advection problem using 1024 elements. Close-up of small magnitude oscillations in Galerkin FEM solution.

and LSFEM due to the presence of the oscillations that reduce with mesh refinement as shown in Figure 3.3 and Figure 3.5.

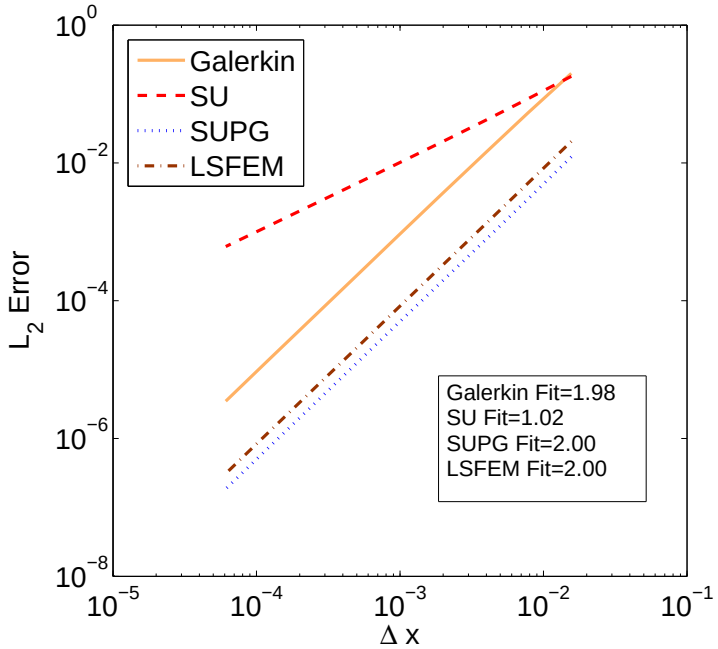

Figure 3.6: Convergence study of steady state advection problem.

3.9.2 One Dimensional Steady State Advection-Reaction Equation

In this subsection the steady-state advection-reaction equation is examined. It is similar to the steady state advection equation, but now a reaction term is also considered. The governing equation and boundary conditions are given by:

$$a\frac{\partial u}{\partial x} + \sigma u = s(x) \tag{3.55}$$

$$u = u_D \text{ on } \Gamma_D \tag{3.56}$$

$$n\frac{\partial u}{\partial x} = f \text{ on } \Gamma_N \tag{3.57}$$

The only difference between (3.55) and (3.50) is the addition of a reaction term to the left hand side of the equation. Since there is a reaction term in (3.55) SGS and GLS provide different stabilized methods than SUPG.

Example 1

The same example as the previous section is repeated here, but with $\sigma \neq 0$. Several values of σ are considered. The effect of σ on the exact solution is shown in Figure 3.7. The exact solution from the previous example ($\sigma = 0$) is shown by a solid blue line. Positive values (dashed lines) of $\frac{\sigma}{a}$ fall to the right of the $\sigma = 0$ solution. Negative values of $\frac{\sigma}{a}$ are indicated by solid lines and fall to the left of the $\sigma = 0$ solution.

Figure 3.8 shows the numerical solutions using 1024 element for the case when $\sigma = -100$. SUPG, GLS, and SGS agree very well with the exact solution. SU gives a solution that is overdiffuse, but gives a reasonable approximation. LSFEM and Galerkin, on the other hand, give solutions that are far from the exact solution. Figure 3.9 zooms in further on these solutions. It is shown that the Galerkin solution has small magnitude

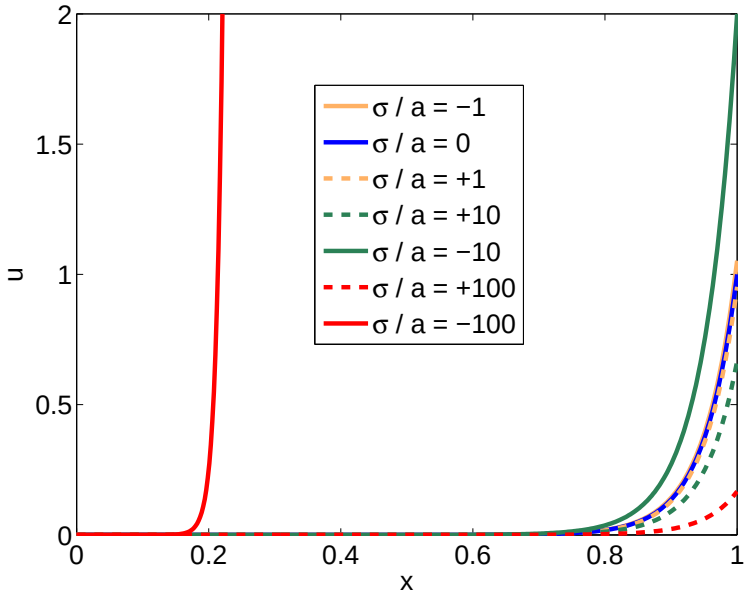

Figure 3.7: Exact solutions for various values of σ.

oscillations, while the other solutions are smooth.

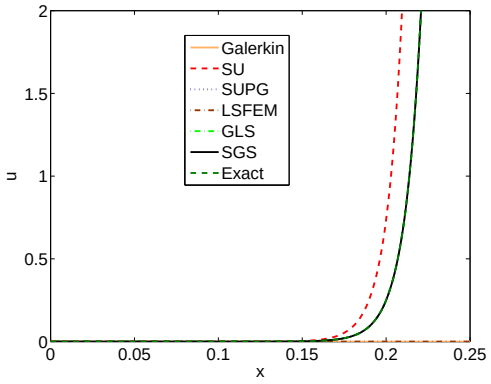

Figure 3.8: Solution to steady state advection-reaction problem using 1024 elements - $\sigma = -100$.

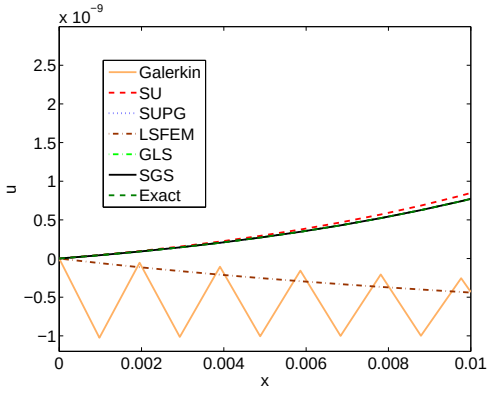

Figure 3.9: Solution to steady state advection-reaction problem using 1024 elements - $\sigma = -100$.

In Figure 3.10 and Figure 3.11, $\sigma = 100$ is used to generate the results. All of the methods agree very well with the exact solution both on the scale of the entire domain (Figure 3.10) and locally (Figure 3.11).

Figure 3.12 shows the solutions using the various FEMs with 1024 elements for $\sigma = -10$. SU, SUPG, GLS and SGS agree well with the exact solution. Galerkin and LSFEM give poor approximations. The Galerkin solution is has small magnitude oscillations as

shown in Figure 3.13.

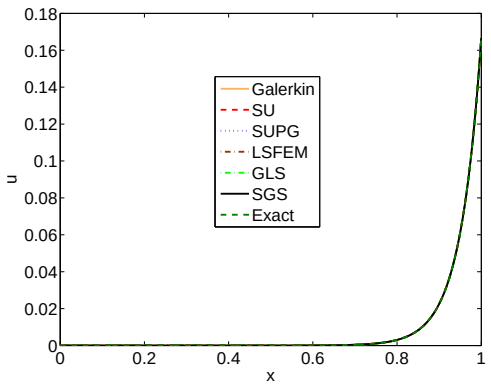

Figure 3.10: Solution to steady state advection-reaction problem using 1024 elements - $\sigma = 100$.

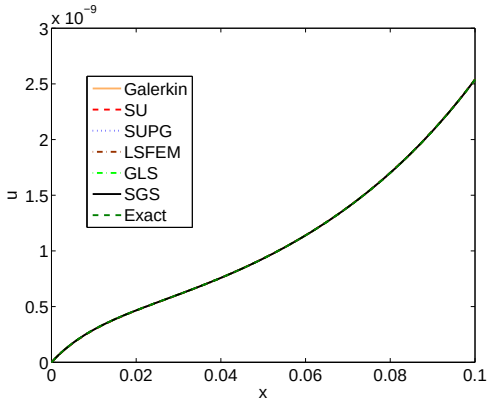

Figure 3.11: Solution to steady state advection-reaction problem using 1024 elements - $\sigma = 100$.

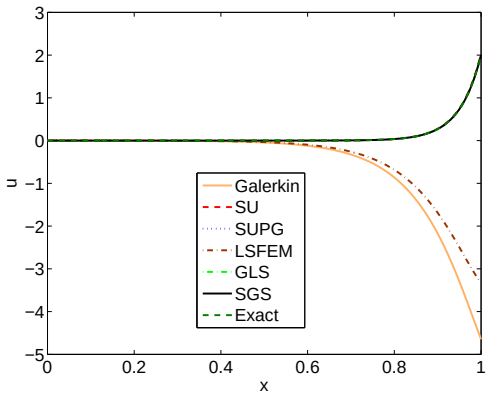

Figure 3.12: Solution to steady state advection-reaction problem using 1024 elements - $\sigma = -10$.

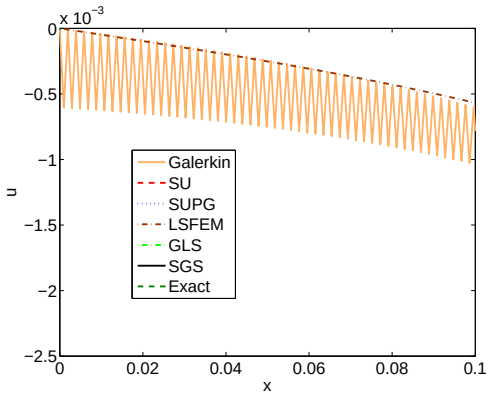

Figure 3.13: Solution to steady state advection-reaction problem using 1024 elements - $\sigma = -10$.

The solutions when $\sigma = 10$ are plotted in Figure 3.14 and Figure 3.15. On the scale of the entire domain all methods appear to give results that are very close the the exact solution, however, upon closer inspection the Galerkin approximation experiences small magnitude oscillations.

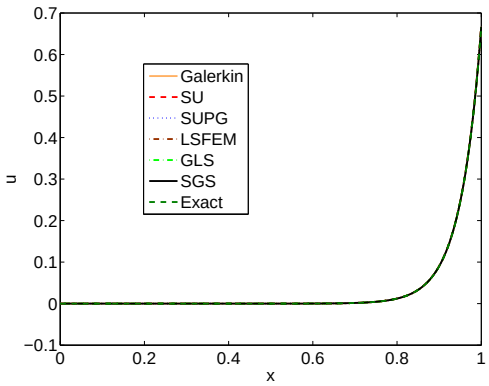

Figure 3.14: Solution to steady state advection-reaction problem using 1024 elements - $\sigma = 10$.

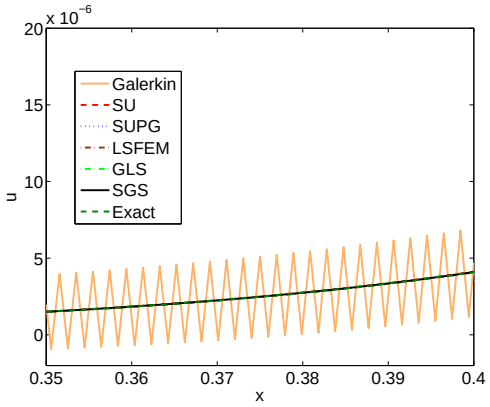

Figure 3.15: Solution to steady state advection-reaction problem using 1024 elements - $\sigma = 10$.

3.9.3 One Dimensional Unsteady Advection Equation

The unsteady advection equation is considered in this example. The governing equation for this problem is given by:

$$\frac{\partial u}{\partial t} + a\frac{\partial u}{\partial x} = s(x,t) \tag{3.58}$$

$$u(x,0) = u_0(x) \text{ on } \Omega \tag{3.59}$$

$$u = u_D \text{ on } \Gamma_D \tag{3.60}$$

$$n\frac{\partial u}{\partial x} = f \text{ on } \Gamma_N \tag{3.61}$$

The FEMs described in this subsection are used to discretize in space. The Finite Difference Method (FDM) is used to discretize in time. The general theta family relationship is given by (3.21).

When $\theta = 0$ the FE time integration is explicit. If $\theta = 0.5$ the method is CN. When $\theta = 1$ the method is BE. CN and BE are implicit methods. The effect of various values of θ will be considered in the next two examples. In addition, the effect of timestep size will be considered.

Example 1

In this example the source function from the previous examples is made time-varying and is given by:

$$s(x,t) = \frac{e^{(x-1)/\epsilon}}{\epsilon(1-e^{-1/\epsilon})}\sin(5t); \tag{3.62}$$

where $\epsilon = 0.05$ [54]

The initial conditions are $u = 0$ throughout the domain. The other properties are the same as from Section 3.9.1. Figure 3.16 shows the results of $\theta = 0$ with $Cr = 0.25$ using 25 elements. SU, SUPG and LSFEM-ST give smooth solutions that are reasonably close to one another. Galerkin and LSFEM-TS, on the other hand are unstable and are not shown here.

When $\theta = 0.5$ the time integration scheme is referred to as the Crank-Nicolson method (CN). The results using CN are shown in Figure 3.17. SU, SUPG, LSFEM-ST and LSFEM-TS give similar solutions to Figure 3.16. Galerkin gives a solution that is very oscillatory. When BE time integration is used the Galerkin oscillations are slightly reduced as shown in Figure 3.18.

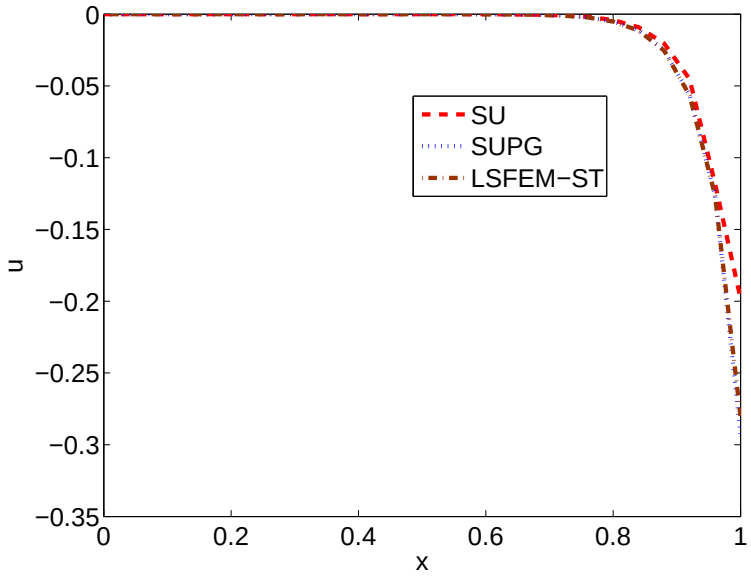

Figure 3.16: One dimensional unsteady advection equation, example 1, $\theta = 0, Cr = 0.25$, 25 elements.

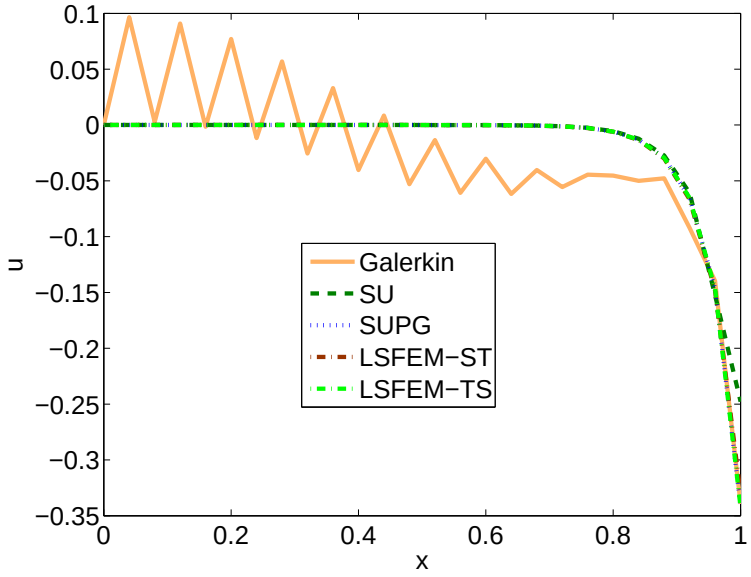

Figure 3.17: One dimensional unsteady advection equation, example 1, $\theta = 0.5, Cr = 1$, 25 elements.

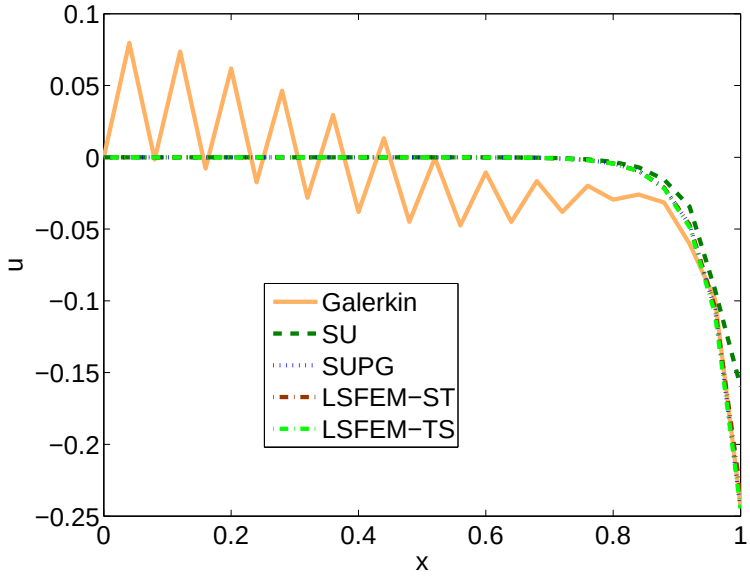

Figure 3.18: One dimensional unsteady advection equation, example 1, $\theta = 1, Cr = 1$, 25 elements.

Example 2

In this example there is no source function and the initial conditions are a step function. The initial step function travels through the domain at a velocity of $a = 1$. Figure 3.19 shows the solutions with $\theta = 0$ for $Cr = 0.1$. Only SU does not show any oscillations. However, the SU approximation is overdiffuse. The largest oscillations occur for Galerkin and LSFEM-TS to the left of the discontinuity. LSFEM-ST gives the largest oscillations to the right of the discontinuity. When $Cr = 1$ the timesteps are too large for the explicit timestepping scheme and thus the Forward Euler scheme gives unstable solutions. This case is not shown.

When $\theta = 0.5$ (CN) the solutions are shown in Figure 3.20 and Figure 3.21. All methods show oscillations except SU. SU appears to be largely unaffected by the size of the timestep.

Backward Euler (BE) ($\theta = 1$) time integration is considered in Figure 3.22 and Figure 3.23 for $Cr = 0.1$ and $Cr = 1$ respectively. When $\theta = 1$ is combined with $Cr = 1$, all methods give better approximations with no visible oscillations. SU gives a slightly more diffuse solution. The apparent large diffusion compared to the exact solution is magnified by the use 25 elements. As the number of elements is increased, the approximation of this sharp front can be improved.

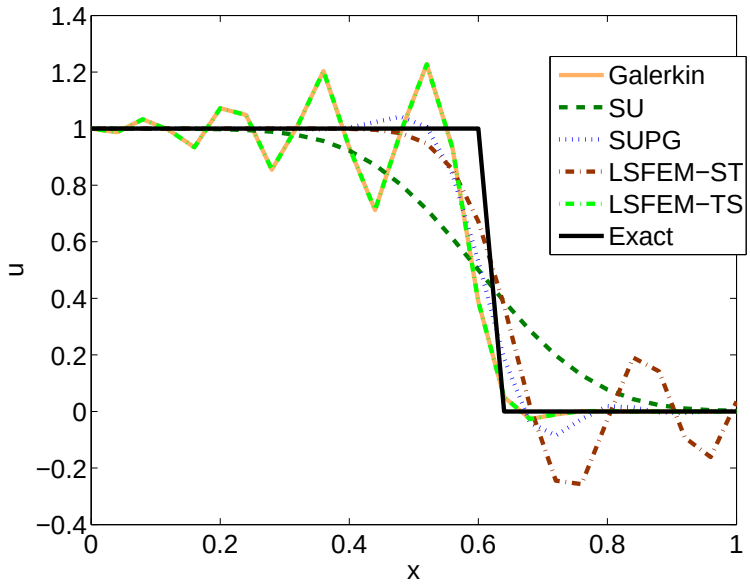

Figure 3.19: One dimensional unsteady advection equation, example 2, $\theta = 0, Cr = 0.1$, 25 elements.

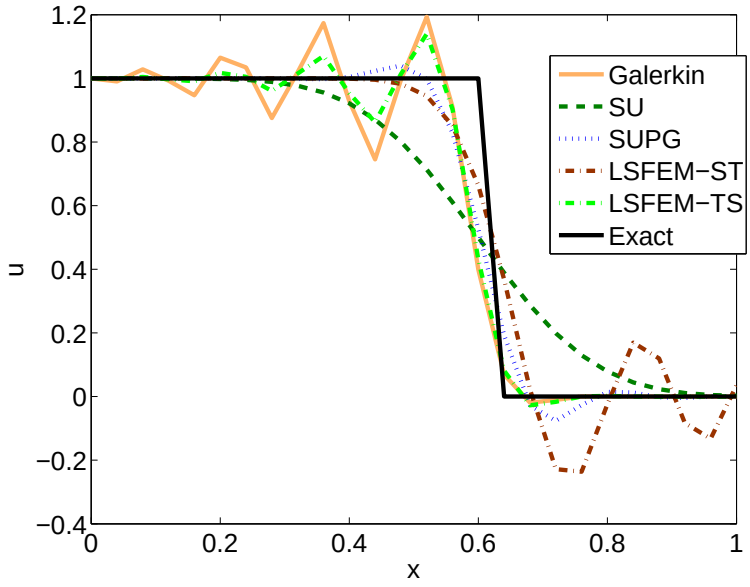

Figure 3.20: One dimensional unsteady advection equation, example 2, $\theta = 0.5, Cr = 0.1$, 25 elements.

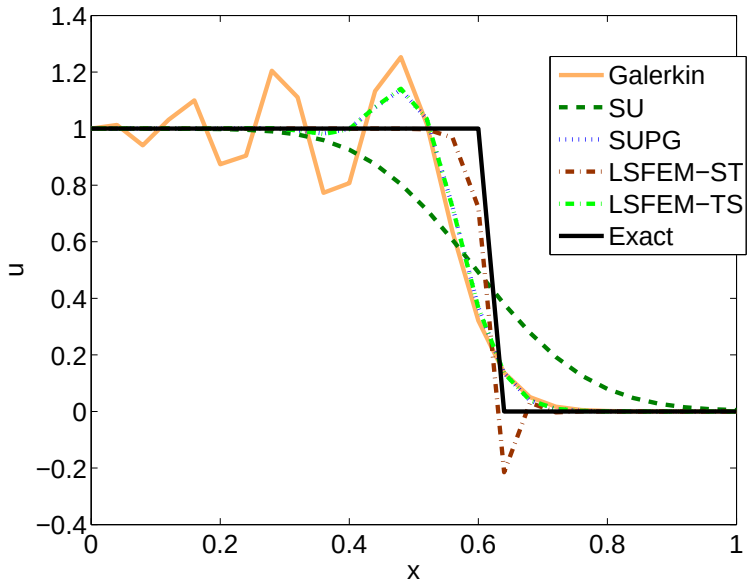

Figure 3.21: One dimensional unsteady advection equation, example 2, $\theta = 0.5, Cr = 1$, 25 elements.

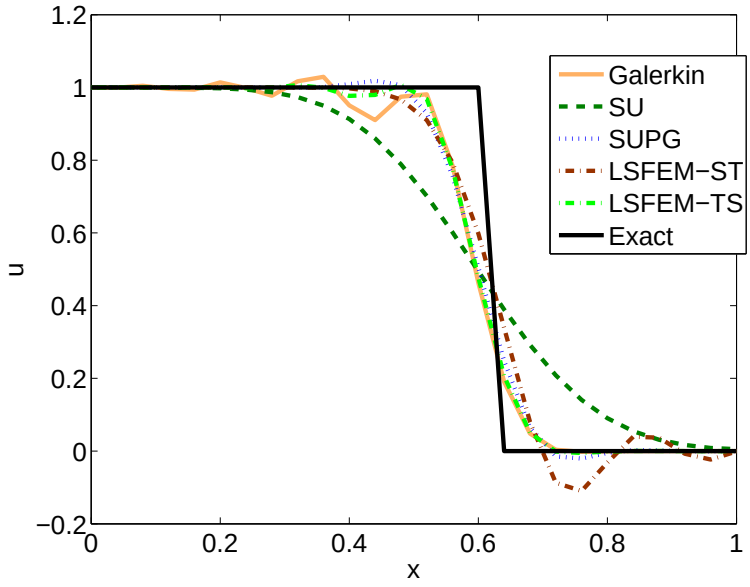

Figure 3.22: One dimensional unsteady advection equation, example 2, $\theta = 1, Cr = 0.1$, 25 elements.

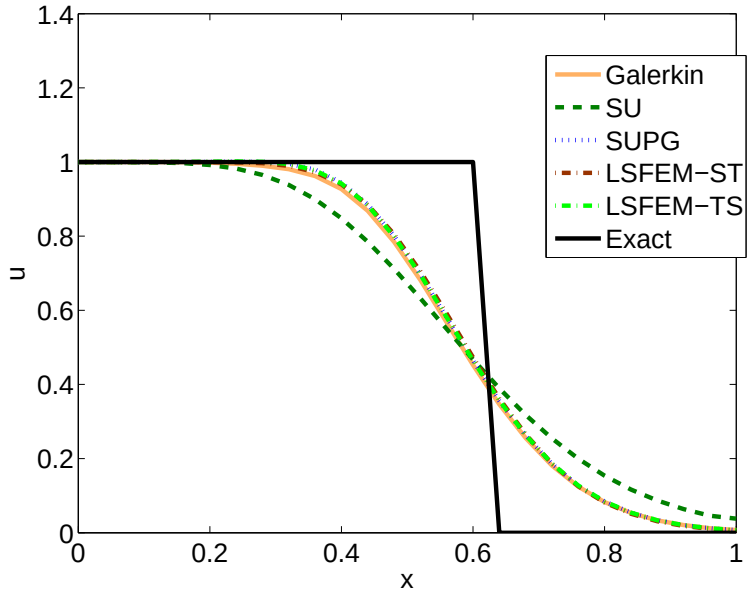

Figure 3.23: One dimensional unsteady advection equation, example 2, $\theta = 1, Cr = 1$, 25 elements.

3.9.4 One Dimensional Unsteady Advection-Reaction Equation

The final examples in this chapter focus on the unsteady version of the advection-reaction equation. The governing equation is the same as the previous section, except that now there is a reaction term present. This equation is given below:

$$\frac{\partial u}{\partial t} + a\frac{\partial u}{\partial x} + \sigma u = s(x,t) \tag{3.63}$$

$$u(x,0) = u_0(x) \text{ on } \Omega \tag{3.64}$$

$$u = u_D \text{ on } \Gamma_D \tag{3.65}$$

$$n\frac{\partial u}{\partial x} = f \text{ on } \Gamma_N \tag{3.66}$$

Example 1

This example is the same as example 1 in the previous section, with the addition of a reaction term. Time integration is conducted in the same manner as discussed in the previous example.

When $\sigma = 10$ the results are shown in Figure 3.24 and Figure 3.25 for CN and BE time integration respectively. The results are very similar. The oscillations in the Galerkin solution are reduced very slightly for BE compared to CN. Only Galerkin gives oscillations in the solutions.

Figure 3.26 and Figure 3.27 show the solutions for $\sigma = -10$ with CN and BE respectively. The results are similar for the two time integration schemes. Galerkin and LSFEM-ST give unstable solutions.

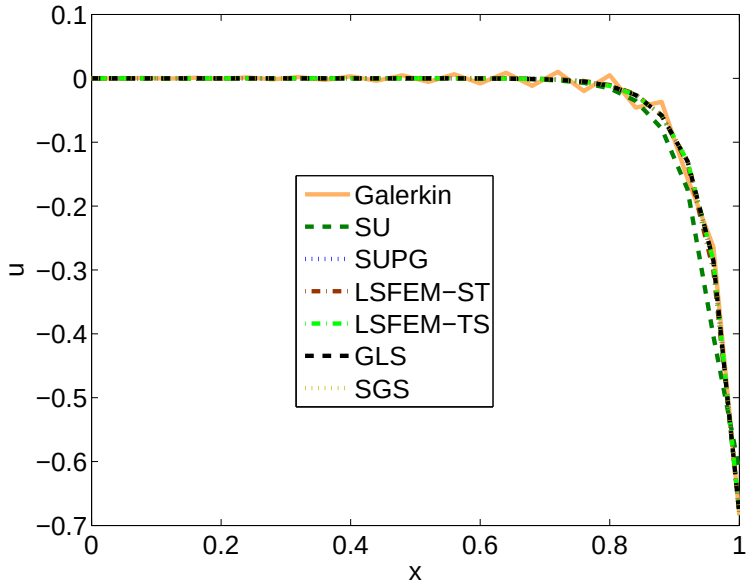

Figure 3.24: One dimensional unsteady advection-reaction equation, example 1, $\theta = 0.5, Cr = 1, \sigma = 10$, 25 elements.

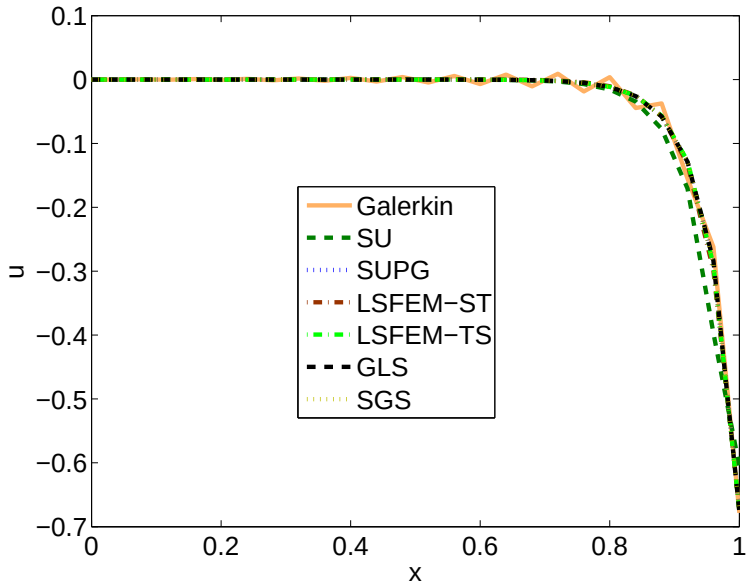

Figure 3.25: One dimensional unsteady advection-reaction equation, example 1, $\theta = 1, Cr = 1, \sigma = 10$, 25 elements.

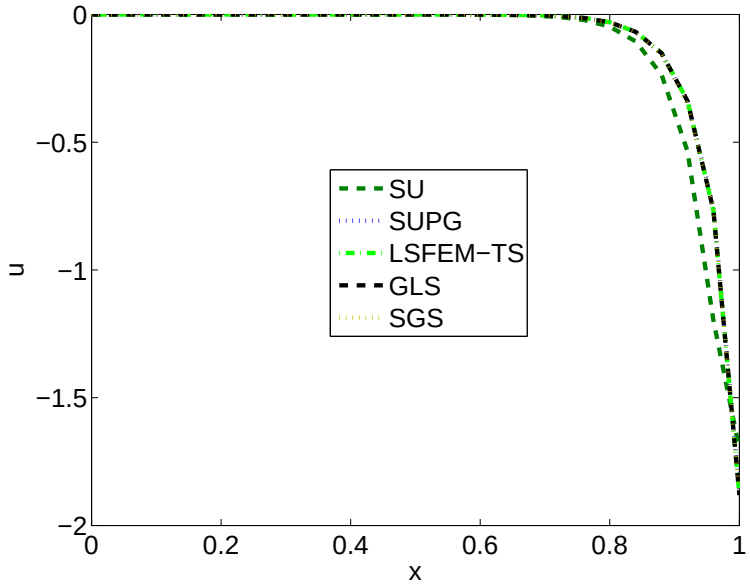

Figure 3.26: One dimensional unsteady advection-reaction equation, example 1, $\theta = 0.5, Cr = 1, \sigma = -10$, 25 elements.

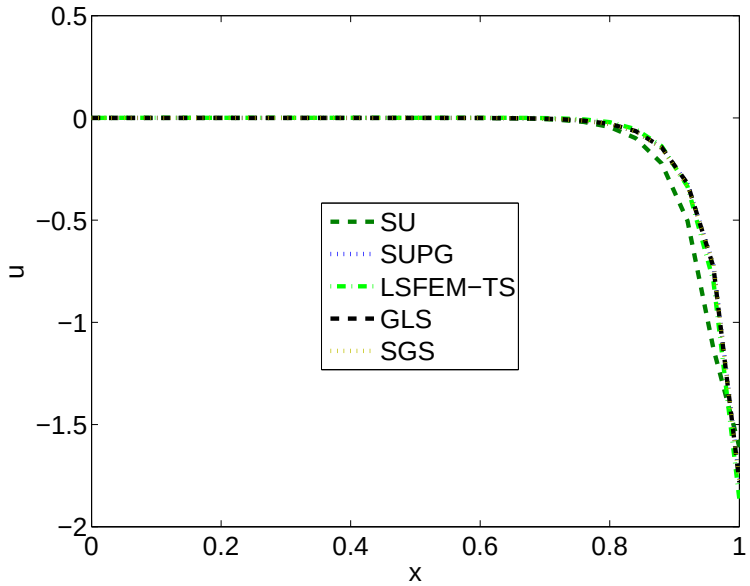

Figure 3.27: One dimensional unsteady advection-reaction equation, example 1, $\theta = 1, Cr = 1, \sigma = -10$, 25 elements.

Example 2

Similar to example 2 in the previous section, the source term is zero and the initial condition is a step function. The main difference here is the addition of the reaction term. The exact solution to this problem is given by:

$$u_{exact}(x,t) = H(at-x)e^{\frac{-\sigma}{a}x} \tag{3.67}$$

where $H()$ is a heaviside function.

Figure 3.28 and Figure 3.29 compare the solution for $\sigma = 1$ when $Cr = 0.1$ and $Cr = 1$ respectively using BE time integration. Larger timesteps generally provide smoother results and give more consistent solutions between the various FEMs. SU is least affected by the size of the timestep.

When $\sigma = -1$ the results are shown in Figure 3.30 and Figure 3.31. Similar to the previous two figures, larger timesteps reduce the magnitude of the oscillations and SU is the least affected by changing the size of the timestep.

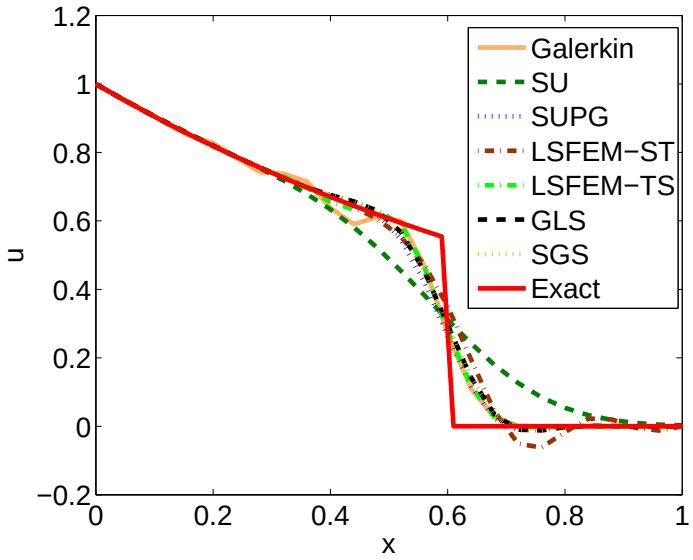

Figure 3.28: One dimensional unsteady advection-reaction equation, example 2, $\theta = 1, Cr = 0.1$, $\sigma = 1$, 25 elements.

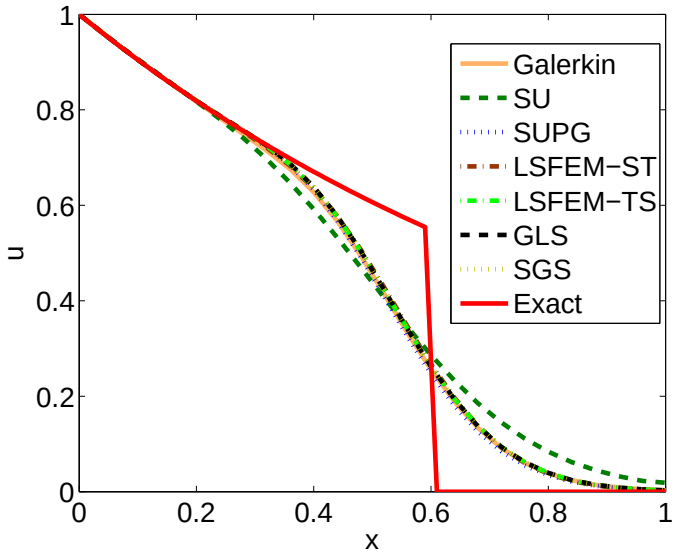

Figure 3.29: One dimensional unsteady advection-reaction equation, example 2, $\theta = 1, Cr = 1$, $\sigma = 1$, 25 elements.

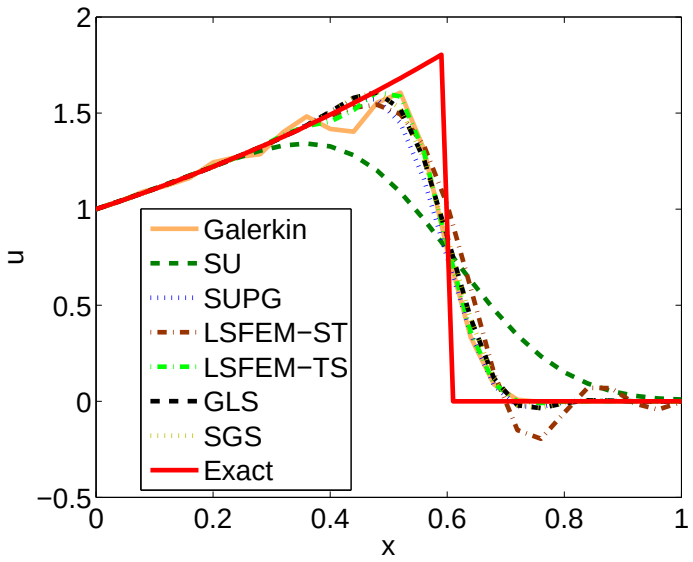

Figure 3.30: One dimensional unsteady advection-reaction equation, example 2, $\theta = 1, Cr = 0.1$, $\sigma = -1$, 25 elements.

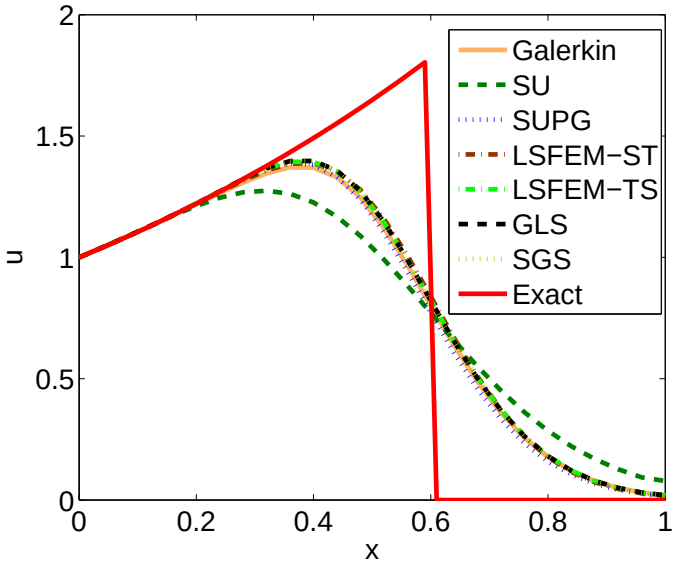

Figure 3.31: One dimensional unsteady advection-reaction equation, example 2, $\theta = 1, Cr = 1$, $\sigma = -1$, 25 elements.

3.10 Chapter Conclusions

In this chapter the steady and unsteady pure advection and advection-reaction equations were considered. Finite Element Method (FEM) discretizations were used to approximate the solutions to the steady state advection equation, the steady state advection-reaction equation, the unsteady advection equation and the unsteady advection-reaction equation. The discretization of the advection term results in non-physical oscillations in the solution from the standard (Galerkin) FEM. These oscillations can be controlled with stabilized FEMs. Several stabilized FEMs were described and compared using four example problems. SU, SUPG, LSFEM, SGS, GLS can be used to stabilize FEM under various scenarios. These stabilization methods were compared with several test problems to give insights into the stabilization properties of these methods, which will be useful as they are used in the next chapter to stabilize the saturation equation. Time integration was performed with the θ-family FDM. In some cases the Galerkin FEM gave seemingly smooth results, but by zooming in small magnitude oscillations are revealed. This was not observed with any of the stabilized FEMs. FE time integration was shown to give unstable results unless small timesteps are used. The magnitude of the oscillations from the various FEMs were the least when BE time integration was used. Oscillations were found to be significantly reduced when BE is combined with relatively large timesteps ($Cr = 1$). SU gave the most robust solutions across the range of examples considered. However, SU can give overdiffuse solutions. The presence of a reaction term was shown that it can increase the magnitude of the non-physical oscillations.

The stabilized FEMs considered in this chapter will be used in Chapter 5 and Chapter 6 in order to stabilize the resulting oscillations that occur during the Galerkin FEM discretization of vertically averaged multiphase flow equations.

Chapter 4

Carbon Sequestration Injection Simulations using a Stabilized Finite Element Method Framework in Quasi-Two Dimensions

This chapter is based on two journal articles:

C. Ladubec and R. Gracie, "Stabilized Finite Element Methods for Vertically Averaged Multiphase Flow for Carbon Sequestration", Submitted, 2015.

C. Ladubec and R. Gracie, "Vertically Averaged Multiphase Flow Simulations for Carbon Sequestration using Stabilized Finite Element Methods and Quadratic Elements", Submitted, 2016.

In these articles I was the first author where I led the writing of the journal articles. In addition, I lead the development of the MATLAB code, and the development of the formulations.

This chapter addresses objectives 1 and 2 (see Chapter 1) of the thesis:

- Develop a computationally efficient numerical model for carbon sequestration based on a Finite Element Method framework using a vertically averaged formulation.

- Effectively deal with instabilities and oscillations that occur from FEM approximations of the advection equation and the coupled nature of this problem.

4.1 Introduction

The properties of saline aquifers are highly uncertain because of the large size of the domains, the difficulty in measuring system properties and the high degree of heterogeneity. As such, stochastic simulations are required during storage site assessments [90]. In addition, there is a great deal of uncertainty associated with the location and properties of leakage pathways. Stochastic approaches require a large number of simulations (using many different sets of system parameters), dramatically increasing the computational cost of modelling for site assessment purposes. Therefore, computationally efficient numerical schemes for modelling CO_2 sequestration are needed.

A vertically averaged multiphase flow formulation [3] allows for a significant reduction in the computational cost by reducing the dimensionality of the problem (e.g., from three dimensions to quasi-three dimensions or two dimensions to quasi-two dimensions). The vertically averaged formulation is comprised of two non-linear coupled partial differential equations (PDEs) that define the mass balance of the CO_2 and the brine phases. The governing equations can be solved either simultaneously, or by using a sequential solution strategy. Solving the coupled equations simultaneously creates a very large system of equations that has a large computational cost associated with it. In order to reduce the computational burden a sequential solution strategy may be utilized. The system of equations can be manipulated to result in an elliptical equation (i.e., a Poisson equation) that governs the pressure in the system and a hyperbolic equation (i.e., an advection equation) that describes the evolution of the average brine saturation [41].

It is well known that the Galerkin Finite Element Method can produce non-physical oscillations when used to obtain numerical solutions of advection-dominated PDEs. The Galerkin FEM discretization of the saturation equation can achieve smooth solutions with the proper selection of element size and timestep. However, it will be demonstrated that the Galerkin FEM can lead to solutions with spurious oscillations and often cannot be used when the CO_2 plume encounters a Dirichlet boundary or when multiple plumes mix, as occurs in the presence of multiple injection wells.

Many solutions exist in the literature to stabilize the Finite Element Method to obtain satisfactory solutions to advection-dominated problems. A good overview of the subject is presented in [71]. A large number of approaches have been used in literature to stabilize the Galerkin FEM. The more common approaches include the Streamline Upwind (SU) method [73], the Streamline Upwind Petrov Galerkin (SUPG) method [73], the Least Squares Finite Element Method (LSFEM) [74, 75, 76], the Subgrid Scales (SGS) method [77, 78] and the Galerkin Least Squares (GLS) method [79]. SU and SUPG were originally presented considering steady-state and transient advection-diffusion equations [73]. LSFEM was presented as a means to provide stabilized solutions to the steady state advection-reaction equation [74], and the transient advection equation [75]. GLS was proposed as a stabilization method for advection-diffusion problems [79]. SGS was presented as a method to stabilize the advection-diffusion equation and the Helmholtz equation (a diffusion-reaction equation) [77, 78]. Other approaches include Upwinding [80, 81], the Taylor-Galerkin method [82], Bubble Functions [83], the Discontinuous Galerkin (DG) method [85], and Finite Increment Calculus [84].

The multitude of stabilization techniques give a great deal of possible approaches to providing a stabilized Finite Element approximation of an advection equation. Each ap-

proach has its advantages and disadvantages. Typically stabilization methods are best suited to a particular problem, and often are inadequate for other problems. In addition, the stabilization methods in the literature are often optimized for linear uncoupled systems where the advection term is constant in time and space. In the case of carbon sequestration considered here the governing equations are non-linear, coupled, and the advection velocity is not constant. Determining the ideal stabilization method for a given problem can be non-trivial. Stabilization is more challenging for the advection equation considered here since there is no diffusion term.

The use of linear elements results in incomplete forms of the SUPG and LSFEM discretizations. This loss of information may affect the stabilization properties of the SUPG and LSFEM methods. When linear elements are used SUPG, GLS and SGS all result in the same formulation. Quadratic elements allow for GLS and SGS stabilizations, and permit more complete forms of SUPG and LSFEM stabilizations.

In this chapter, a coupled system of non-linear PDEs is considered where the advection velocity varies with space and time. The pressure is approximated using the Galerkin FEM, while the saturation equation is discretized in time using the θ-family of Finite Difference Methods (FDMs) and in space using the FEM and various stabilized FEMs. The various spatial discretization methods for the saturation equation are compared and the advantages and disadvantages are highlighted. Stabilization has not been previously studied in detail for these equations. The selection of appropriate stabilization methods is highly problem dependent. Furthermore, the optimization of stabilization methods and associated stabilization parameters have typically focused on linear, uncoupled equations with constant advection velocity. Therefore, the performance of various stabilization methods needs to be assessed in the context of the vertically averaged multiphase flow

equations. While the performance of the various stabilization methods discussed above may be hypothesized, an actual study of their behaviour is required. Such a study is presented in this chapter. Due to the complexity of the resulting non-linear coupled discrete equations, stabilization is studied here in a one dimensional (quasi-two dimensional) context.

4.2 Governing Equations in One Dimension (Quasi-Two Dimensions)

The problem consists of simulating the injection of CO_2 into a deep saline aquifer and solving for the pressure and saturation distributions over time. A description of the carbon sequestration system considered in this chapter is shown in Figure 4.1. The multiphase flow system [3] is described by the mass balance of each phase. The CO_2 and brine mass balance equations are given by:

$$\phi(1 - S_B)\frac{\partial h_C}{\partial t} + \frac{\partial \hat{q}_C}{\partial x} = Q_{inj}(t)\delta(x - x_{inj}) \tag{4.1}$$

$$\phi(1 - S_B)\frac{\partial h_B}{\partial t} + \frac{\partial \hat{q}_B}{\partial x} = 0 \tag{4.2}$$

where ϕ is the porosity of the aquifer, S_B is the brine residual saturation, $h_C(x,t)$ is the depth of CO_2 and $h_B(x,t)$ is the depth of brine as a functions of time and space, $Q_{inj}(t)$ is the rate of CO_2 injection, $\delta()$ is Dirac's delta function, and x_{inj} is the coordinates of the injection well. The vertically integrated CO_2 and brine fluxes, $\hat{q}_C$ and $\hat{q}_B$ are respectively given by:

$$\hat{q}_C = -h_C\frac{kk_C^{rel}}{\mu_C}\left(\frac{\partial p_{bot}}{\partial x} - \rho_B g\frac{\partial H}{\partial x} + \Delta\rho g\frac{\partial h_C}{\partial x} + \rho_C g\frac{\partial z_{top}}{\partial x}\right) \tag{4.3}$$

$$\hat{q}_B = -h_B \frac{k}{\mu_B} \left(\frac{\partial p_{bot}}{\partial x} + \rho_B g \frac{\partial z_{bot}}{\partial x} \right) \tag{4.4}$$

where k is the permeability of the rock matrix of the aquifer, k_C^{rel} is the relative permeability of CO_2, μ_C is the viscosity of CO_2, μ_B is the brine viscosity, p_{bot} is the pressure along the the bottom boundary of the aquifer, ρ_B and ρ_C are the densities of brine and CO_2 respectively, $\Delta\rho = \rho_B - \rho_C$, g is the gravitational constant, H is the aquifer thickness, and z_{top} and z_{bot} are the depths of the top and bottom boundaries of the aquifer respectively.

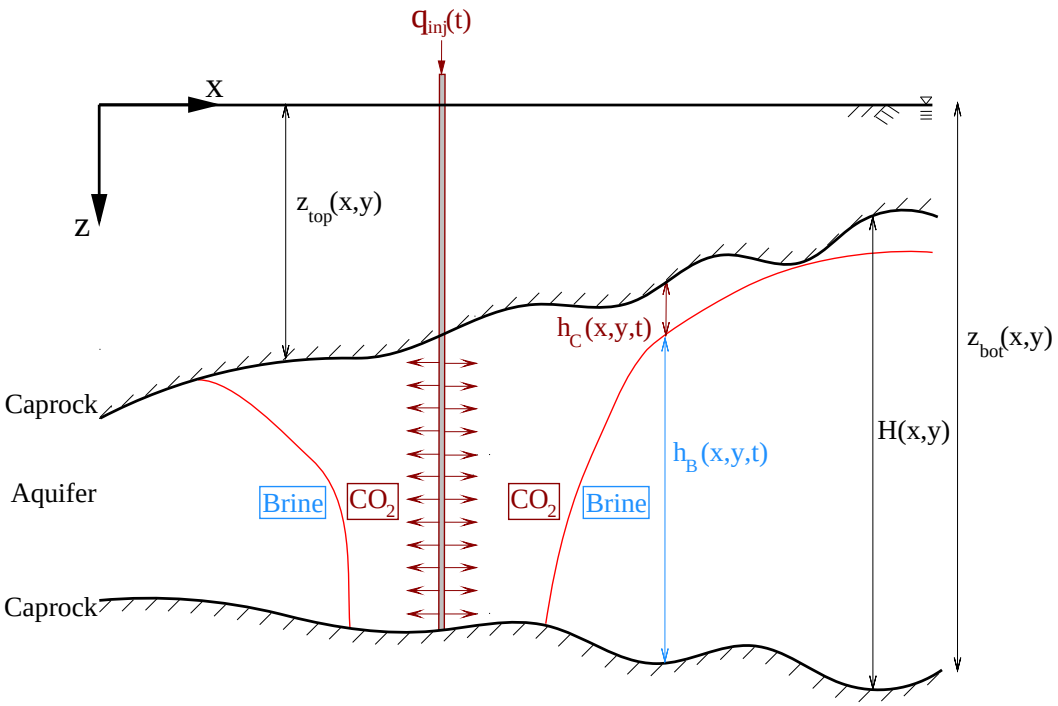

Figure 4.1: Parameters of carbon sequestration model [4].

The mass balance equations (4.1) and (4.2) are combined with with the flux equations (4.3) and (4.4). These equations are then manipulated in the same way as described in [41] to obtain a pressure equation and a saturation equation.

4.3 Pressure Equation

The pressure equation is determined by adding (4.1) and (4.2), as in [41]. The unsteady terms $\phi(1-S_B)\frac{\partial h_C}{\partial t}$ and $\phi(1-S_B)\frac{\partial h_B}{\partial t}$ cancel, and what is left is a elliptical equation. The strong form of the pressure equation is find $p_{bot}(x,t)$ such that:

$$\begin{aligned} -\frac{\partial}{\partial x}\left(h_C\frac{kk_{REL}^C}{\mu_C}\left(\frac{\partial p_{bot}}{\partial x}+\Delta\rho g\frac{\partial h_C}{\partial x}-\rho_B g\frac{\partial H}{\partial x}+\rho_C g\frac{\partial z_{top}}{\partial x}\right)\right) \\ -\frac{\partial}{\partial x}\left(h_B\frac{k}{\mu_B}\left(\frac{\partial p_{bot}}{\partial x}+\rho_B g\frac{\partial z_{bot}}{\partial x}\right)\right)=q_C^{inj}, \quad x\in\Omega \end{aligned} \tag{4.5}$$

and

$$p_{bot}(x,t)=\overline{p}_{bot}(x,t) \text{ on } \Gamma_p \tag{4.6}$$

$$\hat{q}_C(x,t)n=\overline{q}_C(x,t) \text{ on } \Gamma_q \tag{4.7}$$

$$\hat{q}_B(x,t)n=\overline{q}_B(x,t) \text{ on } \Gamma_q \tag{4.8}$$

where Ω is the entire domain of the problem, $\Gamma_p\cup\Gamma_q$ is the boundary of Ω, $\Gamma_p\cap\Gamma_q=\emptyset$, and n is a unit normal to Γ_q.

4.3.1 Weak Form

In order to derive the FEM formulation, the strong form is converted to a weak form. The weak form of the pressure equation for the pressure at the bottom of the aquifer (4.5) is:

find $p_{bot}(x,t) \in U$ such that:

$$\int_\Omega \frac{\partial \delta p_{bot}}{\partial x} h_B \frac{k}{\mu_B} \frac{\partial p_{bot}}{\partial x} d\Omega + \int_\Omega \frac{\partial \delta p_{bot}}{\partial x} h_B \frac{k}{\mu_B} \rho_B g \frac{\partial z_{bot}}{\partial x} d\Omega + \int_\Omega \frac{\partial \delta p_{bot}}{\partial x} h_C \frac{k k_C^{rel}}{\mu_C} \Delta\rho g \frac{\partial h_C}{\partial x} d\Omega$$
$$- \int_\Omega \frac{\partial \delta p_{bot}}{\partial x} h_C \frac{k k_C^{rel}}{\mu_C} \rho_B g \frac{\partial H}{\partial x} d\Omega + \int_\Omega \frac{\partial \delta p_{bot}}{\partial x} h_C \frac{k k_C^{rel}}{\mu_C} \rho_C g \frac{\partial z_{top}}{\partial x} d\Omega + \int_\Omega \frac{\partial \delta p_{bot}}{\partial x} h_C \frac{k k_C^{rel}}{\mu_C} \frac{\partial p_{bot}}{\partial x} d\Omega$$
$$= \int_\Omega \delta p_{bot} Q_{inj}(t) \delta(x - x_{inj}) d\Omega + \left(\delta p_{bot} \left(\overline{q}_B + \overline{q}_C \right) \right) \Big|_{\Gamma_p}, \forall \delta p_{bot} \in U_0. \tag{4.9}$$

The function spaces are given as:

$$\begin{aligned} U &= \{ p_{bot}(x) | p_{bot}(x) \in H^1 \backslash \Omega^{well}, p_{bot}(x) = \overline{p}_{bot} \text{ on } \Gamma_p \} \\ U_0 &= \{ \delta p(x) | \delta p(x) \in H^1 \backslash \Omega^{well}, \delta p(x) = 0 \text{ on } \Gamma_p \} \end{aligned} \tag{4.10}$$

These spaces have been used in similar problems, but the author is not aware of any proof that these spaces are correct.

4.3.2 FEM Discretization

From the weak form (4.9) one can arrive at a Galerkin Finite Element Method (FEM) discrete pressure equation. The FEM approximation of pressure is taken as:

$$p^h(x) = \sum_{I \in \mathcal{N}} N_I(x) p_I, x \in \Omega \tag{4.11}$$

where $N_I(x)$ are the shape functions for three-node quadratic elements, p_I is the pressure at the node I and $\mathcal{N}$ is the set of all nodes in the domain Ω. The pressure approximation can be expressed in matrix form as:

$$p^h(x) = \mathbf{N} \mathbf{p}_{bot} \tag{4.12}$$

where $\mathbf{N}$ contains the shape functions for all nodes and

$$\mathbf{p}_{bot}^{\mathsf{T}} = \{p_1, p_2, ..., p_{nn}\} \tag{4.13}$$

where nn is the total number of nodes in $\mathcal{N}$.

Substituting (4.12) into (4.9) the FEM discretization of the pressure equation can be determined as:

$$\mathbf{K}_p \mathbf{p}_{bot} = \mathbf{F}_p \tag{4.14}$$

$$\mathbf{F}_p = \mathbf{F}_{p1} + \mathbf{F}_{p2} + \mathbf{F}_{p3} + \mathbf{F}_{p4} \tag{4.15}$$

where $\mathbf{K}_p$ is the diffusion matrix, $\mathbf{F}_p$ is the total flux vector, which is composed of: $\mathbf{F}_{p1}$ - the injection flux vector, $\mathbf{F}_{p2}$ - the boundary flux vector, $\mathbf{F}_{p3}$ - the buoyancy flux vector, and $\mathbf{F}_{p4}$ - the slope flux vector.

The matrices and vectors defined in the previous two equations are:

$$\mathbf{K}_p^e = \int_{\Omega^e} \mathbf{B^e}^{\mathsf{T}} \left(\frac{h_C k_C^{rel}}{\mu_C} + \frac{h_B}{\mu_B} \right) k \mathbf{B^e} d\Omega^e \tag{4.16}$$

$$\mathbf{F}_{p1}^e = \int_{\Omega^e} \mathbf{N^e}^{\mathsf{T}} Q_{inj}(t) \delta(x - x_{inj}) d\Omega^e \tag{4.17}$$

$$\mathbf{F}_{p2}^e = \mathbf{N^e}^{\mathsf{T}} \left(\overline{q}_B + \overline{q}_C \right) \Big|_{\Gamma_p^e} \tag{4.18}$$

$$\mathbf{F}_{p3}^e = - \int_{\Omega^e} \mathbf{B^e}^{\mathsf{T}} \frac{k k_C^{rel}}{\mu_C} \Delta \rho g h_C \frac{\partial h_C}{\partial x} d\Omega^e \tag{4.19}$$

$$\mathbf{F}_{p4}^e = \int_{\Omega^e} \mathbf{B^e}^{\mathsf{T}} \left(h_C \frac{k k_C^{rel}}{\mu_C} \left(\rho_B g \frac{\partial H}{\partial x} - \rho_C g \frac{\partial z_{top}}{\partial x} \right) - h_B \frac{k}{\mu_B} \rho_B g \frac{\partial z_{bot}}{\partial x} \right) d\Omega^e \tag{4.20}$$

where $\mathbf{N^e}$ and $\mathbf{B^e}$ are the shape functions and the shape function derivatives for element e and Ω^e is the domain of element e.

4.4 Saturation Equation

The strong form of the saturation equation for the brine phase is given by combining (4.2) and (4.4), resulting in:

$$\frac{\partial h_B}{\partial t} = \frac{1}{\phi(1-S_B)\mu_B}\left(\left(\frac{\partial p_{bot}}{\partial x} + \rho_B g \frac{\partial z_{bot}}{\partial x}\right)\frac{\partial h_B}{\partial x} + \left(\frac{\partial^2 p_{bot}}{\partial x^2} + \rho_B g \frac{\partial^2 z_{bot}}{\partial x^2}\right) h_B\right), \quad x \in \Omega,\ \mathrm{t}\ \in [0, t_{end}] \tag{4.21}$$

$$h_B(x,t) = \overline{h}_B(x,t) \text{ on } \Gamma_h \tag{4.22}$$

$$\hat{q}_B(x,t)n = \overline{q}_B(x,t) \text{ on } \Gamma_q \tag{4.23}$$

$$h_B(x,0) = h_{Bo}(x) \text{ on } \Omega \tag{4.24}$$

where $\overline{h}_B(x,t)$ is the specified Dirichlet boundary condition on the boundary Γ_h, $\overline{q}_B(x,t)$ is the prescribed brine flux on the Neumann boundary Γ_q, and $h_{Bo}(x)$ is the initial brine depth throughout the domain Ω. On the right hand side of the equation the first term in the brackets is the advection term and the second term is the reaction term.

4.4.1 Galerkin Method

The strong form from the previous section is converted to a weak form, which is then discretized using the Galerkin Finite Element Method. Green's Formula is used to reduce the order of the second derivatives that appear in the reaction term. The advection and reaction terms become a combined advection-reaction term and a boundary integral. The boundary integral is zero for Dirichlet boundaries. The Galerkin weak form is given by:

find $h_B(x,t) \in W$ such that

$$\int_\Omega \delta h_B \frac{\partial h_B}{\partial t} d\Omega - \int_\Omega \frac{\partial \delta h_B}{\partial x} a h_B d\Omega = \left(\delta h_B \frac{1}{\phi(1-S_B)} \overline{q}_B \right) \Big|_{\Gamma_q}, \forall \delta h_B \in W_0. \tag{4.25}$$

where δh_B is the weight function W and W_0 are the appropriate function spaces for h_B and δh_B, and a is the advective velocity given by:

$$a = -\frac{k}{\phi(1-S_B)\mu_B} \left(\frac{\partial p_{bot}}{\partial x} + \rho_B g \frac{\partial z_{bot}}{\partial x} \right) \tag{4.26}$$

The Courant number is given by:

$$Cr = \frac{a\Delta t}{\Delta x} \tag{4.27}$$

where Δt is the timestep size and Δx is the element size.

The FEM approximation for the depth of brine is given by:

$$h_B^h(x,t) = \sum_{I \in \mathcal{N}} N_I(x) h_I(t) \tag{4.28}$$

where $N_I(x)$ is the shape function for one dimensional three-node quadratic elements, $h_I(t)$ is the brine depth at the node I (which is a function of time) and $\mathcal{N}$ is the set of all nodes in the domain Ω.

The brine depth approximation can be expressed in matrix form as:

$$h_B^h(x,t) = \mathbf{N}\mathbf{h_B} \tag{4.29}$$

where $\mathbf{N}$ contains the shape functions for all nodes and

$$\mathbf{h_B}^{\mathsf{T}} = \{h_1, h_2, ..., h_{nn}\} \tag{4.30}$$

where nn is the total number of nodes in $\mathcal{N}$.

By substituting the FEM approximation of brine depth given by (4.29) into (4.25), and using the same form for the weight functions, the Galerkin FEM discretization results in the following system of semi-discrete equations:

$$[\mathbf{C}_\alpha]\{\dot{\mathbf{h_B}}\} + [\mathbf{K}_\alpha]\{\mathbf{h_B}\} = \{\mathbf{F}_\alpha\} \tag{4.31}$$

where $\mathbf{C}_\alpha$ is the storage matrix, $\mathbf{K}_\alpha$ is the advection-reaction matrix, $\mathbf{F}_\alpha$ is the flux vector, $\mathbf{h_B}$ is the nodal brine depths, $\dot{\mathbf{h_B}}$ is the time derivative of the depth of brine, and α signifies the spatial discretization method - Galerkin, SU, SUPG, LSFEM, GLS, or SGS.

After discretizing the above equation in time using the Finite Difference Method (FDM), the system of equations to solve becomes:

$$\begin{aligned}\left([\mathbf{C}_\alpha] + \Delta t\theta[\mathbf{K}_\alpha]^{n+1}\right)\{\mathbf{h_B}\}^{n+1} = \Big(\left([\mathbf{C}_\alpha] - \Delta t\,(1-\theta)\,[\mathbf{K}_\alpha]^{n+1}\right)\{\mathbf{h_B}\}^{n} \\ + \Delta t\left(\theta\{\mathbf{F}_\alpha\}^{n+1} + (1-\theta)\,\{\mathbf{F}_\alpha\}^{n}\right)\Big)\end{aligned} \tag{4.32}$$

where Δt is the timestep size, θ determines the type of time integration ($\theta = 0$ for the Forward Euler method (FE), $\theta = 0.5$ for the Crank-Nicolson method (CN) and $\theta = 1$ for the Backward Euler method (BE), $n+1$ denotes the current timestep, and n denotes the previous timestep.

The matrices associated with the Galerkin spatial discretization of (4.25) are given by:

$$\mathbf{K}_G^e = -\int_{\Omega^e} \mathbf{B}^{\mathbf{e}\mathsf{T}} a \mathbf{N}^{\mathbf{e}} d\Omega^e \tag{4.33}$$

$$\mathbf{C}_G^e = \int_{\Omega^e} \mathbf{N}^{\mathbf{e}\mathsf{T}} \mathbf{N}^{\mathbf{e}} d\Omega^e \tag{4.34}$$

$$\mathbf{F}_G^e = \left(\mathbf{N}^{\mathbf{e}\mathsf{T}} \frac{1}{\phi(1-S_B)} \overline{q}_B \right) \Big|_{\Gamma_q^e} \tag{4.35}$$

4.4.2 Stabilization Methods

In order to eliminate the non-physical oscillations that can occur with a Galerkin FEM approximation, several stabilized FEMs are examined. The following methods will be considered: the Streamline Upwind (SU) method [73], the Streamline Upwind Petrov Galerkin (SUPG) method [73], the Least Squares Finite Element Method (LSFEM) [74, 75, 76], the Galerkin Least Squares (GLS) method [79], and the Subgrid Scales (SGS) method [77, 78]. Each stabilization method can be considered as the original (Galerkin) weak form of the problem (4.25) with an additional stabilization term that is composed of a perturbation operator and a residual. Various options are available and these choices define the various stabilized methods that are considered in this thesis. The additional stabilization term can be generalized by the following form:

$$\sum_e \int_{\Omega^e} P(\delta h_B) R(h_B) d\Omega^e \tag{4.36}$$

where $P(\delta h_B)$ is a perturbation function and $R(h_B)$ is the residual. The choice of $P(\delta h_B)$ and $R(h_B)$ differentiates the various stabilized methods examined in this chapter.

The weak form for the stabilized methods is obtained by adding (4.36) to (4.25). The

weak form then becomes find $h_B(x,t) \in W$ such that:

$$\begin{aligned}&\int_\Omega \delta h_B \frac{\partial h_B}{\partial t} d\Omega - \int_\Omega \frac{\partial \delta h_B}{\partial x} a h_B d\Omega + \sum_e \int_{\Omega^e} P(\delta h_B) R(h_B) d\Omega^e \\ &= \left(\delta h_B \frac{1}{\phi(1-S_B)} \overline{q}_B \right) \Big|_{\Gamma_q}, \; \forall \delta h_B \in W_0.\end{aligned} \tag{4.37}$$

where W and W_0 are the appropriate function spaces for h_B and δh_B.

In the sections that follow the perturbation function and the residual for each of the stabilized methods are discussed. The resulting matrices of the discretization are also presented.

The Streamline Upwind (SU) and Streamline Upwind Petrov Galerkin (SUPG) Methods

The Streamline Upwind (SU) and Streamline Upwind Petrov Galerkin (SUPG) methods share the same perturbation function in (4.36) and (4.37). The perturbation function is given by:

$$P^{SU}(\delta h_B) = P^{SUPG}(\delta h_B) = \tau a \frac{\partial \delta h_B}{\partial x} \tag{4.38}$$

where τ is the stabilization parameter, and δh_B is the weight function.

The definition of τ used in this study is adopted from [91] to account for the reaction term in (4.21).

$$\tau^e = \left(\left(\frac{1}{\theta \Delta t} \right)^2 + \left(\frac{2a}{h^e} \right)^2 + \sigma^2 \right)^{-\frac{1}{2}} \tag{4.39}$$

where h^e is a measure of element size and σ is the reaction term of the residual and is given by:

$$\sigma = -\frac{k}{\phi(1-S_B)\mu_B} \left(\frac{\partial^2 p_{bot}}{\partial x^2} + \rho_B g \frac{\partial^2 z_{bot}}{\partial x^2} \right) \tag{4.40}$$

The distinguishing feature of SU and SUPG is the form of their residuals. SUPG uses the complete residual of (4.21), while the residual for SU only includes the advective term. SUPG consistently applies the perturbation operation to all terms in the residual and thus it is called a consistent stabilization method. SU on the other hand is an inconsistent stabilization method. The residual for SUPG and SU are given by:

$$R^{SUPG}(h_B) = \frac{\partial h_B}{\partial t} + a\frac{\partial h_B}{\partial x} + \sigma h_B \tag{4.41}$$

$$R^{SU}(h_B) = a\frac{\partial h_B}{\partial x} \tag{4.42}$$

The resulting matrices for the spatial discretization of (4.37) are given by

$$\mathbf{K}_{SUPG}^{e,stab} = \int_{\Omega^e} \mathbf{B^e}^\mathsf{T} \tau a^2 \mathbf{B^e} d\Omega^e + \int_{\Omega^e} \mathbf{B^e}^\mathsf{T} \tau a \sigma \mathbf{N^e} d\Omega^e \tag{4.43}$$

$$\mathbf{K}_{SUPG} = \mathbf{K}_G + \mathbf{K}_{SUPG}^{stab} \tag{4.44}$$

$$\mathbf{K}_{SU}^{e,stab} = \int_{\Omega^e} \mathbf{B^e}^\mathsf{T} \tau a^2 \mathbf{B^e} d\Omega^e \tag{4.45}$$

$$\mathbf{K}_{SU} = \mathbf{K}_G + \mathbf{K}_{SU}^{stab} \tag{4.46}$$

$$\mathbf{C}_{SUPG}^{e,stab} = \int_{\Omega^e} \mathbf{B^e}^\mathsf{T} \tau a \mathbf{N^e} d\Omega^e \tag{4.47}$$

$$\mathbf{C}_{SUPG} = \mathbf{C}_G + \mathbf{C}_{SUPG}^{stab} \tag{4.48}$$

$$\mathbf{C}_{SU} = \mathbf{C}_G \tag{4.49}$$

$$\mathbf{F}_{SUPG} = \mathbf{F}_{SU} = \mathbf{F}_G \tag{4.50}$$

The Galerkin Least Squares Method (GLS)

The Galerkin Least Squares Method (GLS) uses a different perturbation operator than SUPG. The perturbation operator for GLS is given by:

$$P^{GLS}(\delta h_B) = \tau \left(\frac{\delta h_B}{\Delta t} + a \frac{\partial \delta h_B}{\partial x} + \sigma \delta h_B \right) \tag{4.51}$$

where τ is given by (4.39). The residual is the same as for SUPG and is given by (4.41). The matrices for the GLS discretization are given by:

$$\begin{aligned} \mathbf{K}_{GLS}^{e,stab} = & \int_{\Omega^e} \mathbf{N^e}^\mathsf{T} \frac{\tau}{\Delta t} a \mathbf{B^e} d\Omega^e + \int_{\Omega^e} \mathbf{N^e}^\mathsf{T} \frac{\tau}{\Delta t} \sigma \mathbf{N^e} d\Omega^e + \int_{\Omega^e} \mathbf{B^e}^\mathsf{T} \tau a^2 \mathbf{B^e} d\Omega^e \\ & + \int_{\Omega^e} \mathbf{B^e}^\mathsf{T} \tau a \sigma \mathbf{N^e} d\Omega^e + \int_{\Omega^e} \mathbf{N^e}^\mathsf{T} \tau \sigma a \mathbf{B^e} d\Omega^e + \int_{\Omega^e} \mathbf{N^e}^\mathsf{T} \tau \sigma^2 \mathbf{N^e} d\Omega^e \end{aligned} \tag{4.52}$$

$$\mathbf{K}_{GLS} = \mathbf{K}_G + \mathbf{K}_{GLS}^{stab} \tag{4.53}$$

$$\mathbf{C}_{GLS}^{e,stab} = \int_{\Omega^e} \mathbf{N^e}^\mathsf{T} \frac{\tau}{\Delta t} \mathbf{N^e} d\Omega^e + \int_{\Omega^e} \mathbf{B^e}^\mathsf{T} \tau a \mathbf{N^e} d\Omega^e + \int_{\Omega^e} \mathbf{N^e}^\mathsf{T} \tau \sigma \mathbf{N^e} d\Omega^e \tag{4.54}$$

$$\mathbf{C}_{GLS} = \mathbf{C}_G + \mathbf{C}_{GLS}^{stab} \tag{4.55}$$

$$\mathbf{F}_{GLS} = \mathbf{F}_G \tag{4.56}$$

The Subgrid Scales (SGS) Method

The Subgrid Scales (SGS) method is similar to GLS. The difference between SGS and GLS is the sign on the last term of the perturbation operator, as shown below:

$$P^{SGS}(\delta h_B) = \tau \left(\frac{\delta h_B}{\Delta t} + a \frac{\partial \delta h_B}{\partial x} - \sigma \delta h_B \right) \tag{4.57}$$

where τ is given by (4.39).

The residual is the same as for SUPG and GLS and is given in (4.41). The matrices for the SGS method are:

$$\begin{aligned}\mathbf{K}_{SGS}^{e,stab} = &\int_{\Omega^e} \mathbf{N}^{\mathbf{e}\mathsf{T}} \frac{\tau}{\Delta t} a \mathbf{B}^{\mathbf{e}} d\Omega^e + \int_{\Omega^e} \mathbf{N}^{\mathbf{e}\mathsf{T}} \frac{\tau}{\Delta t} \sigma \mathbf{N}^{\mathbf{e}} d\Omega^e + \int_{\Omega^e} \mathbf{B}^{\mathbf{e}\mathsf{T}} \tau a^2 \mathbf{B}^{\mathbf{e}} d\Omega^e \\ &+ \int_{\Omega^e} \mathbf{B}^{\mathbf{e}\mathsf{T}} \tau a \sigma \mathbf{N}^{\mathbf{e}} d\Omega^e - \int_{\Omega^e} \mathbf{N}^{\mathbf{e}\mathsf{T}} \tau \sigma a \mathbf{B}^{\mathbf{e}} d\Omega^e - \int_{\Omega^e} \mathbf{N}^{\mathbf{e}\mathsf{T}} \tau \sigma^2 \mathbf{N}^{\mathbf{e}} d\Omega^e\end{aligned} \tag{4.58}$$

$$\mathbf{K}_{SGS} = \mathbf{K}_G + \mathbf{K}_{SGS}^{stab} \tag{4.59}$$

$$\mathbf{C}_{SGS}^{stab} = \int_{\Omega^e} \mathbf{N}^{\mathbf{e}\mathsf{T}} \frac{\tau}{\Delta t} \mathbf{N}^{\mathbf{e}} d\Omega^e + \int_{\Omega^e} \mathbf{B}^{\mathbf{e}\mathsf{T}} \tau a \mathbf{N}^{\mathbf{e}} d\Omega^e - \int_{\Omega^e} \mathbf{N}^{\mathbf{e}\mathsf{T}} \tau \sigma \mathbf{N}^{\mathbf{e}} d\Omega^e \tag{4.60}$$

$$\mathbf{C}_{SGS} = \mathbf{C}_G + \mathbf{C}_{SGS}^{stab} \tag{4.61}$$

$$\mathbf{F}_{SGS} = \mathbf{F}_G \tag{4.62}$$

The Least Squares Finite Element Method (LSFEM)

There are two main differences between the Least Squares Finite Element Method (LSFEM) and the three other consistent stabilization methods (SUPG, GLS and SGS). The first difference is the general form of the perturbation operator. The second difference is that the definition of the stabilization parameter τ arises directly from the derivation, and thus one does not need to define τ separately, as in (4.39).

$$P^{LSFEM}(\delta h_B) = \tau^{LSFEM} \left(a \frac{\partial \delta h_B}{\partial x} + \sigma \delta h_B \right) \tag{4.63}$$

where τ^{LSFEM} is given by the following equation:

$$\tau^{LSFEM} = \theta \Delta t \tag{4.64}$$

LSFEM shares the same residual as SUPG, GLS, and SGS. The residual is given by (4.41). The matrices for the LSFEM discretization are given by:

$$\begin{aligned}\mathbf{K}_{LSFEM}^{e,stab} = &\int_{\Omega^e} \mathbf{B^e}^\mathsf{T} \theta \Delta t a^2 \mathbf{B^e} d\Omega^e + \int_{\Omega^e} \mathbf{N^e}^\mathsf{T} \theta \Delta t \sigma^2 \mathbf{N^e} d\Omega^e \\ &+ \int_{\Omega^e} \mathbf{N^e}^\mathsf{T} \theta \Delta t \sigma a \mathbf{B^e} d\Omega^e + \int_{\Omega^e} \mathbf{B^e}^\mathsf{T} \theta \Delta t a \sigma \mathbf{N^e} d\Omega^e\end{aligned} \tag{4.65}$$

$$\mathbf{K}_{LSFEM} = \mathbf{K}_G + \mathbf{K}_{LSFEM}^{stab} \tag{4.66}$$

$$\mathbf{C}_{LSFEM}^{e,stab} = \int_{\Omega^e} \mathbf{B^e}^\mathsf{T} \theta \Delta t a \mathbf{N^e} d\Omega^e + \int_{\Omega^e} \mathbf{N^e}^\mathsf{T} \theta \Delta t \sigma \mathbf{N^e} d\Omega^e \tag{4.67}$$

$$\mathbf{C}_{LSFEM} = \mathbf{C}_G + \mathbf{C}_{LSFEM}^{stab} \tag{4.68}$$

$$\mathbf{F}_{LSFEM} = \mathbf{F}_G \tag{4.69}$$

4.5 Solution Procedure

4.5.1 Single Step (SS) Approach

One of the solution strategies that is used to solve the coupled problem is illustrated in Figure 4.2. It is similar to that found in [68]. The simulation begins at $t = 0$. The initial conditions for the saturation equation (4.21) are specified and used to calculate the initial pressure distribution. Next, the injection begins. For each time the pressure distribution is calculated and used to determine the average brine and CO_2 distributions. This loop is executed until the end time is reached.

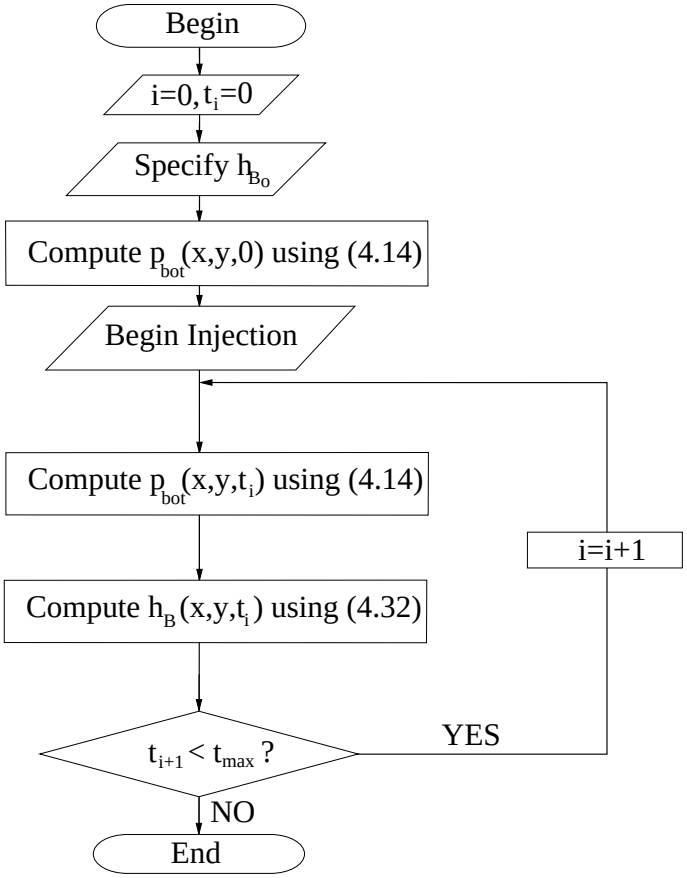

Figure 4.2: Sequential solution strategy to solve (4.14) and (4.32) [5].

4.5.2 Predictor-Corrector (PC) Approach

A second solution technique is examined and compared to the methodology described in the previous subsection. In this approach a Heun predictor-corrector (PC) [35] is used to improve the solution of the saturation equation.

The predictor step is:

$$\{\mathbf{p_{bot}}\}^{n+\frac{1}{2}} = [\mathbf{K_p}^n]^{-1}\{\mathbf{F_p}\}^n \tag{4.70}$$

$$\{\mathbf{h_B}\}^{n+\frac{1}{2}} = \{\mathbf{h_B}\}^n - [\mathbf{K_{eff}}^{n+\frac{1}{2}}]^{-1}\{\mathbf{F_{eff}^{incr}}\}^{n+\frac{1}{2}} \tag{4.71}$$

in which $\{\mathbf{p_{bot}}\}^{n+\frac{1}{2}}$ is the predicted pressure vector, $[\mathbf{K_p}^n]$ is the pressure diffusion matrix

using the nodal saturation from time n, $\{\mathbf{F_p}\}^n$ is the pressure flux vector computed using the nodal saturation from time n, $\{\mathbf{h_B}\}^{n+\frac{1}{2}}$ is the predicted saturation vector, $\{\mathbf{h_B}\}^n$ is the saturation vector from time t_n, $[\mathbf{K_{eff}}^{n+\frac{1}{2}}]$ is the saturation effective advection matrix computed using the predicted nodal pressures, and $\{\mathbf{F_{eff}^{incr}}\}^{n+\frac{1}{2}} = [\mathbf{K}_\alpha]^{n+\frac{1}{2}}\{\mathbf{h_B}\}^n$ is the saturation effective incremental flux vector computed using the predicted nodal pressures, $[\mathbf{K}_\alpha]^{n+\frac{1}{2}}$ is the advection matrix from (5.25) (α = Galerkin, SU, SUPG or LSFEM) evaluated using the predicted nodal pressures.

The corrector step is:

$$\{\mathbf{p_{bot}}\}^{n+1} = [\mathbf{K_p}^{n+\frac{1}{2}}]^{-1}\{\mathbf{F_p}\}^{n+\frac{1}{2}} \tag{4.72}$$

$$\{\mathbf{h_B}\}^{n+1} = \{\mathbf{h_B}\}^n - \frac{\Delta t}{2}\left([\mathbf{K_{eff}}^{n+\frac{1}{2}}]^{-1}\{\mathbf{F_{eff}^{incr}}\}^{n+\frac{1}{2}} + [\mathbf{K_{eff}}^{n+1}]^{-1}\{\mathbf{F_{eff}^{incr}}\}^{n+1}\right) \tag{4.73}$$

where $\{\mathbf{p_{bot}}\}^{n+1}$ is the corrected pressure vector at time t_{n+1}, $[\mathbf{K_p}^{n+\frac{1}{2}}]$ is the pressure diffusion matrix computed using the predicted nodal saturations, $\{\mathbf{F_p}\}^{n+\frac{1}{2}}$ is the pressure flux vector computed using the predicted nodal saturation, $\{\mathbf{h_B}\}^{n+1}$ is the corrected saturation vector, $[\mathbf{K_{eff}}^{n+1}]$ is the saturation effective advection matrix computed using the corrected nodal pressures from time t_{n+1}, $\{\mathbf{F_{eff}^{incr}}\}^{n+1} = [\mathbf{K}_\alpha]^{n+1}\{\mathbf{h_B}\}^{n+\frac{1}{2}}$ is the saturation effective incremental flux vector computed using the corrected nodal pressures from time t_{n+1}, and $[\mathbf{K}_\alpha]^{n+1}$ is the advection matrix evaluated using the corrected nodal pressures.

4.6 Stabilization Using One Dimensional Linear Elements

In this section three examples are considered. First, a manufactured solution is used to measure the convergence of the saturation distribution error in the L_2 norm. In the final two examples, two quasi-two dimensional test problems are considered to compare the Galerkin discretization of the saturation equation with three stabilized discretizations: SU, SUPG, and LSFEM. In the second example, CO_2 is injected into a horizontal aquifer via a single well. In the third example, two injection wells pumping CO_2 into a sloping aquifer is considered. The performance of each discretization method is investigated and compared. The relative strengths and weaknesses of each method in solving these problems are discussed.

4.6.1 Example 1 - Convergence Study of a Manufactured Solution

In this section the convergence of the L_2 error of the saturation distribution is studied by considering a manufactured solution in one dimension. A horizontal aquifer is assumed and simplified system properties are used as shown in Table 4.1.

Table 4.1: System properties for example 1 [6].

Property	Value	Units
μ_B	1	Ns/m^2
μ_C	1	Ns/m^2
ρ_B	1	kg/m^3
ρ_C	1	kg/m^3
S_B	0	-
ϕ	1	-
k_x	1	m^2
k_C^{rel}	1	-

After substituting the simplified system properties and using the fact that the aquifer

is horizontal, the following simplified forms of the pressure and saturation equations are obtained:

$$\frac{\partial}{\partial x}\left(h_C\frac{\partial p_{bot}}{\partial x}\right)+\frac{\partial}{\partial x}\left(h_B\frac{\partial p_{bot}}{\partial x}\right)=s(x,t),\quad x\in[0,1] \tag{4.74}$$

and

$$p_{bot}(x,t)=1 \text{ on } \Gamma_p \tag{4.75}$$

$$\frac{\partial h_B}{\partial t}=\frac{\partial}{\partial x}\left(h_B\frac{\partial p_{bot}}{\partial x}\right),\ x\in[0,1],\ \mathrm{t}\ \in[0,0.25] \tag{4.76}$$

$$\begin{aligned} h_B(x,t)&=1 \text{ on } \Gamma_h \\ h_B(x,0)&=1-\frac{1}{2}\sin(\pi x) \text{ on } \Omega \end{aligned} \tag{4.77}$$

The manufactured solution is obtained by assuming the solution to the CO_2 and brine depths. The solution to the CO_2 is assumed to be:

$$h_C(x,t)=\frac{1}{2}\sin(\pi x)\cos(\pi t) \tag{4.78}$$

and it follows that the brine distribution is:

$$h_B(x,t)=1-\frac{1}{2}\sin(\pi x)\cos(\pi t) \tag{4.79}$$

The saturation equation (4.76) with (4.79) is used to solve for the pressure distribution. The pressure distribution is then used to solve for a source term from the pressure equation

(4.74). The source term in (4.74) is found to be:

$$s(x,t) = \frac{\pi \sin(\pi t)\left(\cos(\pi t) - 4\cos\left(\frac{\pi x}{2}\right)\sin\left(\frac{\pi x}{2}\right)\right)}{4\cos^2(\pi t)\cos^2\left(\frac{\pi x}{2}\right) - 4\cos^2(\pi t)\cos^4\left(\frac{\pi x}{2}\right) - 8\sin\left(\frac{\pi x}{2}\right)\cos(\pi t)\cos\left(\frac{\pi x}{2}\right) + 4} \tag{4.80}$$

Figure 4.3 shows the convergence of the L_2 error of the saturation profile at time $t = 0.25\ s$ using the single step (SS) approach. The error in the L_2 norm in the saturation approximation is given by:

$$\epsilon_h^m = \left(\frac{\int_\Omega (h_B^m - h_B^{ex})^2 d\Omega}{\int_\Omega (h_B^{ex})^2 d\Omega}\right)^{\frac{1}{2}} \tag{4.81}$$

where m is the number of degrees of freedom in the approximation and a superscript ex denotes the exact solution.

The slope of the four leftmost data points are displayed on Figure 4.3. All methods except SUPG-8τ and SUPG-10τ give identical rates of convergence of ϵ_h^m of 1.00. The convergence rate is slightly lower for the SUPG-8τ and SUPG-10τ, at rates of 0.999 and 0.998 respectively. SUPG-10τ and SUPG-8τ also have the largest errors for each element size.

The saturation convergence for the predictor-corrector (PC) approach is shown in Figure 4.4. The results are essentially the same as for the SS approach in Figure 4.3. The results of this example demonstrate that the solution methodology presented in this chapter achieves first order convergence of saturation distribution error in the L_2 norm.

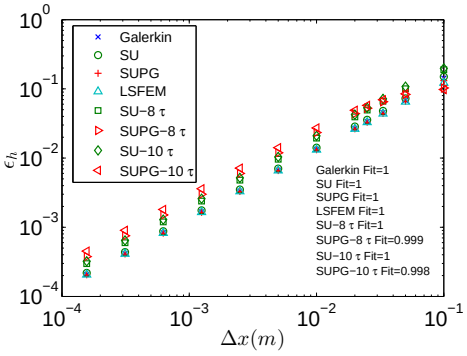

Figure 4.3: L_2 error vs. element size after $t = 0.25\ s$, $\theta = 1$, $Cr_{max} = 1$, SS method [6].

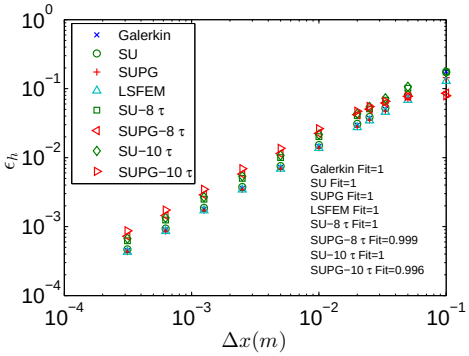

Figure 4.4: L_2 error vs. element size after $t = 0.25\ s$, $\theta = 1$, $Cr_{max} = 1$, PC method [6].

4.6.2 Example 2 - Point Source Injection into a Horizontal Aquifer

In this example, CO_2 is injected into the centre of a hypothetical 1000 m × 1 m aquifer at a depth of 2970 m, as shown in Figure 4.5. The system properties are given in Table 4.2. The aquifer has a uniform thickness of 30 m. CO_2 is injected into the aquifer at a rate of 13.33 m^3/day. The injection well is modelled as a point source injection at a node to improve the accuracy of the pressure approximation. The system is symmetric, so symmetric boundary conditions and half the domain is used. At $x = 0$ the injection is applied as a boundary flux for the pressure equation and a no-flow boundary is imposed for the saturation equation. At $x = 500m$ Dirichlet boundaries are imposed for the pressure and saturation equation.

The results in this example focus on two times. The first time is when the CO_2 plume is far from the domain boundary. The second time of interest is after the CO_2 reaches the edge of the domain. Gravity causes the CO_2 to rise to the top of the aquifer above the brine. This can lead to the creation of a very thin CO_2 boundary layer along the upper caprock that extends far beyond the centroid of the plume. Thus in the practical modelling of carbon sequestration the case of CO_2 reaching the edge of the domain may

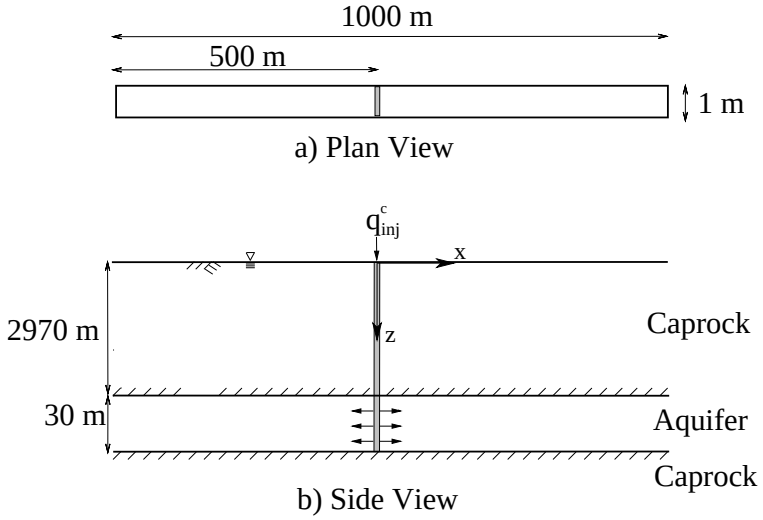

Figure 4.5: Example 1: Injection into a single aquifer system [6].

Table 4.2: System properties for example 2 [6].

Property	Value	Units
μ_B	2.535e-4	Ns/m^2
μ_C	3.950e-5	Ns/m^2
ρ_B	1045	kg/m^3
ρ_C	479	kg/m^3
S_B	0	-
ϕ	0.15	-
k_x	2e-14	m^2
k_C^{rel}	1	-
q_{inj}	13.33	m^3/day

be encountered.

A large number of simulations (432) were executed using various parameters (including θ, $Cr_{max}(\Delta t)$, and τ), the sequential solution strategy (SS vs. PC), and the stabilization schemes. The results of these simulations are summarized in Tables 4.3-4.8.

Forward Euler (FE) FDM in Time ($\theta = 0$)

The results using Forward Euler (FE) FDM are summarized in Table 4.3 for the SS scheme and Table 4.4 for the PC scheme. For both SS and PC all methods smooth solutions were obtained when $Cr_{max} \leq 0.005$. When $\theta = 0$ all methods reduce to the

Galerkin FEM based on (4.39) and (4.64). Figure 4.6 shows the saturation distribution for $\theta = 0, Cr_{max} = 0.001$ and the SS sequential scheme. The horizontal line represents the top aquifer boundary. Figure 4.7 shows the associated pressure distributions. All of the FEM variants give nearly identical solutions as expected.

Table 4.3: Simulation results after 50 *days* of CO_2 injection for $\theta = 0$ and the SS method. "S" indicates a smooth solution (stable and non-oscillatory) and "O" indicates either noticeable oscillations or an unstable solution. Using 100 linear elements [6].

$\theta = 0$				τ		8τ		10τ	
Δt $(days)$	Cr_{max}	**G**	**LS**	**SUPG**	**SU**	**SUPG**	**SU**	**SUPG**	**SU**
0.0034	**0.001**	S	S	S	S	S	S	S	S
0.0169	**0.005**	S	S	S	S	S	S	S	S
0.0337	**0.01**	O	O	O	O	O	O	O	O
0.1684	**0.05**	O	O	O	O	O	O	O	O
0.3356	**0.1**	O	O	O	O	O	O	O	O
1.6667	**0.5**	O	O	O	O	O	O	O	O
3.3333	**1**	O	O	O	O	O	O	O	O
10	**3**	O	O	O	O	O	O	O	O
16.6667	**5**	O	O	O	O	O	O	O	O

Table 4.4: Simulation results after 50 *days* of CO_2 injection for $\theta = 0$ and the PC method. "S" indicates a smooth solution (stable and non-oscillatory) and "O" indicates either noticeable oscillations or an unstable solution. Using 100 linear elements [6].

$\theta = 0$				τ		8τ		10τ	
Δt $(days)$	Cr_{max}	**G**	**LS**	**SUPG**	**SU**	**SUPG**	**SU**	**SUPG**	**SU**
0.0034	**0.001**	S	S	S	S	S	S	S	S
0.0169	**0.005**	S	S	S	S	S	S	S	S
0.0337	**0.01**	O	O	O	O	O	O	O	O
0.1684	**0.05**	O	O	O	O	O	O	O	O
0.3356	**0.1**	O	O	O	O	O	O	O	O
1.6667	**0.5**	O	O	O	O	O	O	O	O
3.3333	**1**	O	O	O	O	O	O	O	O
10	**3**	O	O	O	O	O	O	O	O
16.6667	**5**	O	O	O	O	O	O	O	O

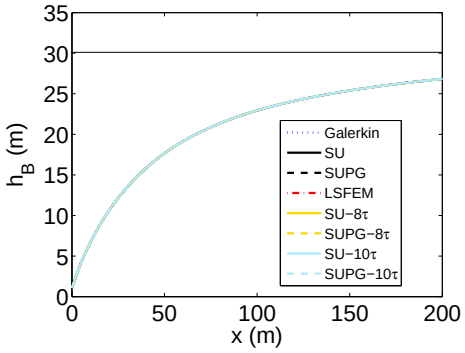

Figure 4.6: Saturation distribution after 50 *days* of CO_2 injection, $\theta = 0$, $Cr_{max} = 0.001$, using 100 linear elements, SS method [6].

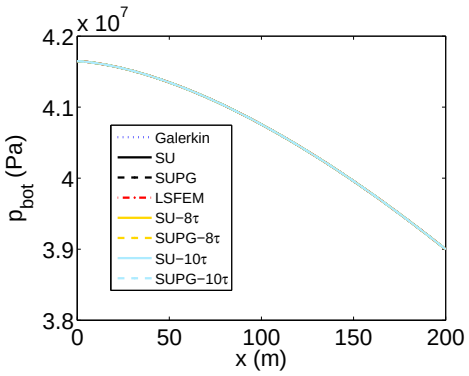

Figure 4.7: Pressure distribution after 50 *days* of CO_2 injection, $\theta = 0$, $Cr_{max} = 0.001$, using 100 linear elements, SS method [6].

Crank-Nicolson (CN) FDM in Time ($\theta = 0.5$)

The Crank-Nicolson (CN) FDM results are summarized in Table 4.5 for the SS scheme and Table 4.6 for the PC scheme. For both sequential solution schemes (SS and PC) Galerkin, LSFEM, SUPG-τ, and SU-τ were found to give smooth solutions when $Cr_{max} \leq 0.005$, while SUPG-8τ and SUPG-10τ produced smooth solutions only when $Cr_{max} = 0.001$. For the SS scheme SU-8τ achieved smooth solutions when $Cr_{max} \leq 0.005$, while SU-8τ combined with the PC scheme produced smooth solutions with $Cr_{max} \leq 0.01$, $Cr_{max} = 0.5$ and $Cr_{max} = 1$. For SU-10τ, SS produced smooth solutions for $Cr_{max} \leq 0.01$ and $Cr_{max} \geq 3$, and PC with SU-10τ gave smooth solutions with $Cr_{max} \leq 0.01$, $Cr_{max} = 0.5$ and $Cr_{max} = 1$ (same as SU-8τ).

Figure 4.8 and 4.9 show the saturation and pressure distributions for $\theta = 0.5, Cr_{max} = 0.001$ and SS solution strategy. All methods give nearly identical results.

Table 4.5: Simulation results after 50 *days* of CO_2 injection for $\theta = 0.5$ and the SS method. "S" indicates a smooth solution (stable and non-oscillatory) and "O" indicates either noticeable oscillations or an unstable solution. Using 100 linear elements [6].

$\theta = 0.5$				τ		8τ		10τ	
Δt $(days)$	Cr_{max}	**G**	**LS**	**SUPG**	**SU**	**SUPG**	**SU**	**SUPG**	**SU**
0.0034	**0.001**	S	S	S	S	S	S	S	S
0.0169	**0.005**	S	S	S	S	O	S	O	S
0.0337	**0.01**	O	O	O	O	O	O	O	S
0.1684	**0.05**	O	O	O	O	O	O	O	O
0.3356	**0.1**	O	O	O	O	O	O	O	O
1.6667	**0.5**	O	O	O	O	O	O	O	O
3.3333	**1**	O	O	O	O	O	O	O	O
10	**3**	O	O	O	O	O	O	O	S
16.6667	**5**	O	O	O	O	O	O	O	S

Table 4.6: Simulation results after 50 *days* of CO_2 injection for $\theta = 0.5$ and the PC method. "S" indicates a smooth solution (stable and non-oscillatory) and "O" indicates either noticeable oscillations or an unstable solution. Using 100 linear elements [6].

$\theta = 0.5$				τ		8τ		10τ	
Δt $(days)$	Cr_{max}	**G**	**LS**	**SUPG**	**SU**	**SUPG**	**SU**	**SUPG**	**SU**
0.0034	**0.001**	S	S	S	S	S	S	S	S
0.0169	**0.005**	S	S	S	S	O	S	O	S
0.0337	**0.01**	O	O	O	O	O	S	O	S
0.1684	**0.05**	O	O	O	O	O	O	O	O
0.3356	**0.1**	O	O	O	O	O	O	O	O
1.6667	**0.5**	O	O	O	O	O	S	O	S
3.3333	**1**	O	O	O	O	O	S	O	S
10	**3**	O	O	O	O	O	O	O	O
16.6667	**5**	O	O	O	O	O	O	O	O

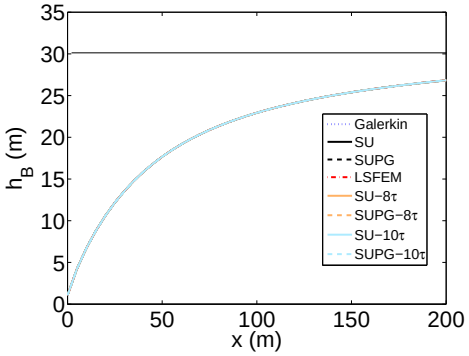

Figure 4.8: Saturation distribution after 50 *days* of CO_2 injection, $\theta = 0.5$, $Cr_{max} = 0.001$, using 100 linear elements, SS method [6].

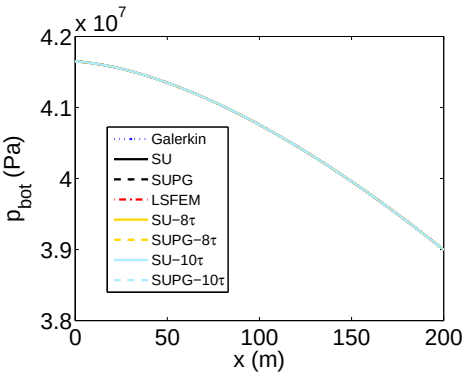

Figure 4.9: Pressure distribution after 50 *days* of CO_2 injection, $\theta = 0.5$, $Cr_{max} = 0.001$, using 100 linear elements, SS method [6].

Backward Euler (BE) FDM in Time ($\theta = 1$)

The Backward Euler (BE) FDM results are summarized in Table 4.7 for the SS scheme and Table 4.8 for the PC scheme. Non-oscillatory and stable solutions were achieved with the SS scheme for Galerkin, LSFEM, SU-τ, and SUPG-τ when $Cr_{max} \leq 0.005$ and $Cr_{max} = 5$. SUPG-8τ and SUPG-10τ gave smooth solutions only for the case of $Cr_{max} = 0.001$. SU-10τ produced smooth solutions for all values of Cr_{max} considered. Only $Cr_{max} = 0.05$ gave minor oscillations when SU-8τ was used.

When the PC scheme was used Galerkin and SU-τ produced smooth solutions when $Cr_{max} \leq 0.01$ and $Cr_{max} \geq 3$. LSFEM and SUPG-τ achieved smooth approximations when $Cr_{max} \leq 0.005$ and $Cr_{max} \geq 3$. The results produced by SUPG-8τ were smooth when $Cr_{max} = 0.001$ and $Cr_{max} \geq 1$ and by SUPG-10τ when $Cr_{max} = 0.001$ and $Cr_{max} \geq 3$. Smooth results were obtained from SU-8τ and SU-10τ for all values of Cr_{max} that were investigated.

By increasing the stabilization parameter τ by eight and ten times, SU was found to give smooth solutions for nearly all cases with $\theta = 1$ (SS and PC methods). In the one exception, the oscillations were minor. The effect of increasing τ on SUPG is quite different. Most often increasing τ increased the oscillations for SUPG.

Figure 4.10 and 4.11 show the saturation and pressure distributions for $\theta = 1, Cr_{max} = 3$ with the PC scheme. Galerkin, SU, SUPG and LSFEM give similar results. The SUPG-8τ saturation distribution shows a slight bend near $x = 0$ that is not present in the other solutions, while brine depth obtained with SUPG-10τ becomes slightly negative at the injection well (CO_2 depth exceeds the height of the aquifer). SU-8τ and SU-10τ give smooth saturation distributions that are more diffuse than the others.

Figure 4.12 shows the saturation distribution for $\theta = 1$ and $Cr_{max} = 3$ with the SS

sequential solution scheme. Only SU-8τ and SU-10τ do not contain oscillations. SUPG-10τ becomes negative 20 m from the injection well. In Figure 4.13, where $\theta = 1$ and $Cr_{max} = 1$ with the PC scheme, only SU-8τ and SU-10τ and SUPG-8τ are smooth.

Table 4.7: Simulation results after 50 *days* of CO_2 injection for $\theta = 1$ and the SS method. "S" indicates a smooth solution (stable and non-oscillatory) and "O" indicates either noticeable oscillations or an unstable solution. Using 100 linear elements [6].

$\theta = 1$				τ		8τ		10τ	
Δt $(days)$	Cr_{max}	**G**	**LS**	**SUPG**	**SU**	**SUPG**	**SU**	**SUPG**	**SU**
0.0034	**0.001**	S	S	S	S	S	S	S	S
0.0169	**0.005**	S	S	S	S	O	S	O	S
0.0337	**0.01**	O	O	O	O	O	S	O	S
0.1684	**0.05**	O	O	O	O	O	O	O	S
0.3356	**0.1**	O	O	O	O	O	S	O	S
1.6667	**0.5**	O	O	O	O	O	S	O	S
3.3333	**1**	O	O	O	O	O	S	O	S
10	**3**	O	O	O	O	O	S	O	S
16.6667	**5**	S	S	S	S	O	S	O	S

Table 4.8: Simulation results after 50 *days* of CO_2 injection for $\theta = 1$ and the PC method. "S" indicates a smooth solution (stable and non-oscillatory) and "O" indicates either noticeable oscillations or an unstable solution. Using 100 linear elements [6].

$\theta = 1$				τ		8τ		10τ	
Δt $(days)$	Cr_{max}	**G**	**LS**	**SUPG**	**SU**	**SUPG**	**SU**	**SUPG**	**SU**
0.0034	**0.001**	S	S	S	S	S	S	S	S
0.0169	**0.005**	S	S	S	S	O	S	O	S
0.0337	**0.01**	S	O	O	S	O	S	O	S
0.1684	**0.05**	O	O	O	O	O	S	O	S
0.3356	**0.1**	O	O	O	O	O	S	O	S
1.6667	**0.5**	O	O	O	O	O	S	O	S
3.3333	**1**	O	O	O	O	S	S	O	S
10	**3**	S	S	S	S	S	S	S	S
16.6667	**5**	S	S	S	S	S	S	S	S

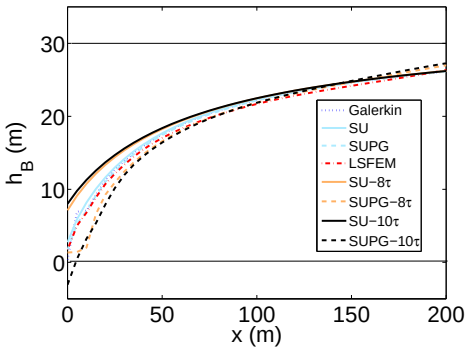

Figure 4.10: Saturation distribution after 50 *days* of CO_2 injection, $\theta = 1$, $Cr_{max} = 3$, using 100 linear elements, PC method [6].

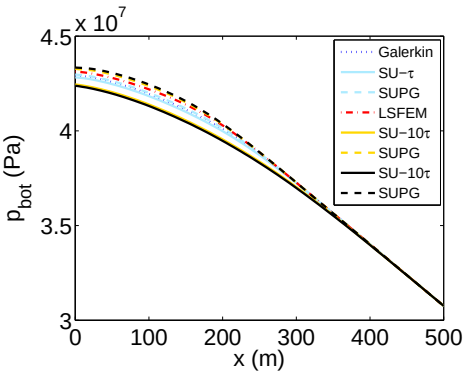

Figure 4.11: Pressure distribution after 50 *days* of CO_2 injection, $\theta = 1$, $Cr_{max} = 3$, using 100 linear elements, PC method [6].

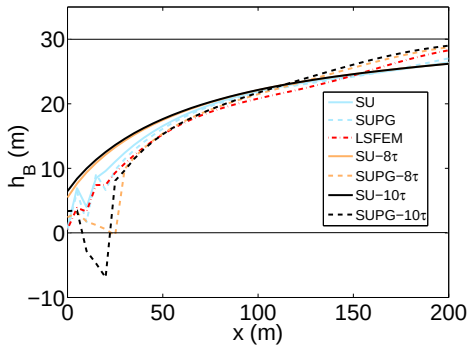

Figure 4.12: Saturation distribution after 50 *days* of CO_2 injection, $\theta = 1$, $Cr_{max} = 3$, using 100 linear elements, SS method [6].

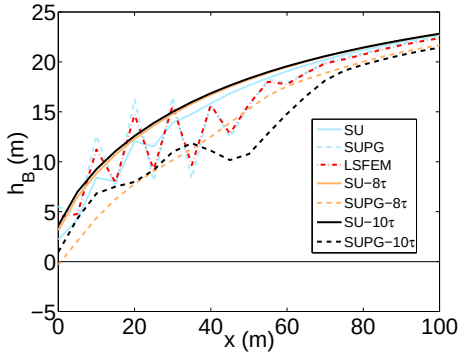

Figure 4.13: Saturation distribution after 50 *days* of CO_2 injection, $\theta = 1$, $Cr_{max} = 1$, using 100 linear elements, PC method [6].

Effects of Timestep Size

The effects of timestep size (measured by Cr_{max}) are examined in Figures 4.14 - 4.19. All methods give nearly identical solutions at small timesteps, therefore Galerkin with $Cr_{max} = 0.001$ with the SS scheme is arbitrarily selected as the reference solution for the comparisons.

Figure 4.14 shows that with large timesteps $Cr_{max} = 5$ the Galerkin FEM with the PC scheme gives a solution that is closer to the reference solution. This is also true for SUPG (Figure 4.15), LSFEM (Figure 4.16), SU (Figure 4.17) and SU-8τ (Figure 4.18).

However, SU-8τ is the least affected by the choice of the sequential solution strategy (SS or PC).

Figure 4.19 compares the SS scheme results from Figures 4.14 - 4.18. SU-8τ is the closest to the reference solution for distances greater than 200 m away from the injection well. It is important to understand the large scale migration of CO_2, so this may be an important area to have accurate simulation results.

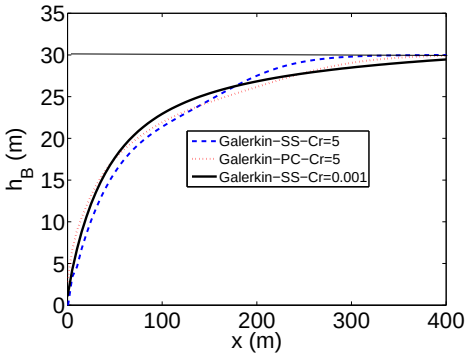

Figure 4.14: Saturation distribution after 50 *days* of CO_2 injection, $\theta = 1$ - effect of large timesteps on Galerkin approximation [6].

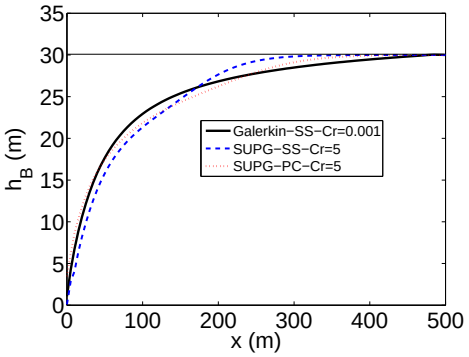

Figure 4.15: Saturation distribution after 50 *days* of CO_2 injection, $\theta = 1$ - effect of large timesteps on SUPG approximation [6].

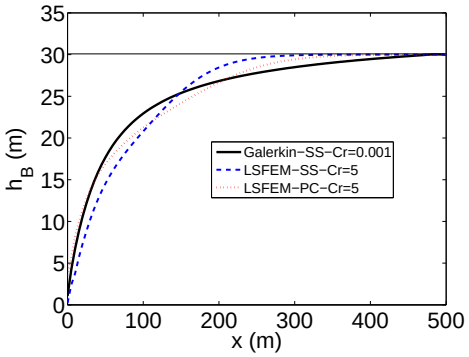

Figure 4.16: Saturation distribution after 50 *days* of CO_2 injection, $\theta = 1$ - effect of large timesteps on LSFEM approximation [6].

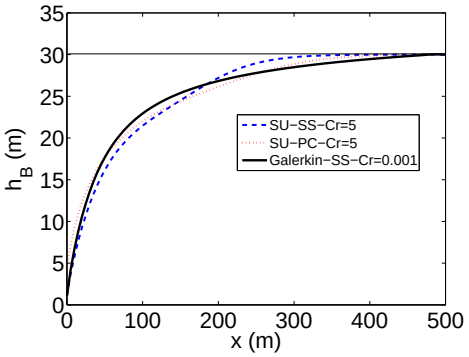

Figure 4.17: Saturation distribution after 50 *days* of CO_2 injection, $\theta = 1$ - effect of large timesteps on SU approximation [6].

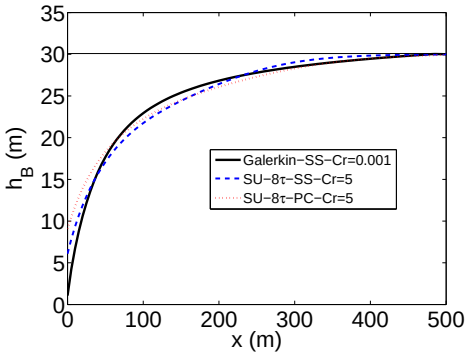

Figure 4.18: Saturation distribution after 50 *days* of CO_2 injection, $\theta = 1$ - effect of large timesteps on SU-8τ approximation [6].

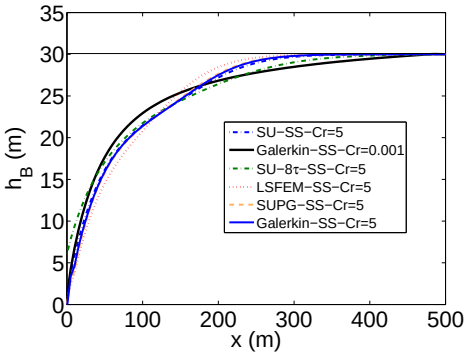

Figure 4.19: Saturation distribution after 50 *days* of CO_2 injection, $\theta = 1$ - effect of large timesteps - a comparison of approximations, SS method [6].

Injection of CO_2 into a Brine-Filled Aquifer for 350 days

When the CO_2 plume reaches the domain boundary where a Dirichlet boundary condition $h_C = 0$ ($h_B = H$) is prescribed, the boundary conditions applied to the FEM discretization do not represent the true physics of the problem. In other words, the depth of CO_2 at the domain boundary is no longer zero, as the Dirichlet boundary conditions imply. In the simulations as CO_2 leaves the system the depth of CO_2 at the boundary remains as zero, which is unrealistic. With a fine enough mesh an acceptable approximation of the saturation near the boundaries can be obtained.

The effect of the CO_2 reaching the domain boundary is shown in Figure 4.20 and Figure 4.21. Figure 4.20 compares the results of SU-8τ, SUPG-8τ, LSFEM and SU-10τ formulations (SS scheme) when the CO_2 plume reaches the domain boundary. Once the CO_2 reaches the boundary, oscillations completely contaminate the Galerkin, SU-τ, SUPG-τ, and SUPG-10τ approximations of brine (or CO_2) depth and thus are not shown. SU-8τ, SUPG-8τ, LSFEM and SU-10τ do not experience these oscillations. For SUPG-8τ, however, the brine depth becomes negative. Figure 4.21 shows the same plot for the

PC scheme where it is shown that with the PC scheme SU-τ, SU-8τ, SU-10τ, SUPG-τ and LSFEM don't oscillate or exceed the aquifer boundaries. The SUPG-8τ, SUPG-10τ solutions give CO_2 depths that exceed the aquifer height. The Galerkin approximation is not shown due to significant oscillations.

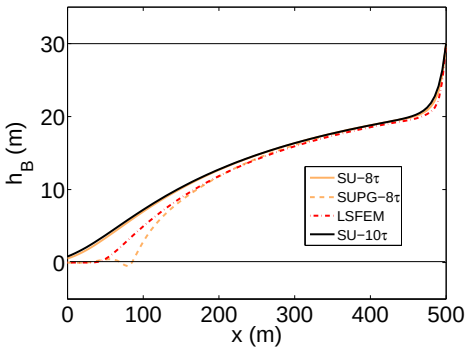

Figure 4.20: Saturation distribution after 350 *days* of CO_2 injection, $\theta = 1$, $Cr_{max} = 5$, using 100 linear elements, SS method [6].

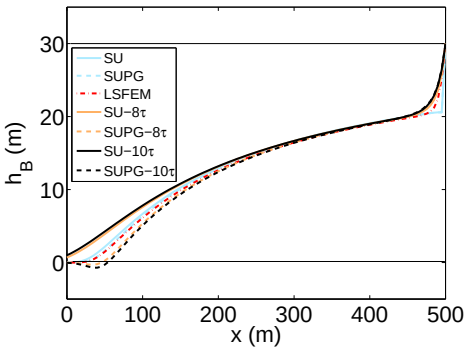

Figure 4.21: Saturation distribution after 350 *days* of CO_2 injection, $\theta = 1$, $Cr_{max} = 5$, using 100 linear elements, PC method [6].

Figure 4.20 and Figure 4.21 demonstrate that even when the Galerkin method gives smooth solutions in early times, when the domain boundary is encountered by the CO_2 significant oscillations will contaminate the solutions. Therefore stabilized methods are always necessary if the plume is expected to encounter the domain boundary.

4.6.3 Example 3 - Two Wells Injecting into a Sloping Aquifer

In this example there are two injection wells injecting CO_2 at a uniform rate of 6.67 m^3/day into a sloping aquifer. Figure 4.22 illustrates the problem. The domain is 500 m long by 1 m wide. Two-node linear elements are used. The wells are spaced 100 m apart. The system properties are the same as example 2, except that H, z_{top} and z_{bot} are functions of x. The top boundary, $z_{top}(x)$ slopes upward from left to right, while the bottom boundary $z_{bot}(x)$ slopes downward from left to right, at the same rate.

Figure 4.23 shows the average brine depth (saturation) profiles as the two plumes merge using $\theta = 1$, $Cr_{max} = 0.001$ ($\Delta t = 7.4882 \times 10^{-4}$ *days*) using the PC scheme and 200 linear elements. Solid black lines indicate the top and bottom boundaries of the aquifer. All methods give nearly identical results which are contaminated by minor oscillations at the boundaries. The results from the PC scheme and 100 elements with $Cr_{max} = 5$ ($\Delta t = 7.5$ *days*) are shown in Figure 4.24. Only SU-8τ gives a solution that is smooth and does not exceed the top and bottom aquifer boundaries. Results for the SS scheme are shown in Figure 4.25 and Figure 4.26 for $Cr_{max} = 0.001$ (200 elements) and $Cr_{max} = 5$ (100 elements) respectively. When $Cr_{max} = 0.001$ all methods give minor oscillations in the solution at the boundaries. When large timesteps are used ($Cr_{max} = 5$) only SU-8τ gives a smooth solution that remains within the aquifer boundary.

Figure 4.27 compares SU-8τ with the SS and PC sequential solution schemes. The results are very similar. The associated pressure distributions are also very similar as shown in Figure 4.28.

This example demonstrates that the SU-8τ (and SU-10τ) stabilization is the only method to give satisfactory results using large timesteps when multiple injection wells result in plumes merging. The results for SU-10τ were not shown in this example, but are essentially the same as SU-8τ, but are slightly more diffuse. Since the PC scheme is much more computationally expensive, the SU-8τ stabilization combined with the SS sequential solution strategy is the preferable approach for this problem.

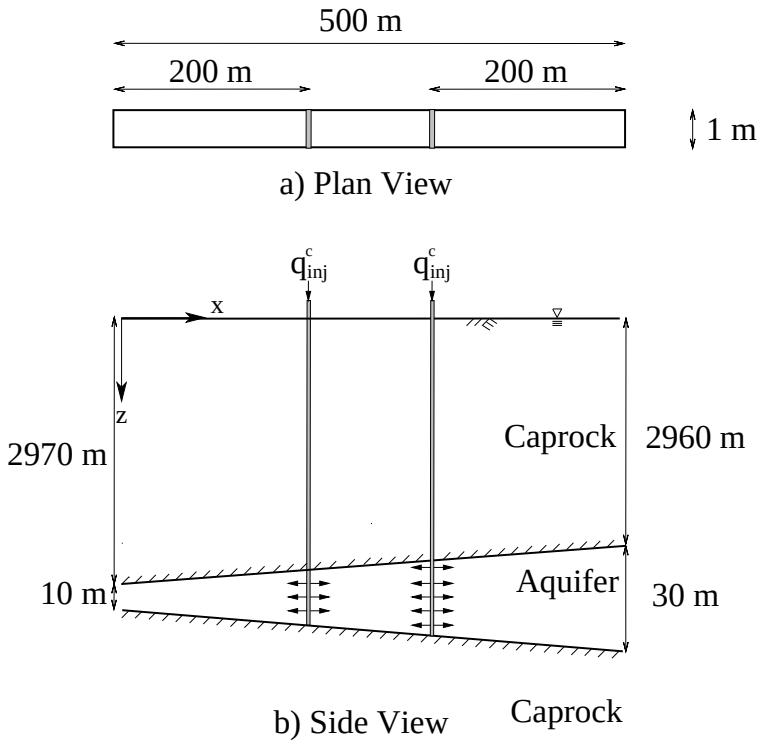

Figure 4.22: Two wells injecting into a single nonhorizontal variable depth aquifer [6].

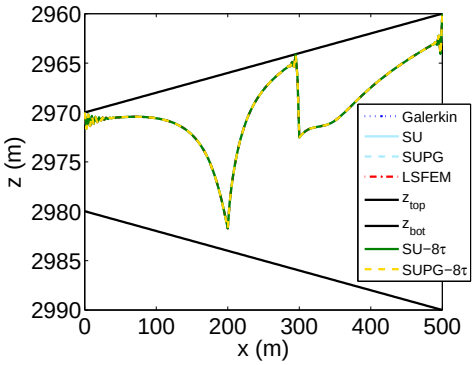

Figure 4.23: Saturation distribution after 30 *days* of CO_2 injection from two wells, $\theta = 1$, $Cr_{max} = 0.001$, using 200 linear elements, PC method [6].

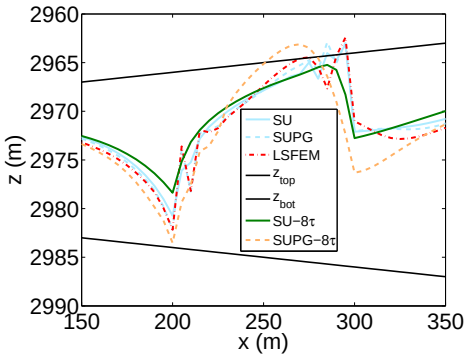

Figure 4.24: Saturation distribution after 30 *days* of CO_2 injection from two wells, $\theta = 1$, $Cr_{max} = 5$, using 100 linear elements, PC method [6].

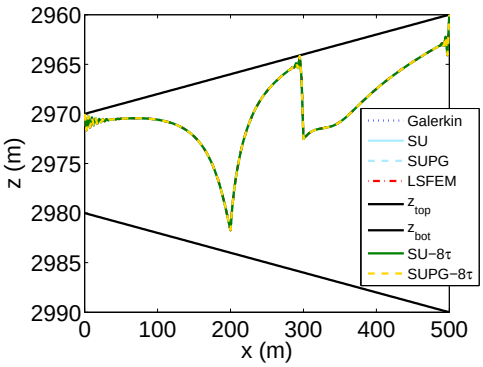

Figure 4.25: Saturation distribution after 30 *days* of CO_2 injection from two wells, $\theta = 1$, $Cr_{max} = 0.001$, using 200 linear elements, SS method [6].

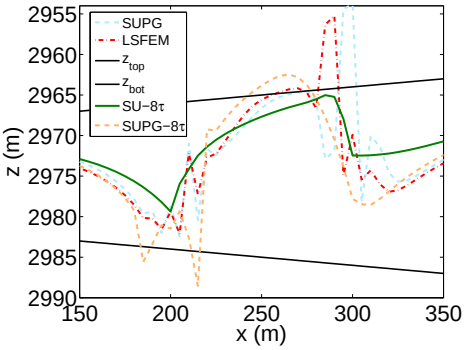

Figure 4.26: Saturation distribution after 30 *days* of CO_2 injection from two wells, $\theta = 1$, $Cr_{max} = 5$, using 100 linear elements, SS method [6].

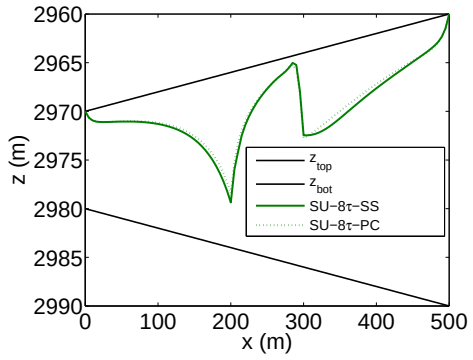

Figure 4.27: Saturation distribution after 30 *days* of CO_2 injection from two wells, $\theta = 1$, $Cr_{max} = 5$, using 100 linear elements, a comparison of SS and PC methods [6].

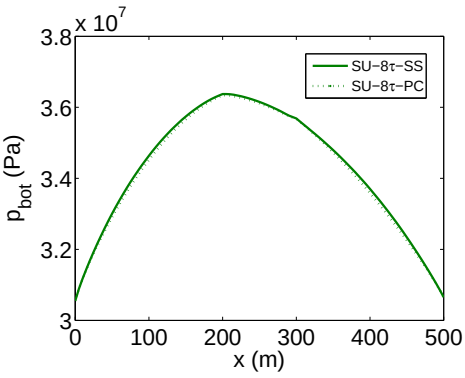

Figure 4.28: Pressure distribution after 30 *days* of CO_2 injection from two wells, $\theta = 1$, $Cr_{max} = 5$, using 100 linear elements, a comparison of SS and PC methods [6].

4.7 Stabilization Using One Dimensional Quadratic Elements

Quadratic elements are required for complete representations of the SUPG and LSFEM stabilizations. In addition, SGS and GLS stabilizations require quadratic elements in order to give formulations that are different from SUPG. In this section two examples are used to demonstrate and compare the various stabilized discretizations of the saturation equation using quadratic elements.

4.7.1 Example 1 - Injection of CO_2 into Brine-Filled Aquifer: Comparison of Stabilized FEMs

In this problem an injection well pumps CO_2 into an aquifer at a rate of 13.33 m^3/day. The aquifer is located at a depth of 2970 m and has a uniform height of 30 m. This scenario is shown in Figure 4.29. The system properties are given in Table 4.9. The domain is 1000 m in length, and has a unit width. The system is symmetric, as such only half the domain is modelled after applying the proper symmetric boundary conditions.

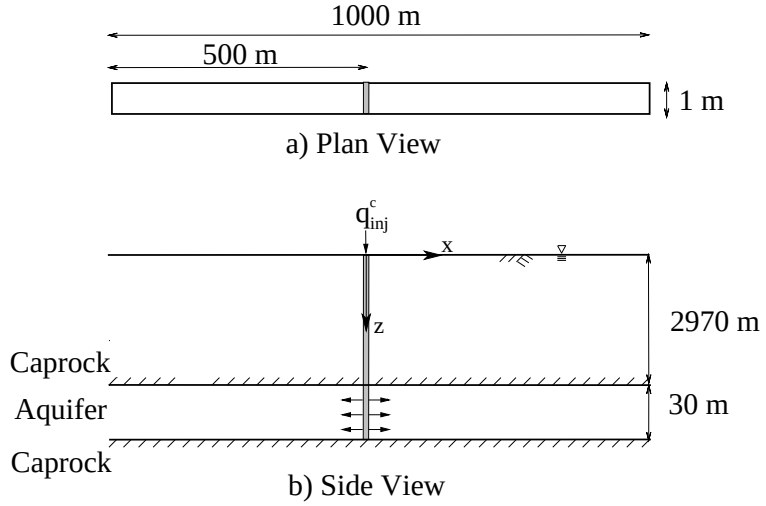

Figure 4.29: Example 1: One injection well injecting CO_2 into a single aquifer [4].

Injection over 50 *days* was simulated using seven different formulations: Galerkin,

Table 4.9: System properties for example 1 [4].

Property	Value	Units
μ_B	2.535e-4	Ns/m^2
μ_C	3.950e-5	Ns/m^2
ρ_B	1045	kg/m^3
ρ_C	479	kg/m^3
S_B	0	-
ϕ	0.15	-
k	2e-14	m^2
k_C^{rel}	1	-
q_{inj}	13.33	m^3/day

SU, SU-8τ (τ increased by a factor of 8), SUPG, LSFEM, GLS and SGS using Backward Euler ($\theta = 1$) time integration. The simulations are run using a range of timestep sizes and the results are summarized in Table 4.10. Each simulation is marked with one of four symbols: "S" means a stable and non-oscillatory (smooth) solution, "S*" means that minor oscillations are present, "S**" means that significant oscillations are present and "O" means that the result either contains extreme oscillations or is unstable.

Galerkin produces oscillation-free results only when $Cr = 5$. SU, SUPG and LSFEM result in smooth solutions when $Cr \geq 3$. SU-8τ smooth results when $Cr \geq 0.05$. GLS and SGS produce stable non-oscillatory solutions when $Cr \leq 0.05$ or $Cr \geq 3$. These results can be compared to those presented in the previous section to compare linear and quadratic elements. The stability ranges were similar for quadratic elements and linear elements for Galerkin, SU, SU-8τ, SUPG, and LSFEM. The additional methods examined in this section (GLS and SGS), which are only made possible by quadratic and higher order elements, give superior stability ranges to the other consistently stabilized methods (SUPG and LSFEM). The stability ranges of GLS and SGS are similar to that of SU-8τ which was shown earlier in this chapter to be the most robust stabilized method for linear elements.

Figure 4.30 shows the average brine saturation when $Cr = 0.0001$ ($\Delta t = 0.00067$ *days*). All of the stabilization methods give similar results. Only GLS and SGS are free from the minor oscillations that occur near the right boundary which exceed the top aquifer boundary. This can be seen more clearly in Figure 4.31. The associated pressure distributions are shown in Figure 4.32.

Figure 4.33 shows the brine saturation distributions with $Cr = 0.005$ ($\Delta t = 0.0034$ *days*). GLS and SGS give smooth solutions, while SU-8τ gives oscillations near the right boundary. The other methods give extreme oscillations and are not shown.

Figure 4.34 compares the various stabilization methods when $Cr = 3$ ($\Delta t = 16.66667$ *days*). In this case all methods give smooth solutions except Galerkin which shows significant oscillations near the injection site. SU-8τ gives a more diffuse solution than the other methods.

Figure 4.35 plots the average brine saturation when $Cr = 5$ ($\Delta t = 25$ *days*). In this case all stabilization methods give smooth solutions. Again, SU-8τ exhibits a more diffusive solution compared to the others.

Figures 4.36 - 4.39 compare linear and quadratic elements for small timesteps and large timesteps. In Figures 4.36 and 4.37 linear and quadratic elements are compared for $Cr = 0.001$. All methods (linear and quadratic) give nearly identical saturation distributions except near the right boundary. SGS and GLS are the only methods that do not exceed the top aquifer boundary. Although slight, the other methods exceed the top boundary and exhibit oscillations. Linear elements gave results that exceed the top aquifer boundary by a lesser amount than the quadratic elements. Figures 4.38 and 4.39 compare linear and quadratic elements using $Cr = 5$. Galerkin, LSFEM, and SU-8τ give very similar saturation distributions whether or not linear or quadratic elements are

used. SU gives significant oscillations when linear elements are used (not shown), but no oscillations appear when quadratic elements are used. When linear elements are used with SUPG an oscillation occurs near the injection well where the CO_2 saturation exceeds the height of the aquifer. This does not occur when SUPG is combined with quadratic elements. In addition, SUPG with linear elements give a less diffuse solution compared with quadratic elements. Similarly, LSFEM with linear elements also gives a less diffuse solution compared with quadratic elements.

When linear elements are used, the SUPG and LSFEM residual are incomplete because of the second derivatives in the reaction term. In addition, the LSFEM perturbation function is also incomplete with linear elements. This explains the differences between linear and quadratic elements for LSFEM and SUPG. When quadratic elements are used all methods give nearly identical distributions except SU-8τ which gives a more diffuse solution that better matches the solutions with small timesteps as the distance from the injection well increases.

Figure 4.40 shows the average brine saturation after 350 *days* of injection. After 350 *days* much of the CO_2 that was injected has left the system. For the CO_2 to leave the system the depth of the CO_2 should be non-zero to be physically realistic. However, Dirichlet boundary conditions are typically imposed for this type of problem. Dirichlet boundary conditions are applied at the domain boundary that represents a brine only condition at the boundary. This results in an inconsistency between the numerical model and the physical reality. When the CO_2 plume encounters these Dirichlet boundary conditions numerical oscillations can occur as shown in Figure 4.40. Only SU-8τ gives a smooth solution. SUPG, LSFEM and GLS all exhibit significant oscillations. Galerkin, SU and SGS are not shown as they exhibit extreme oscillations. When linear elements

were used, smooth solutions were obtained for SU-8τ and LSFEM (SUPG had minor oscillations). However, with quadratic elements only SU-8τ gives a smooth solution. This example suggests that quadratic elements encounter greater oscillations as the CO_2 plume exits the domain.

Table 4.10: Simulation results after 50 *days* of CO_2 injection for $\theta = 1$. "S" indicates a smooth solution (stable and non-oscillatory) "S*" indicates minor oscillations, "S**" indicates significant oscillations and "O" indicates either extreme oscillations or an unstable solution. Using 50 quadratic elements [4].

Δt $(days)$	Cr_{max}	**G**	**SU**	**SU-8τ**	**SUPG**	**LS**	**GLS**	**SGS**
0.00067	**0.0001**	S*	S*	S*	S*	S*	S	S
0.0034	**0.0005**	S*	S*	S*	S*	S*	S	S
0.0067	**0.001**	S*	S*	S*	S*	S*	S	S
0.0337	**0.005**	O	O	S**	O	O	S	S
0.0675	**0.01**	O	O	O	O	O	S	S
0.3356	**0.05**	O	O	S	O	O	S	S
0.6667	**0.1**	O	O	S	O	O	O	O
3.3333	**0.5**	O	O	S	O	O	S**	O
6.25	**1**	O	O	S	O	O	S**	S**
16.6667	**3**	S**	S	S	S	S	S	S
25	**5**	S	S	S	S	S	S	S

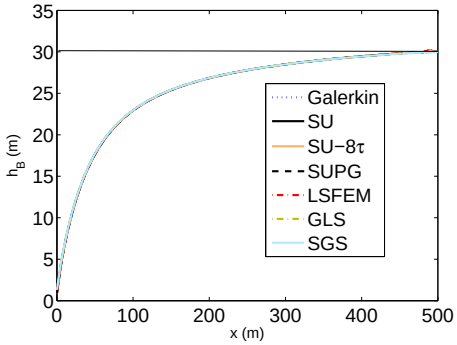

Figure 4.30: Saturation distribution after 50 *days* of CO_2 injection, $Cr_{max} = 0.0001$, using 50 quadratic elements [4].

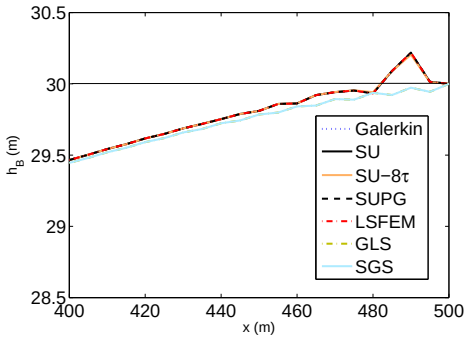

Figure 4.31: Saturation distribution after 50 *days* of CO_2 injection, $Cr_{max} = 0.0001$, using 50 quadratic elements. Close-up of oscillations near boundary [4].

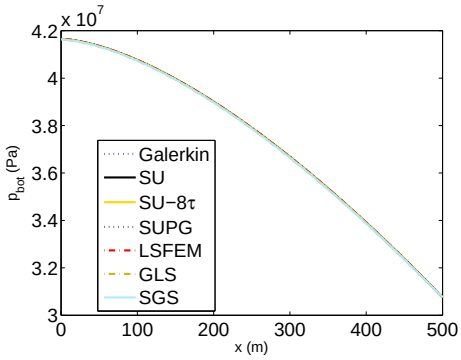

Figure 4.32: Pressure distribution after 50 *days* of CO_2 injection, $Cr_{max} = 0.0001$, using 50 quadratic elements [4].

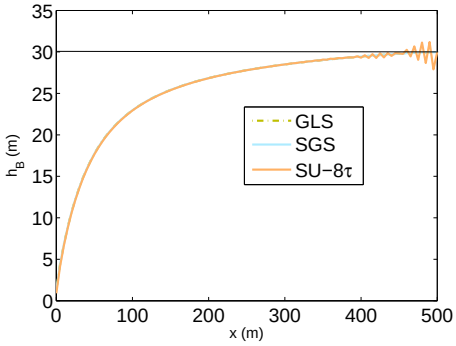

Figure 4.33: Saturation distribution after 50 *days* of CO_2 injection, $Cr_{max} = 0.005$, using 50 quadratic elements [4].

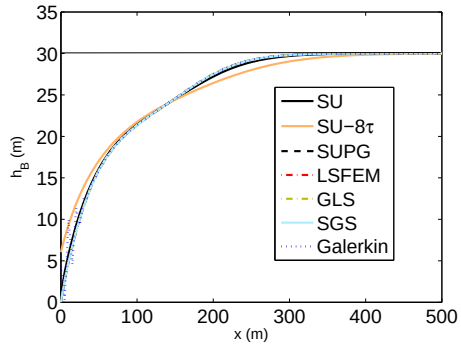

Figure 4.34: Saturation distribution after 50 *days* of CO_2 injection, $Cr_{max} = 3$, using 50 quadratic elements [4].

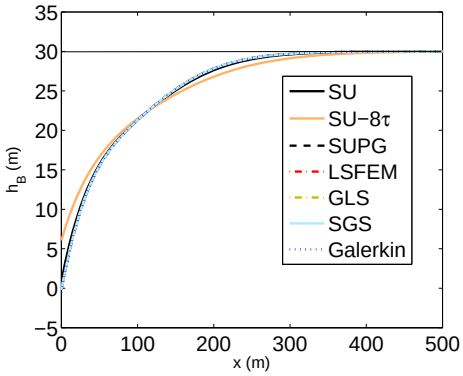

Figure 4.35: Saturation distribution after 50 *days* of CO_2 injection, $Cr_{max} = 5$, using 50 quadratic elements [4].

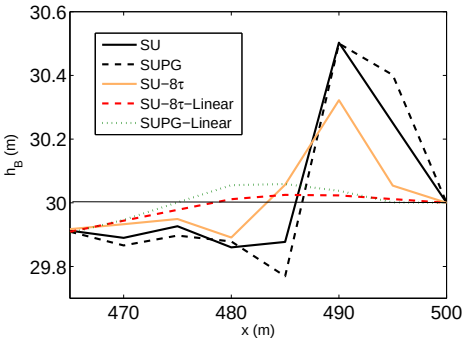

Figure 4.36: Close-up of Saturation distribution after 50 *days* of CO_2 injection, $Cr_{max} = 0.001$, 100 linear elements vs. 50 quadratic elements [4].

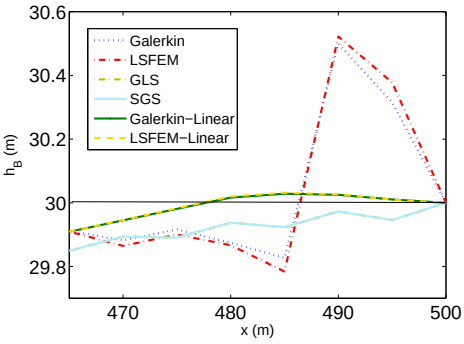

Figure 4.37: Close-up of Saturation distribution after 50 *days* of CO_2 injection, $Cr_{max} = 0.001$, 100 linear elements vs. 50 quadratic elements [4].

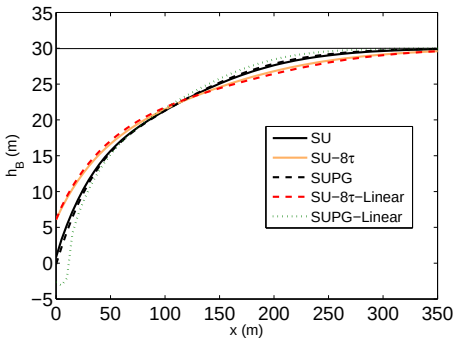

Figure 4.38: Saturation distribution after 50 *days* of CO_2 injection, $Cr_{max} = 5$, 100 linear elements vs. 50 quadratic elements [4].

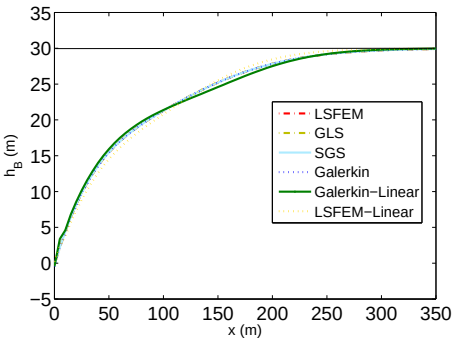

Figure 4.39: Saturation distribution after 50 *days* of CO_2 injection, $Cr_{max} = 5$, 100 linear elements vs. 50 quadratic elements [4].

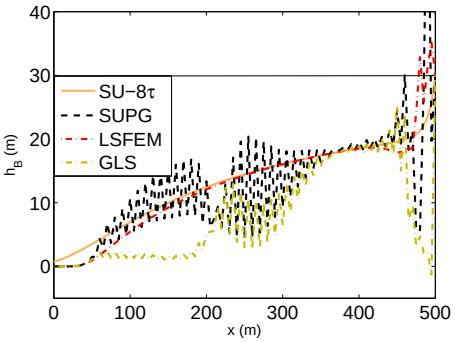

Figure 4.40: Saturation distribution after 350 *days* of CO_2 injection, $Cr_{max} = 5$, using 50 quadratic elements [4].

4.7.2 Example 2 - Multiple CO_2 Injectors in a Sloping Aquifer

In this example three injection wells inject CO_2 into an aquifer with a horizontal bottom boundary and a top boundary that slopes upward from left to right as shown in Figure 4.41. Except for z_{top}, which is a function of x, the system properties are the same as for example 1 and are given in Table 4.9.

Figure 4.42 compares the brine saturation distributions after 40 $days$ of injection with one timestep. Galerkin experiences significant oscillations and is not shown. The stabilized FEMs avoid these oscillations, however LSFEM computes a CO_2 depth that exceeds the aquifer depth at the centre of the domain.

Figure 4.43 shows the saturation distributions using a small timestep ($Cr = 0.0005$, $\Delta t = 7.7301 \times 10^{-4}$ $days$). Only LSFEM, GLS and SGS give smooth solutions that are in excellent agreement. Earlier in this chapter it was demonstrated that Galerkin, SU, SUPG, and LSFEM with linear elements result in oscillatory solutions when plumes merge. Only SU-8τ and SU-10τ were able to obtain non-oscillatory solutions. This example shows that in general, quadratic elements improve the ability of to capture merging plumes compared to linear elements.

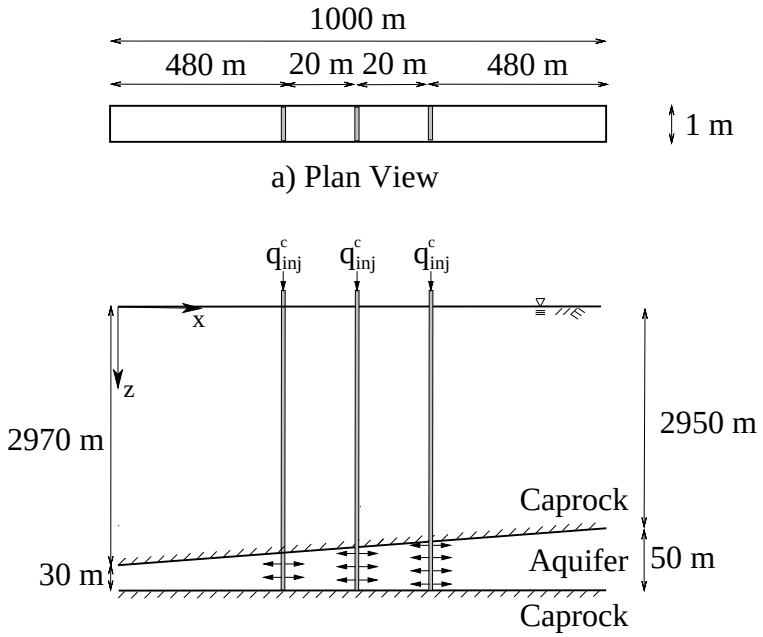

Figure 4.41: Three wells injecting into a variable depth aquifer [4].

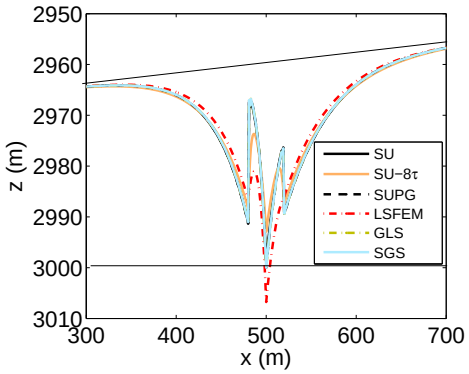

Figure 4.42: Saturation distribution after 40 *days* of CO_2 injection, $Cr_{max} = 25$ ($\Delta t = 40$ *days*), using 500 quadratic elements [4].

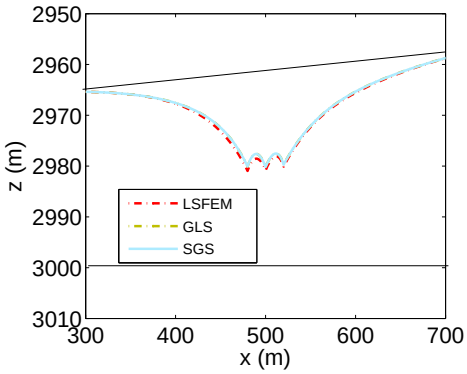

Figure 4.43: Saturation distribution after 40 *days* of CO_2 injection, $Cr_{max} = 0.0005$ ($\Delta t = 7.7301 \times 10^{-4}$ *days*), using 500 quadratic elements [4].

4.8 Chapter Conclusions

Carbon sequestration is a means to reduce CO_2 emissions by injecting CO_2 into deep saline aquifers for permanent storage. Numerical methods for modelling CO_2 plume evolution for carbon sequestration must be computationally efficient in order to be useful for stochastic

approaches.

Objective 1 (see Chapter 1) of this thesis has been accomplished in this chapter by using a vertically averaged multiphase flow formulation to reduce the number of degrees of freedom. The vertically averaged multiphase flow formulation consists of two fully coupled non-linear PDEs. One of these equations is solved for pressure and the other is solved for the average brine saturation. A sequential solution strategy is adopted to handle the coupling. In this chapter two sequential solution strategies were presented. The first strategy is a single iteration sequential solution (SS) approach and the second is a predictor-corrector (PC) approach.

The governing equation that describes the evolution of the brine contains an advective term, which can result in non-physical spurious oscillations in FEM. Objective 2 (see Chapter 1) of this thesis has been accomplished in this chapter by considering several stabilized FEMs (SU, SUPG, LSFEM, SGS, and GLS). The time discretization was performed with FDM.

One-dimensional linear and quadratic elements were used to approximate pressure and saturation. Linear elements cannot fully represent the stabilization terms for SUPG and LSFEM. Quadratic elements allow the full stabilization terms of SUPG and LSFEM to be represented. In addition, quadratic elements also permit the use of SGS and GLS stabilizations.

4.8.1 Comparison of Stabilized FEMs - One Dimensional Linear Elements

Three examples were used to compare several solution strategies for the saturation equation using linear one dimensional elements. First order convergence of the saturation error with respect to the L_2 norm was achieved for both the SS and PC solution strategies us-

ing Backward Euler (BE) time integration. It was demonstrated that, in general, a fully implicit Backward Euler (BE) time integration scheme provides superior stability properties compared to the Forward Euler (FE) and Crank-Nicholson (CN) time integration methods.

In general, when FE ($\theta = 0$) or CN ($\theta = 0.5$) time integration is used, small Courant numbers (e.g., $Cr_{max} \leq 0.005$) are required to obtain smooth solutions with the various stabilization methods.

BE ($\theta = 1$) provides the most reliable approximations in general. In addition to being stable and non-oscillatory for small timesteps, for large timesteps ($Cr_{max} \geq 3 - 5$) it can also produce smooth solutions depending on the sequential solution strategy and stabilization method. When the CO_2 plume encounters the Dirichlet domain boundaries oscillations can contaminate the brine saturation solution. In addition, oscillations can occur when two plumes meet. If SU stabilization is combined with 8τ or 10τ (eight or ten times a standard stabilization parameter definition) smooth solutions can be obtained for large timesteps when the plume encounters a boundary and when plumes merge. This is achieved by adding artificial diffusion to the system. No other stabilization scheme gives acceptable solutions using large timesteps when two plumes merge. Increasing the stabilization parameter for SUPG can sometimes increase the severity of the oscillations.

A PC scheme can be used to reduce oscillations at large timesteps with the BE method ($\theta = 1$), but comes with a significant increase in computational cost. The SS method gives a similar result as the PC scheme, but at a much lower computational cost.

The results from this study highlight the care that must be taken when using Dirichlet boundaries on the outflow boundaries or the simulation of multiple merging CO_2 plumes. It was demonstrated that a Galerkin FEM discretization of the saturation equation should

not be used if the CO_2 plume encounters a Dirichlet boundary or if multiple injection wells are present and large timesteps are used. SU combined with an increased value of the stabilization parameter (8τ or 10τ) is the most robust stabilization method examined. When combined with BE time integration it can achieve smooth solutions at large timesteps, and gives reasonable results even with a simple SS sequential solution strategy, which yields a computationally efficient framework to solve the vertically averaged multiphase flow equations presented in this work.

4.8.2 Comparison of Stabilized FEMs - One Dimensional Quadratic Elements

Two examples were provided to compare low order stabilizations (linear elements) and higher order stabilizations (quadratic elements). The SU-8τ approximation did not change significantly when quadratic elements were used. At large timesteps SU-8τ best matches the solutions obtained by all methods at the smallest Cr. The increased stabilization parameter provides sufficient artificial diffusion to compensate for the negative diffusion introduced by the Galerkin FEM approximation of the saturation equation.

SUPG and LSFEM approximations were more diffuse with quadratic elements. Quadratic elements were shown improve the stabilization properties of SUPG and LSFEM in some cases. SGS and GLS offer stable approximations over a larger range of timesteps compared to Galerkin, SU, SUPG, and LSFEM. SGS and GLS can provide smooth oscillation-free approximations for small Courant numbers ($Cr \leq 0.05$) and large Courant numbers ($Cr \geq 3$). SU-8τ provides smooth solutions when $Cr \geq 0.05$. SGS and GLS seem to be the preferable option for small Cr values, while SU-8τ seems to be the best option for large Cr values.

In general, quadratic elements improve the ability of the stabilized FEMs to achieve

smooth solutions compared with linear elements when multiple CO_2 plumes merge. However, quadratic elements introduce a greater tendency (compared to linear elements) for oscillations when the CO_2 exits the domain.

Chapter 5

Carbon Sequestration Simulations in Quasi-Three Dimensions with Adaptive Timesteps

This chapter is based on the journal article:

C. Ladubec and R. Gracie, "Quasi-Three Dimensional Multiphase Carbon Sequestration Simulation with the Finite Element Method", In Preparation.

In this article I was the first author where I lead the writing of the journal article. In addition, I lead the development of the MATLAB code, and the development of the formulation.

This chapter addresses objectives 3 and 4 (see Chapter 1) of the thesis:

- Compare the developed numerical model with a benchmark problem from existing literature.
- Reduce the computational cost of carbon sequestration injection simulations by using adaptive timesteps.

5.1 Introduction

Deep saline aquifers are an ideal location for long term storage of CO_2 [12]. These aquifers which are typically composed of sandstone, initially contain a salt water solution (brine) that gets displaced as the CO_2 is injected. Deep saline aquifers are typically one kilometre or more below the ground surface. The Shell Quest project in Alberta, for example, proposes to inject over one million tonnes of CO_2 per year into a saline aquifer at a depth of over 2 km [92].

Geological structures such as deep saline aquifers have properties that are uncertain to a large degree. The result of these uncertainties is the need for stochastic approaches for storage site assessment [90]. Stochastic approaches (e.g., Monte Carlo methods) involve the solution of the system equations with many, perhaps thousands, of different combinations of system properties. Since these simulations need to be run many times, the computational efficiency of the underlying numerical solution technique becomes very important. The computational cost of these simulations is very large owing to large domain sizes (e.g., km^2) and long injection times (e.g., $years$).

It is important to compare the current formulation with other carbon sequestration simulators. This is done via a benchmark study that compares eleven different simulators. In order to compare with the results of the benchmark study, the discretization from Chapter 4 is extended to two dimensions (quasi-three dimensions). Quasi-three dimensional refers to the fact that the third dimension (depth) is vertically averaged, thus making the problem essentially two dimensional.

In this chapter an adaptive timestepping algorithm is developed to take advantage of larger permissible timesteps as the simulation progresses in order to improve computational efficiency. Constant timesteps were used in Chapter 4. The current formulation is

demonstrated by using several examples. Adaptive timesteps are shown to significantly reduce the computational cost of the formulation.

The Finite Element Method (FEM) is used to model the pressure field. The Streamline Upwind method is used to stabilize an FEM spatial discretization and combined with a Finite Difference Method (FDM) discretization of time (SU-FEM-FDM) to model the evolution of the brine and CO_2 phase saturations. Non-physical oscillations can occur in the solution of the brine equation making stabilized FEMs necessary. This chapter uses a stabilization method with a magnified stabilization parameter from Chapter 4. This stabilization was demonstrated to be give smooth oscillation-free solutions for a wide range of timestep sizes.

This chapter is organized as follows. First, the governing equations of the problem in quasi-three dimensions are presented. Then, the pressure equation is described along with the weak form and the FEM discretization. Next, the saturation weak form and the SU-FEM-FDM discretization is presented. Then, the solution procedure is described. The chapter concludes with four examples. Results from the current formulation are compared against a benchmark study in [8] where eleven different simulators were compared via a well defined test problem to predict CO_2 plume movement. The examples demonstrate the significant improvement in computational efficiency from adaptive timesteps.

5.2 Problem Statement

A vertically averaged multiphase flow formulation is used to model the large scale CO_2 plume evolution. Figure 2.1 illustrates the problem. The governing equations are provided by the mass balance equations for the CO_2 and brine phases [3].

$$\phi(1 - S_B)\frac{\partial h_C}{\partial t} + \nabla \cdot \hat{\mathbf{q}}_C = q_C^{inj} \tag{5.1}$$

$$\phi(1 - S_B)\frac{\partial h_B}{\partial t} + \nabla \cdot \hat{\mathbf{q}}_B = 0 \tag{5.2}$$

where ϕ is the porosity of the aquifer, S_B is the residual saturation of brine in the aquifer, $h_C(\mathbf{x}, t)$ is the depth of CO_2, $h_B(\mathbf{x}, t)$ is the depth of brine, $\hat{\mathbf{q}}_C(\mathbf{x}, t)$ is the vertically averaged CO_2 flux, $\hat{\mathbf{q}}_B(\mathbf{x}, t)$ is the vertically averaged brine flux, and $q_C^{inj}(\mathbf{x}, t)$ is the CO_2 injection term.

The CO_2 injection term is defined by:

$$q_C^{inj}(\mathbf{x}, t) = Q_C^{inj}(t)\delta(\mathbf{x} - \mathbf{x_{inj}}) \tag{5.3}$$

where $Q_C^{inj}(t)$ is the rate of CO_2 injection, $\mathbf{x_{inj}}$ is the location of the injection or extraction well, and $\delta()$ is the Dirac delta function.

The vertically averaged fluxes are computed by the multiphase extension of Darcy's Law [3]:

$$\hat{\mathbf{q}}_C = -h_C\frac{kk_C^{rel}}{\mu_C}(\nabla p_{bot} - \rho_B g \nabla H + \Delta\rho g \nabla h_C + \rho_C g \nabla z_{top}) \tag{5.4}$$

$$\hat{\mathbf{q}}_B = -h_B\frac{k}{\mu_B}(\nabla p_{bot} + \rho_B g \nabla z_{bot}) \tag{5.5}$$

where k is the permeability of the aquifer, k_C^{rel} is the relative permeability of CO_2 compared to brine, μ_C is the dynamic viscosity of CO_2 , μ_B is the dynamic viscosity of brine, $p_{bot}(\mathbf{x}, t)$ is the pressure at the bottom of the aquifer, ρ_C is the density of CO_2, ρ_B is the density of brine, $\Delta\rho = \rho_B - \rho_C$, g is the gravitational constant, $z_{top}(\mathbf{x})$ defines the top boundary of the aquifer, $z_{bot}(\mathbf{x})$ defines the bottom boundary of the aquifer, and $H(\mathbf{x}) = z_{bot}(\mathbf{x}) - z_{top}(\mathbf{x})$

is the thickness of the aquifer.

The governing equations (5.1) and (5.2) are manipulated to obtain one equation that is solved for the pressure at the bottom of the aquifer (the pressure equation) and one that is solved for the average depth of the brine and thus the CO_2 (the saturation equation). These two equations will be discussed in the next two sections.

5.3 Pressure Equation

The mass balance equations (5.1) and (5.2) are added together to give the pressure equation. The transient terms disappear and the result is a steady state pressure equation.

$$\begin{aligned} &\nabla \cdot \left(h_C \frac{k k_{REL}^C}{\mu_C} (\nabla p_{bot} + \Delta\rho g \nabla h_C \rho_B g \nabla H + \rho_C g \nabla z_{top}) \right) \\ &+ \nabla \cdot \left(h_B \frac{k}{\mu_B} (\nabla p_{bot} + \rho_B g \nabla z_{bot}) \right) = -q_C^{inj}, \quad \mathbf{x} \in \Omega \end{aligned} \tag{5.6}$$

and

$$p_{bot}(\mathbf{x}, t) = \overline{p}_{bot}(\mathbf{x}, t) \text{ on } \Gamma_p \tag{5.7}$$

where Γ_p is the boundary of Ω. The domain is defined in Figure 5.1. The domain of the injection well is indicated by Ω_{well}.

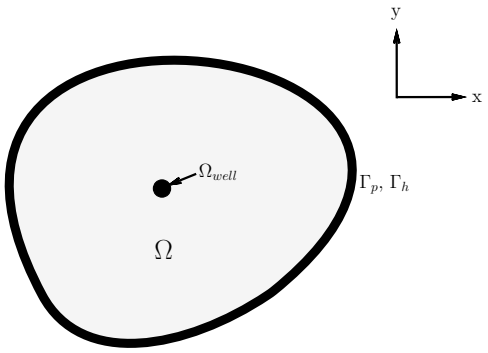

Figure 5.1: Problem domain [6].

5.3.1 Weak Form

The pressure equation is converted to the weak form before the FEM discretization is performed. The weak form of the pressure equation is: find $p_{bot}(x,t) \in U$ such that

$$\begin{aligned}
&\int_\Omega \nabla\delta p_{bot} \cdot h_B \frac{k}{\mu_B} \nabla p_{bot} d\Omega + \int_\Omega \nabla\delta p_{bot} \cdot h_B \frac{k}{\mu_B} \rho_B g \nabla z_{bot} d\Omega + \int_\Omega \nabla\delta p_{bot} \cdot h_C \frac{k k_C^{rel}}{\mu_C} \Delta\rho g \nabla h_C d\Omega \\
&- \int_\Omega \nabla\delta p_{bot} \cdot h_C \frac{k k_C^{rel}}{\mu_C} \rho_B g \nabla H d\Omega + \int_\Omega \nabla\delta p_{bot} \cdot h_C \frac{k k_C^{rel}}{\mu_C} \rho_C g \nabla z_{top} d\Omega + \int_\Omega \nabla\delta p_{bot} \cdot h_C \frac{k k_C^{rel}}{\mu_C} \nabla p_{bot} d\Omega \\
&= \int_\Omega \delta p_{bot} q_C^{inj} d\Omega, \forall \delta p_{bot} \in U_0.
\end{aligned} \tag{5.8}$$

where δp_{bot} is a weight function. The function spaces are

$$\begin{aligned}
U &= \{p_{bot}(\mathbf{x}) | p_{bot}(\mathbf{x}) \in H^1 \backslash \Omega^{well}, p_{bot}(\mathbf{x}) = \overline{p}_{bot} \text{ on } \Gamma_p\} \\
U_0 &= \{\delta p_{bot}(\mathbf{x}) | \delta p_{bot}(\mathbf{x}) \in H^1 \backslash \Omega^{well}, \delta p_{bot}(\mathbf{x}) = 0 \text{ on } \Gamma_p\}
\end{aligned} \tag{5.9}$$

The choice of the approximation spaces given are based on their application in similar problems. The author has no knowledge of a proof that these are the correct spaces for this problem.

5.3.2 FEM Discretization

The weak form of the pressure equation (5.8) is discretized by replacing the weight functions and the pressure by FEM shape functions. The FEM approximation of the pressure is:

$$p^h(\mathbf{x}) = \sum_{I \in \mathcal{N}} N_I(\mathbf{x}) p_I, \mathbf{x} \in \Omega \tag{5.10}$$

where $\mathcal{N}$ is the set of all nodes, p_I is a vector containing the nodal pressures, $N_I(\mathbf{x})$ is the shape function for node I.

The pressure approximation can also be written as:

$$p^h(\mathbf{x}) = \mathbf{N}\mathbf{p}_{bot} \tag{5.11}$$

where $\mathbf{N}$ is a matrix containing the shape functions for all nodes and $\mathbf{p_{bot}}^\top = \{p_1, p_2, ..., p_{nn}\}$.

The FEM discretization of the pressure equation becomes:

$$\mathbf{K}_p\mathbf{p}_{bot} = \mathbf{F}_p \tag{5.12}$$

where $\mathbf{K}_p$ is the diffusion matrix and the flux vector has four contributions:

$$\mathbf{F}_p = \mathbf{F}_{p1} + \mathbf{F}_{p2} + \mathbf{F}_{p3} \tag{5.13}$$

where $\mathbf{F}_{p1}$ is the injection flux vector, $\mathbf{F}_{p2}$ is the buoyancy flux vector, and $\mathbf{F}_{p3}$ is the slope flux vector.

The matrices and vectors are

$$\mathbf{K}_p^e = \int_{\Omega^e} \mathbf{B^e}^\mathsf{T} \left(\frac{h_C k_C^{rel}}{\mu_C} + \frac{h_B}{\mu_B} \right) k \mathbf{B^e} d\Omega^e \tag{5.14}$$

$$\mathbf{F}_{p1}^e = \int_{\Omega^e} \mathbf{N^e}^\mathsf{T} q_C^{inj} d\Omega^e \tag{5.15}$$

$$\mathbf{F}_{p2}^e = -\int_{\Omega^e} \mathbf{B^e}^\mathsf{T} \frac{k k_C^{rel}}{\mu_C} \Delta\rho g h_C \nabla h_C d\Omega^e \tag{5.16}$$

$$\mathbf{F}_{p3}^e = \int_{\Omega^e} \mathbf{B^e}^\mathsf{T} \left(h_C \frac{k k_C^{rel}}{\mu_C} (\rho_B g \nabla H - \rho_C g \nabla z_{top}) - h_B \frac{k}{\mu_B} \rho_B g \nabla z_{bot} \right) d\Omega^e \tag{5.17}$$

where $\mathbf{B^e} = \nabla \mathbf{N^e}$ is a matrix containing the shape functions derivatives for element e.

The eXtended Finite Element Method (XFEM) has successfully been used to allow

accurate pressure distributions using coarse meshes even when the injection occurs mid element [45, 46, 58]. This will be discussed in detail in the next chapter.

5.4 Saturation Equation

The brine mass balance equation (5.2) is used as the saturation equation to determine the average brine saturation in the aquifer. With the average brine saturation known the average CO_2 saturation can computed. The saturation equation is given by:

$$\dot{h}_B + \mathbf{a} \cdot \nabla h_B + \sigma h_B = 0, \, \mathbf{x} \in \Omega, \, \mathrm{t} \ \in [0, t_{end}] \tag{5.18}$$

$$\begin{aligned} h_B(\mathbf{x}, t) &= \overline{h}_B(\mathbf{x}, t) \text{ on } \Gamma_h \\ h_B(\mathbf{x}, 0) &= h_{Bo}(\mathbf{x}) \text{ on } \Omega \end{aligned} \tag{5.19}$$

where t_{end} is the end time of the simulation, $\overline{h}_B(\mathbf{x}, t)$ is the prescribed brine depth, Γ_h is the essential boundary of Ω, $h_{Bo}(\mathbf{x})$ is the initial brine depth in the aquifer. The advective velocity vector is given by:

$$\mathbf{a} = -\frac{k}{\phi(1 - S_B)\mu_B}(\nabla p_{bot} + \rho_B g \nabla z_{bot}) \tag{5.20}$$

and the reaction term is given by:

$$\sigma = -\frac{k}{\phi(1 - S_B)\mu_B}(\nabla^2 p_{bot} + \rho_B g \nabla^2 z_{bot}) \tag{5.21}$$

When bilinear elements are used $\sigma = 0$.

5.4.1 Weak Form

The weak form is obtained by multiplying (5.2) by a weight function and integrating over the domain. Green's Formula is used to reduce the continuity requirements, which generates a boundary flux term. A stabilization term is added to control the oscillations that can result from a Galerkin FEM discretization of the saturation equation (5.2). The stabilization term can be considered as an artificial diffusion that is added to the system which offsets the negative diffusion introduced by the Galerkin FEM discretization of the advection term. The weak form of (5.2) can be written as: find $h_B(x,t) \in W$ such that:

$$\int_\Omega \delta h_B \cdot \frac{\partial h_B}{\partial t} d\Omega - \int_\Omega \nabla \delta h_B \cdot \mathbf{a} h_B d\Omega + \sum_e \int_{\Omega^e} (\tau^e \mathbf{a} \cdot \nabla \delta h_B) \cdot (\mathbf{a} \cdot \nabla h_B)\, d\Omega^e = 0,\ \forall \delta h_B \in W_0. \tag{5.22}$$

where δh_B is the weight function, $\mathbf{a}$ is the advective velocity vector, τ^e is the stabilization parameter, and W and W_0 are the appropriate function spaces for $h_B(\mathbf{x},t)$ and $\delta h_B(\mathbf{x},t)$, respectively. The stabilization parameter τ^e is given by [91]:

$$\tau^e = \left(\left(\frac{1}{\theta \Delta t} \right)^2 + \left(\frac{2\|\mathbf{a}\|}{h^e} \right)^2 \right)^{-\frac{1}{2}} \tag{5.23}$$

5.4.2 Streamline Upwind (SU) FEM - FDM Discretization

A standard linear FEM approximation of the average brine saturation is given by:

$$h_B(\mathbf{x},t) = \sum_{I \in \mathcal{N}} N_I(\mathbf{x}) h_I(t) \tag{5.24}$$

This approximation is inserted into the weak form (5.22) to obtain the discretized matrices and vectors. The system of equations to be solved becomes:

$$[\mathbf{C_S}]\{\dot{\mathbf{h_B}}\} + [\mathbf{K_S}]\{\mathbf{h_B}\} = \{\mathbf{F_S}\} \tag{5.25}$$

where $\mathbf{C_S}$ is the storage matrix, $\mathbf{K_S}$ is the advection matrix and $\mathbf{F_S}$ is the boundary flux vector, $\mathbf{h_B}$ is the unknown vector which contains nodal brine depths in the aquifer and $h_B(\mathbf{x}, t) = H(\mathbf{x}) - h_C(\mathbf{x}, t)$, $\dot{\mathbf{h_B}}$ is the derivative with respect to time of $h_B(\mathbf{x}, t)$.

The Streamline Upwind (SU) method [73] is similar to the Galerkin discretization, except a stabilization matrix is added to the Galerkin advection matrix. The Galerkin advection matrix is given by:

$$\mathbf{K}_G^e = -\int_{\Omega^e} \mathbf{B^{e\mathsf{T}}} \mathbf{a} \mathbf{N^e} d\Omega^e \tag{5.26}$$

and the stabilization matrix is given by:

$$\mathbf{K}_{SU}^{e,stab} = \int_{\Omega^e} \mathbf{B^{e\mathsf{T}}} \tau^e \mathbf{a}\mathbf{a}^{\mathsf{T}} \mathbf{B^e} d\Omega^e \tag{5.27}$$

The SU-FEM advection matrix is obtained by adding the Galerkin advection matrix and the stabilization matrix.

$$\mathbf{K}_S = \mathbf{K}_G + \mathbf{K}_{SU}^{stab} \tag{5.28}$$

The storage matrix is given by:

$$\mathbf{C}_S^e = \int_{\Omega^e} \mathbf{N^{e\mathsf{T}}} \mathbf{N^e} d\Omega^e \tag{5.29}$$

where $\mathbf{N}^e$ are the shape functions for element e, and $\mathbf{B}^e = \nabla \mathbf{N}^e$.

The Backward Euler (BE) method was shown in Chapter 4 to provide superior stability properties compared to the Forward Euler and Crank-Nicholson FDM methods. As such, BE ($\theta = 1$) is used here to discretize (5.22) in time. This results in the following system of equations:

$$[\mathbf{K_{eff}}]^{n+1}\{\mathbf{h_B}\}^{n+1} = \{\mathbf{F_{eff}}\}^{n+1} \tag{5.30}$$

where

$$[\mathbf{K_{eff}}]^{n+1} = [\mathbf{C_S}] + \Delta t[\mathbf{K_S}]^{n+1} \tag{5.31}$$

and

$$\{\mathbf{F_{eff}}\}^{n+1} = [\mathbf{C_S}]\{\mathbf{h_B}\}^{n} \tag{5.32}$$

The matrices and vectors $[\mathbf{K_S}]$ and $[\mathbf{C_S}]$ are defined by (5.28) and (5.29).

5.4.3 Adaptive Time Stepping

To improve the computational efficiency an adaptive timestepping algorithm is developed. This enables larger timesteps to be used later in time as the advective velocities are reduced. The pressure gradient in the CO_2 plume has its largest absolute value when the injection begins. Over time, as the CO_2 plume spreads, the pressure gradient (and thus the advective velocity) decreases at the CO_2 plume front. The size of timestep $n+1$ is computed from:

$$\Delta t^{n+1} = \min_e \left(\frac{\sqrt{\Delta x^2 + \Delta y^2}}{\|\mathbf{a}_e^n\|} \right) Cr \tag{5.33}$$

where Cr is the Courant number, and is given by:

$$Cr = \frac{\|\mathbf{a}\|\Delta t}{\sqrt{\Delta x^2 + \Delta y^2}} \tag{5.34}$$

The Courant number is selected before the analysis begins, in order to balance accuracy an stability. From the fixed Courant number, the timestep for each time is computed from (5.33). The adaptive timestepping allows a constant Cr value for the duration of the simulation.

5.5 Examples

In this section four examples are used to demonstrate the formulation described in this chapter. In the first example, the CO_2 is injected into a horizontal aquifer to compare with other simulators from a benchmark problem from [8]. In the second example, five injection wells inject CO_2 into a single aquifer. In the third example, CO_2 is injected into an upsloping aquifer and the migration of the CO_2 is modelled. In the fourth example, CO_2 is injected into a dome shaped aquifer.

5.5.1 Example 1 - Comparison with Benchmark

In this example the current formulation is compared with the benchmark simulation in [8]. The problem is illustrated in Figure 5.2 and the system properties are given in Table 5.1. A single injection well injects CO_2 at a rate of 1600 m^3/day for 10 $days$. The aquifer is horizontal and has a constant thickness of 30 m. The top boundary of the aquifer is located at a depth of 2970 m.

A ficticous (not modelled) leaky well is located 100 m away. Eleven different simulators

are compared using this benchmark problem in [8]. The time for the CO_2 plume to reach the leaky well is measured and compared. A summary of these results is given in Table 5.2. The arrival time ranges from 4 to 19 *days*, while nine of the 13 results had arrival times that ranged between 7 and 10 *days*.

Figure 5.3 shows the arrival time at the leaky well for several different mesh densities. SU gives smooth stable results for each spatial mesh. When SU is not used (i.e., Galerkin is used) unphysical spatial oscillations can develop, particularly when using 160,000 elements. When the element edges are less than 2 m, the arrival time is consistently 6.6 *days*. This result is in agreement with the lower end of the range from Table 5.2. The result from the current formulation agrees very well with the VESA results in particular which is based on similar assumptions. VESA is based on vertically averaged multiphase flow, but the numerical discretization is based on the FDM in space. The wide range of results in [8] is explained by the variation of numerical diffusion in the various solutions, but the authors argue that due to the large uncertainty in the system properties, the issue of numerical diffusion is not a prohibitive problem.

The saturation and pressure distributions after 10 *days* are shown in Figure 5.4 and Figure 5.5 respectively. Timesteps were controlled by $Cr = 10$ and the spatial discretization was done using 250,000 ($2\ m \times 2\ m$) elements. The saturation and pressure distributions are replotted along line A-A (Figure 5.2) in Figures 5.6 and 5.7. The pressure approximation can be improved using the eXtended Finite Element Method (XFEM) [45, 46, 58], particularly when the injection occurs mid-element. This is considered in Chapter 6.

Figure 5.8 shows how the adaptive timestep changes over the duration of the simulation. The timestep at the end of the simulation is over five times larger than the initial

timestep. If a constant timesteps were used, 16 timesteps would be required, but with the adaptive timestep, only 4 are needed.

The results of this example demonstrate that the current formulation is agreement with a range of simulators. In particular, the current formulation matches very well with the simulator from [8] that most closely matches the assumptions made in the current formulation. The SU method provides smooth solutions, while the Galerkin FEM can be contaminated with non-physical oscillations as shown in Chapter 4. In addition, adaptive timestepping reduced the computational costs of the problem by about 75 %.

Change in Permeability

Figure 5.9 shows the domain with a non-uniform permeability. The permeability drops from $2 \times 10^{-14}\ m^2$ to $2 \times 10^{-15}\ m^2$ when $x = 550\ m$. The resulting saturation and pressure distributions are shown along A-A in Figure 5.10 and Figure 5.11 respectively. When the plume encounters the change in k, it is much easier for the flow to go in the other direction, and therefore further injection leads to the plume preferentially flowing in the direction of the largest permeability as expected. The saturation distribution and the pressure distribution are unsymmetrical as expected.

Table 5.1: System properties for example 1 [5].

Property	Value	Units
μ_B	2.535×10^{-4}	Ns/m^2
μ_C	3.950×10^{-5}	Ns/m^2
ρ_B	1045	kg/m^3
ρ_C	479	kg/m^3
S_B	0	-
ϕ	0.15	-
k	2×10^{-14}	m^2
k_C^{rel}	1	-
q_{inj}	1600	m^3/day

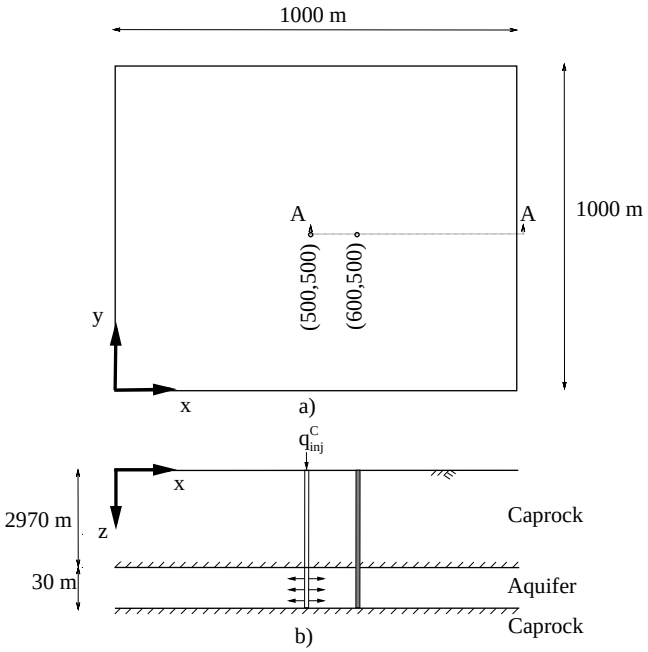

Figure 5.2: Example 1: One injection well injecting CO_2 into a single aquifer [5].

Table 5.2: Summary of results of benchmark study [8].

Simulator	Arrival Time (*days*)
COORES	8
DuMux	6
ECLIPSE	8
FEHM	4
IPARS-CO_2	10
MUFTE	8
RockFlow	19
ELSA	14
TOUGH2/ECO2N #1	4
TOUGH2/ECO2N #2	10
TOUGH2/ECO2N #3 - refined mesh	8
TOUGH2	9
VESA	7

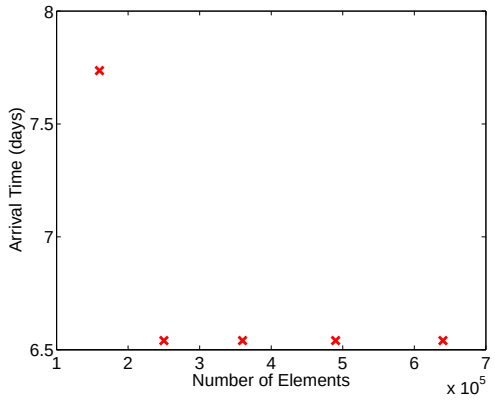

Figure 5.3: Effect of number of elements on arrival time of CO_2 plume at leaky well located 100 m away [5].

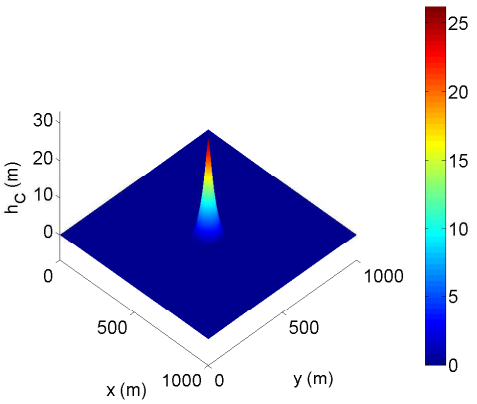

Figure 5.4: Saturation distribution after 10 *days* of CO_2 injection, $Cr = 10$, using 250,000 uniform sized bilinear elements [5].

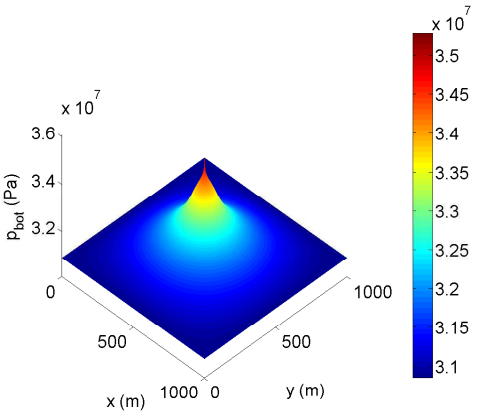

Figure 5.5: Pressure distribution after 10 *days* of CO_2 injection, $Cr = 10$, using 250,000 uniform sized bilinear elements [5].

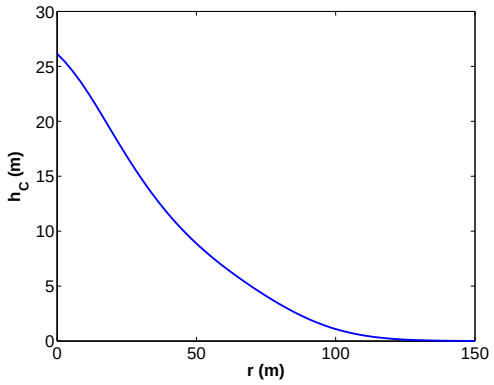

Figure 5.6: Saturation distribution along section A-A (Figure 5.2) after 10 *days* of CO_2 injection, $Cr = 10$, using 250,000 uniform sized bilinear elements [5].

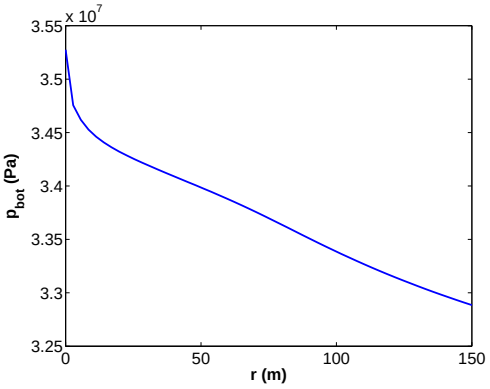

Figure 5.7: Pressure distribution along section A-A (Figure 5.2) after 10 *days* of CO_2 injection, $Cr = 10$, using 250,000 uniform sized bilinear elements [5].

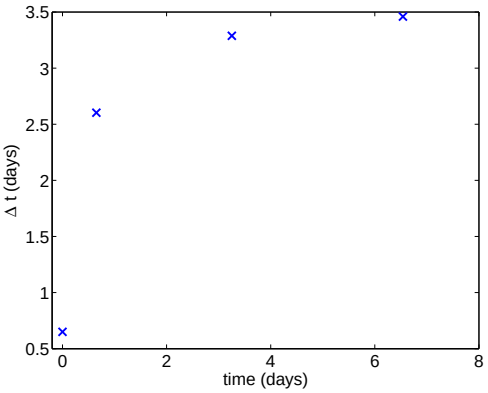

Figure 5.8: Adaptive timestep size over the duration of the simulation, $Cr = 10$, using 250,000 uniform sized bilinear elements [5].

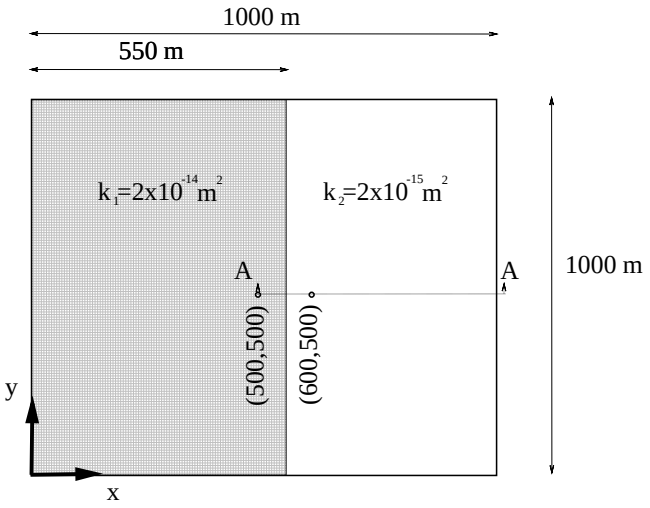

Figure 5.9: Change in permeability at $x = 550\ m$ [5].

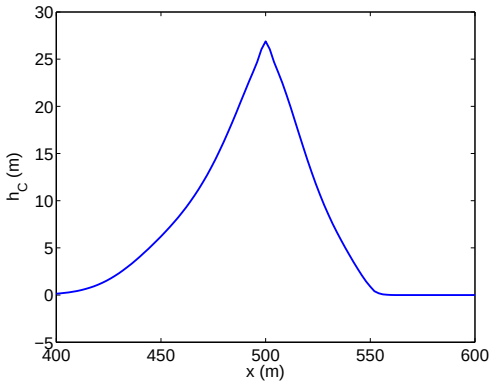

Figure 5.10: Saturation distribution (along A-A) after 10 *days* of CO_2 injection, $Cr = 10$, using 250,000 uniform sized bilinear elements - change in permeability at $x = 550\ m$ [5].

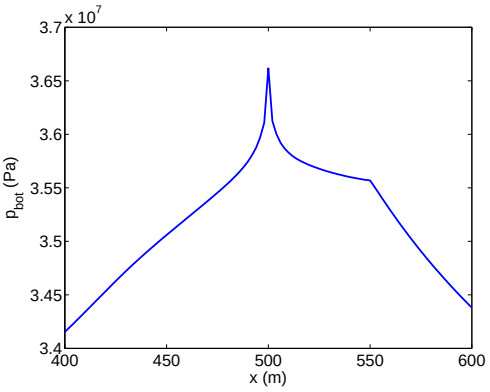

Figure 5.11: Pressure distribution (along A-A) after 10 *days* of CO_2 injection, $Cr = 10$, using 250,000 uniform sized bilinear elements - change in permeability at $x = 550\ m$ [5].

5.5.2 Example 2 - Multiple CO_2 Injection Wells

In the second example five injection wells inject CO_2 into a deep saline aquifer located at depth of 2970 m as shown in Figure 5.12. Other than the number of wells and the injection rates the system properties are the same as for example 1 (see Table 5.1). Each well injects at 320 m^3/day. Two planes of symmetry exist and thus after applying appropriate symmetry boundary conditions the setup of the model is shown in Figure 5.13.

After 60 *days* of injection the saturation and pressure distributions are shown in Figure 5.14 and Figure 5.15 respectively. In addition plots along section A-A (Figure 5.13) are shown for the saturation and pressure distribution in Figure 5.16 and Figure 5.17 respectively. There are two CO_2 plumes and two pressure spikes due to the two injection wells.

Figure 5.18 shows the size of the adaptive timestep over the course of the simulation. The timestep starts out at 2 *days*, and increases to about 12.6 *days*, before reducing to 8.8 *days*. The reduction in timestep at the end is so the predetermined end time can be exactly reached. The maximum timestep is over five times larger than the initial timestep. Thirty constant timesteps would be required, but adaptive timesteps require only 6 timesteps, a reduction in computational cost of approximately 80 %.

This example shows that the current formulation is able to obtain smooth stable solutions with two multiple injection wells that are closely spaced. The significant improvements to computational efficiency that can result from adaptive timestepping was also demonstrated.

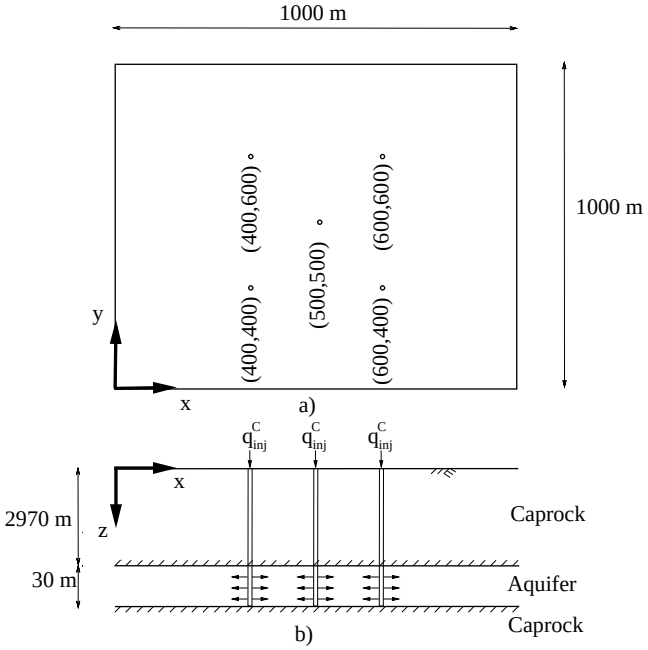

Figure 5.12: Example 2: Five injection wells injecting CO_2 into a single aquifer [5].

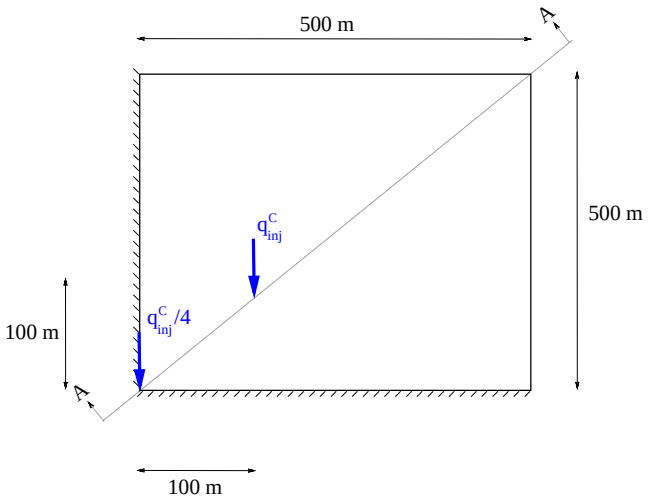

Figure 5.13: Example 2: Model after application of symmetric boundary conditions [5].

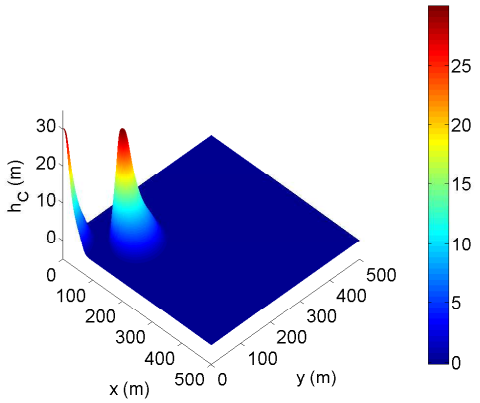

Figure 5.14: Saturation distribution after 60 *days* of CO_2 injection, $Cr = 100$, using 500×500 bilinear elements [5].

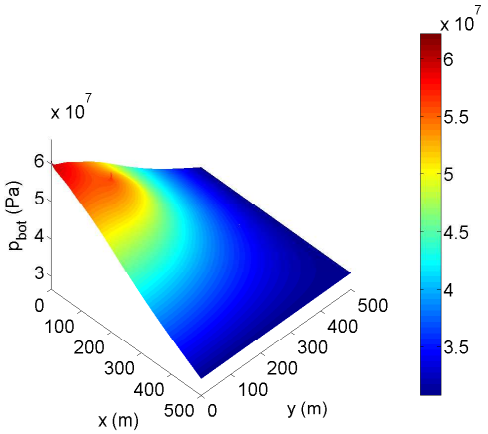

Figure 5.15: Pressure distribution after 60 *days* of CO_2 injection, $Cr = 100$, using 500×500 bilinear elements [5].

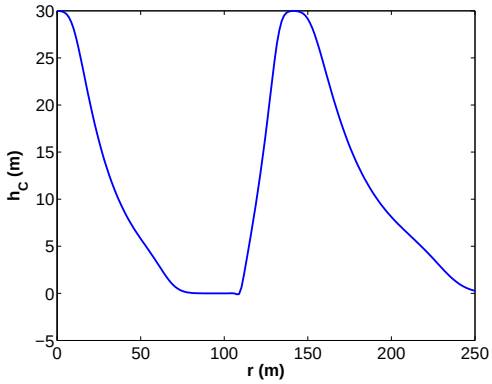

Figure 5.16: Saturation distribution along section A-A (Figure 5.13) after 60 *days* of CO_2 injection, $Cr = 100$, using 500×500 bilinear elements [5].

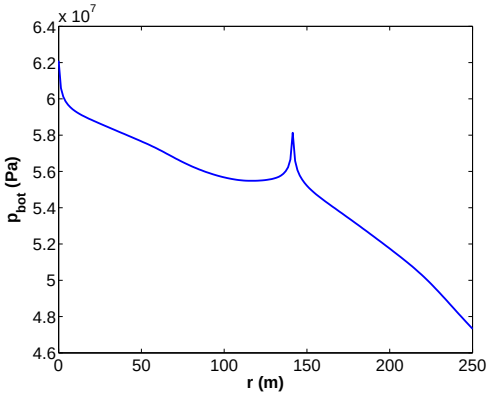

Figure 5.17: Pressure distribution along section A-A (Figure 5.13) after 60 *days* of CO_2 injection, $Cr = 100$, using 500×500 bilinear elements [5].

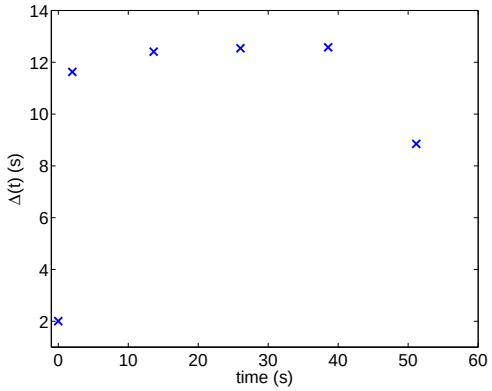

Figure 5.18: Adaptive timestep size over the duration of the simulation, $Cr = 100$, using 250,000 uniform sized bilinear elements [5].

5.5.3 Example 3 - Upslope CO_2 Migration

In the third example CO_2 is injected into an upsloping, but constant thickness aquifer as shown in Figure 5.19. The system properties are given in Table 5.1.

The saturation distribution after 500 *days* of injection is shown in Figure 5.20. The saturation distribution along section A-A (Figure 5.19) is shown in Figure 5.22. It can be clearly be seen that the due to the upsloping aquifers and the density difference between the CO_2 and the brine, the CO_2 preferentially migrates upslope. The pressure distribution after 500 *days* is shown in Figure 5.21 and the distribution along A-A is shown in Figure 5.23. The unsymmetrical pressure distribution reflects the upsloping aquifer and the upslope migration of the CO_2.

The size of each timestep is shown in Figure 5.24. The initial timestep is 6.5 *days* and increases to a maximum of 41.3 *days*. The reduction of the timestep to 7.1 *days* at the end is to so that the endtime can be reached exactly. Seventy-seven constant timesteps would be needed with constant timesteps for this problem, but only 14 timesteps are required with adaptive timesteps. Both the constant and adaptive timesteps provide a similar level of accuracy. This represents an approximate 82 % reduction in computational cost.

In this example the behaviour of the CO_2 plume is modelled after the injection into an upsloping aquifer. The unsymmetrical pressure and saturation distribution demonstrate the ability of the model to capture upsloping effects created by the density difference between the CO_2 and the brine.

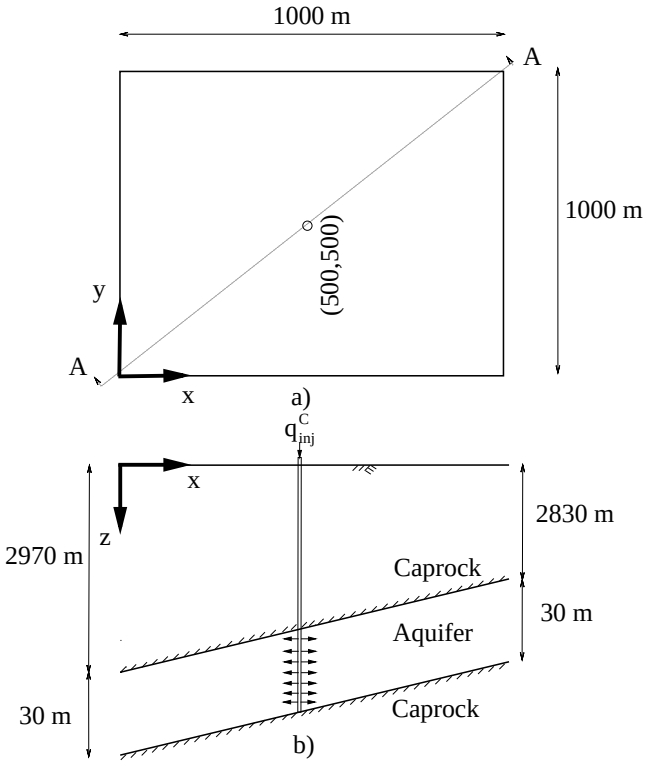

Figure 5.19: Example 3: One injection well injecting CO_2 into a single upsloping aquifer [5].

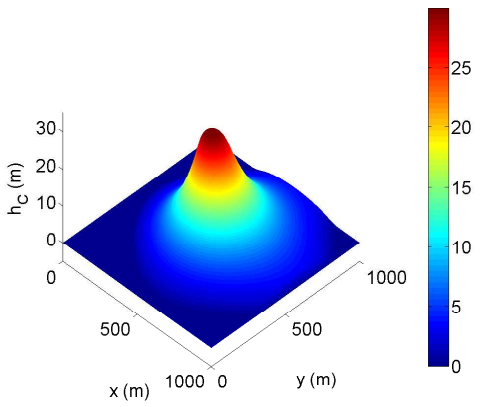

Figure 5.20: Saturation distribution after 500 *days* of CO_2 injection, $Cr = 100$, using 500×500 bilinear elements [5].

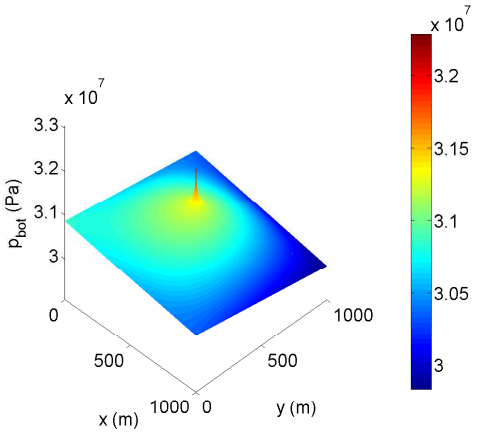

Figure 5.21: Pressure distribution after 500 *days* of CO_2 injection, $Cr = 100$, using 500×500 bilinear elements [5].

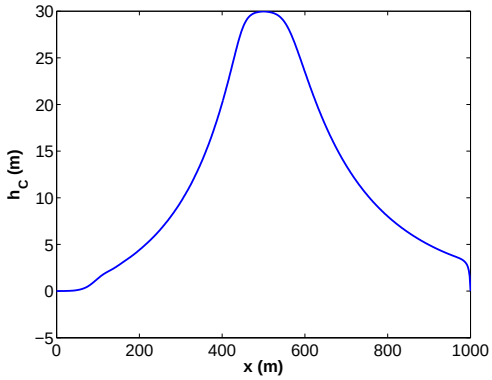

Figure 5.22: Saturation distribution along section A-A (Figure 5.19) after 500 *days* of CO_2 injection, $Cr = 100$, using 500 $\times$ 500 bilinear elements [5].

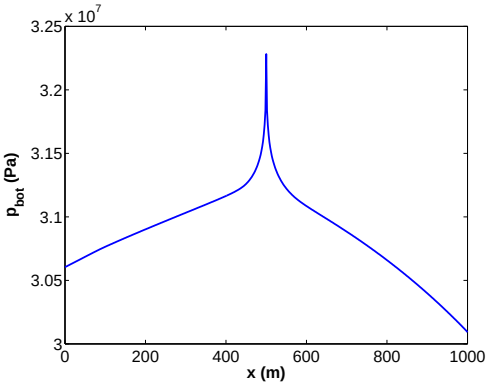

Figure 5.23: Pressure distribution along section A-A (Figure 5.19) after 500 *days* of CO_2 injection, $Cr = 100$, using 500 $\times$ 500 bilinear elements [5].

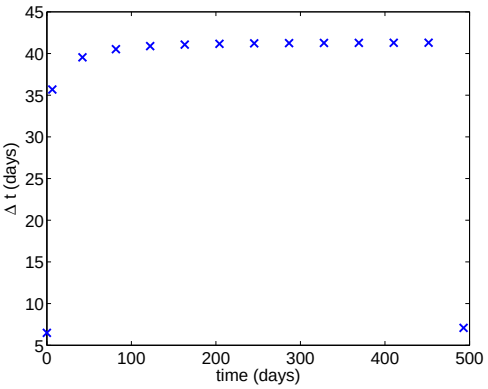

Figure 5.24: Adaptive timestep size over the duration of the simulation, $Cr = 100$, using 250,000 uniform sized bilinear elements [5].

5.5.4 Example 4 - Injection of CO_2 into a Dome Shaped Aquifer

In the final example example CO_2 is injected into an aquifer that contains a dome structure. The setup is given in Figure 5.25. The CO_2 is injected at a rate of 1600 m^3/day into the top of the dome. This problem is symmetric, and the proper symmetric boundary conditions are used.

Figure 5.26 shows the saturation distribution after 325 *days*. The associated pressure distribution is shown in Figure 5.27. The saturation and pressures along slice A-A (Figure 5.25) are shown in Figure 5.28 and Figure 5.29. The CO_2 first fills the dome, since the CO_2 rises above the brine due the differences in densities. Once the dome is filled, the CO_2 begins to spread laterally beyond the extent of the dome. This demonstrates that the current formulation is able to handle arbitrary changes in aquifer boundaries.

The timestep size over time is shown in Figure 5.30. The timestep starts off at $\Delta t = 6.3$ *days*, reaching a maximum of $\Delta t = 40.5$ *days*, before falling to $\Delta t = 0.7$ *days* in order to reach the goal end time. This represents a 81 % reduction in number of timesteps compared to constant timesteps.

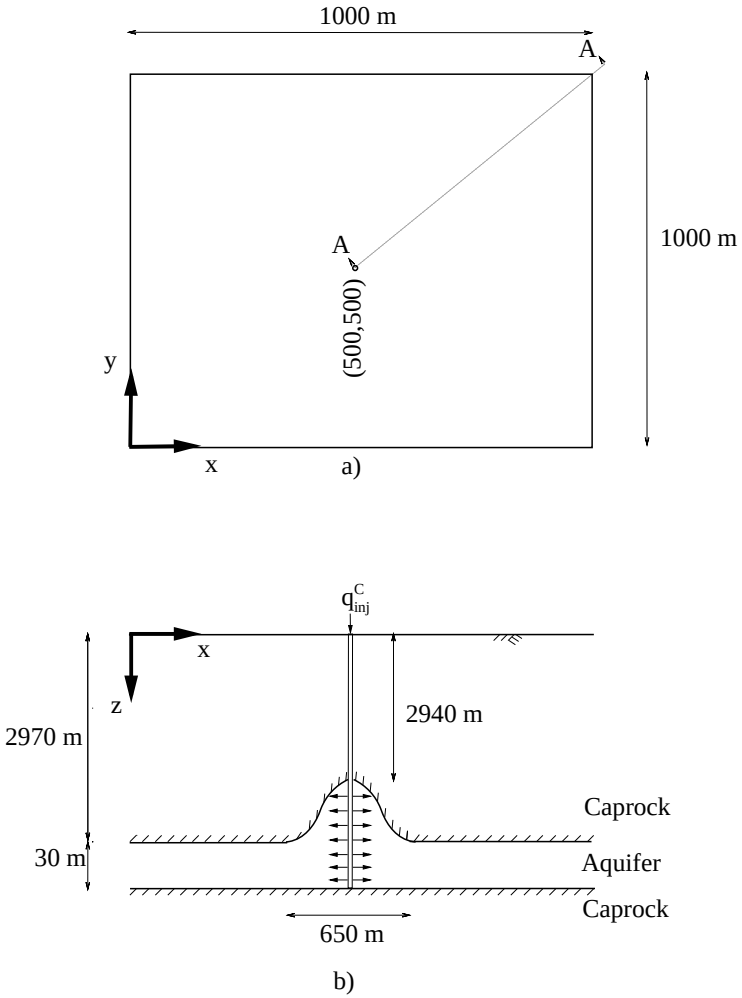

Figure 5.25: Example 4: One injection well injecting CO_2 into a aquifer with a dome structure [5].

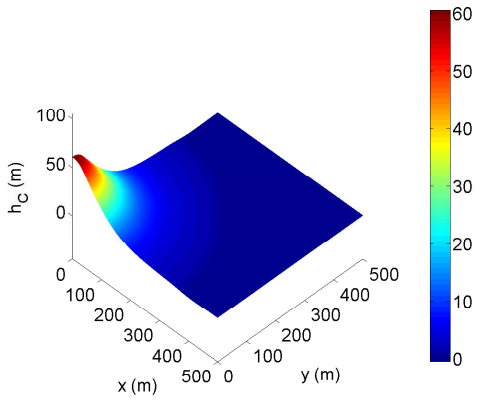

Figure 5.26: Saturation distribution after 325 *days* of CO_2 injection, $Cr = 100$, using 300×300 bilinear elements [5].

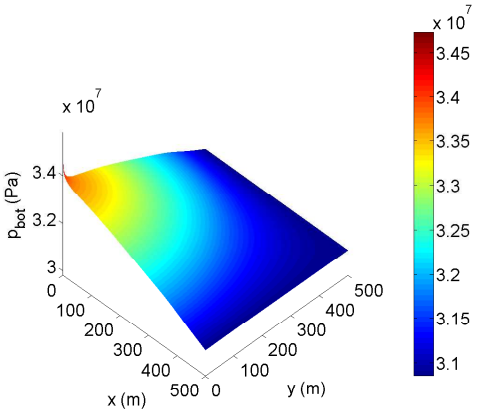

Figure 5.27: Pressure distribution after 325 *days* of CO_2 injection, $Cr = 100$, using 300×300 bilinear elements [5].

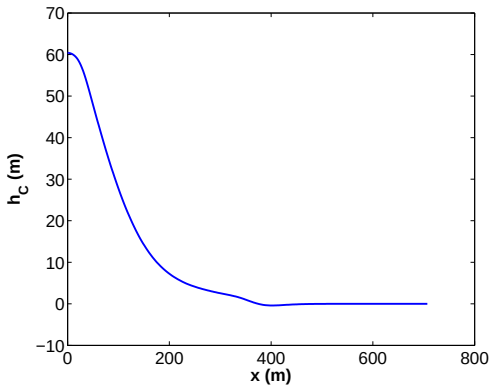

Figure 5.28: Saturation distribution along section A-A (Figure 5.25) after 325 *days* of CO_2 injection, $Cr = 100$, using 300 $\times$ 300 bilinear elements [5].

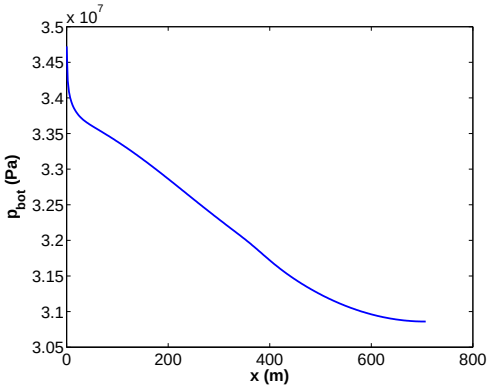

Figure 5.29: Pressure distribution along section A-A (Figure 5.25) after 325 *days* of CO_2 injection, $Cr = 100$, using 300 $\times$ 300 bilinear elements [5].

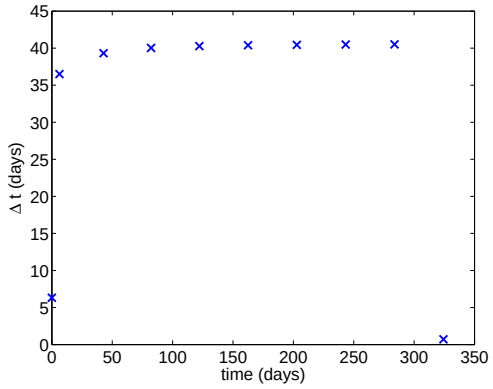

Figure 5.30: Adaptive timestep size over the duration of the simulation, $Cr = 100$, using 90,000 uniform sized bilinear elements [5].

5.6 Chapter Conclusions

Based on the evaluation and comparision of the various stabilization methods in one dimension (quasi-two dimensions), SU-8τ was found to be the most robust in terms of stability, especially at large timesteps (Chapter 4). This formulation (SU-8τ) was extended to bilinear two dimensional elements (quasi-three dimensions) in the current chapter. Objective 3 (see Chapter 1) of this thesis has been accomplished in this chapter by comparing the SU-8τ formulation to a benchmark study that computes when the CO_2 plume arrives

at a leaky well 100 m away from the injection well. The results fell in the range of solutions from the various simulators examined in [8]. The results agreed very well with numerical (FDM) - analytical discretization that was based on similar assumptions to the formulation presented here. It was also demonstrated that the current model is able to generate smooth solutions when an abrupt change in permeability is encountered.

An example with five injections wells in close range was used to illustrate that the formulation can handle complicated injection scenarios. The long term upslope migration was studied using the given formulation and it was shown that the proposed formulation is able to adequately capture the updip movement of CO_2 due to the buoyant drive that results from the density difference between the brine and the supercritical CO_2. Finally, an example of injection into a dome structure was considered. The current formulation was shown to capture the effect of the injected CO_2 flowing downward despite the buoyancy drive since the CO_2 has nowhere else to go.

The model presented in this thesis could be further validated using data from current carbon sequestration operations. A detailed comparison with the North Sea project (Sleipner) is not practical at this point due to the lack of data and large amount of heterogeneities in the system [93]. The Ketzin injection site is relatively well characterized. Data from the Ketzin project can be used to further validate the model presented in this thesis [94, 95].

Computationally efficiency of the underlying numerical solver is essential for practical value in stochastic simulations. In this chapter the use of a vertically averaged multiphase flow framework based upon sequentially coupled FEMs was examined. The computational costs were reduced for the models from Chapter 4 in the current chapter via an adaptive timestep. Objective 4 (see Chapter 1) of this thesis has been accomplished in this chapter

by an adaptive timestepping scheme that allows larger timesteps as the simulation progresses. In the examples considered in this chapter the adaptive timesteps reduced the computational costs of the simulations by a range of approximately 75-82 %.

Chapter 6

Computationally Efficient Approximation of Pressure Singularity at Injection Wells with the eXtended Finite Element Method (XFEM)

This chapter is based on the following journal article:

C. Ladubec, R. Gracie, and J. Craig, "An eXtended Finite Element Method model for carbon sequestration", International Journal for Numerical Methods in Engineering, vol. 102, no. 3-4, pp. 316-331, 2015.

In this article I was the first author where I lead the writing of the journal article. In addition, I lead the development of the MATLAB code, and was involved in the development of the formulation.

This Chapter addresses objective 5 (see Chapter 1) of the thesis:

- Improve the approximation of the pressure singularity due to the injection of CO_2.

6.1 Introduction

Traditional numerical techniques such as the Finite Element Method (FEM) are computationally inefficient when used to model carbon sequestration systems. Aquifers that are candidates for carbon sequestration are often punctured by many abandoned oil and gas wells. The large difference between the scale of aquifers (km^2) and the wells (cm^2) means that in order to obtain accurate solutions a very large number of degrees of freedom are required in simulations. A large number of abandoned wells makes the FEM prohibitively expensive for use in a risk analysis framework.

One method to overcome some of the limitations associated with numerical solutions is to use the eXtended Finite Element Method (XFEM), which was developed to model crack propagation [55, 56]. The primary benefit of XFEM is that it is able to handle discontinuities or steep gradients in the solution in a very computationally efficient manner by enriching the basis functions from the standard FEM. When XFEM is applied to carbon sequestration a fine mesh around the wells is not required to obtain accurate solutions. Instead, the enrichment functions are used only in the vicinity of abandoned wells and injection wells.

In this chapter, an eXtended Finite Element Method (XFEM) method for accurate and efficient modeling of the pressure field resulting from injecting CO_2 into a deep saline aquifer using a vertically averaged multiphase flow formulation is presented. XFEM is then coupled to a Streamline Upwind/ Finite Element Method/Finite Difference Method (SU-FEM-FDM) to model the evolution of the average saturation of each phase in the aquifer. This chapter follows earlier works on XFEM-based single phase aquifer flow models [45, 46].

6.2 Introduction to the eXtended Finite Element Method (XFEM)

The XFEM was comprehensively developed by Belytschko and co-workers over the past 17 years [55, 56, 96, 97, 98, 99]. It was first applied to the simulation of the singularities and discontinuities found in linear elastic fracture mechanics [55, 56, 100]. Later applications focussed on dynamic crack propagation [101, 102, 103], multiscale analysis [104, 105, 106], and material modelling [107, 108, 109].

Comparably less attention has been given to the application of XFEM to multiphase flow. Some notable exceptions are the two-dimensional two-phase flow works of Chessa and Belytschko [110] and Cheng and Fries [111], the three-dimensional two-phase flow models of Sauerland and Fries [112] and the analysis of partially saturated porous media of Mohammadnejad and Khoei [113]. One of the major differences between these earlier works and that present here, is that they focus on two and three dimensional models, whereas, the present model is quasi-three dimensional, leading to different governing equations, different representation of the interface between fluid phases, and different enrichment functions. Furthermore, the focus here is on the singular behaviour near wells.

XFEM was used to model leakage through abandoned wells for a single phase flow formulation [45, 46] where it was shown that for a given level of accuracy XFEM was approximately 10000 times more computationally efficient than the traditional FEM.

6.3 XFEM Approximation of the Pressure Equation

The solution to the pressure equation (5.6) is known to be singular at the injection well. To better approximate the pressure field, an XFEM approximation is adopted. The key to the XFEM is that the FEM approximation is enriched in the vicinity of the injection

wells with functions that capture the asymptotic behaviour near the well. In contrast, an FEM model would require a fine mesh around the wells in order to obtain accurate solutions. As mentioned, XFEM was previously used to model single phase porous media flow in an aquifer [45, 46]. The governing equation (strong form) is given in Chapter 5 by equation (5.6). The weak form is the same as (5.8).

For the multiphase XFEM model present here, the use of the same enrichment function as [45, 46] is examined. The enrichment function for the pressure near well α is:

$$\psi_\alpha(\mathbf{x}) = \begin{cases} \log(r_\alpha(\mathbf{x})), r_\alpha > r_w \\ \\ \log(r_w), r_\alpha \leq r_w \end{cases} \tag{6.1}$$

where r_α is distance to the centre of the well number, α, and r_w is the radius of the well. The enrichment function is illustrated in Figure 6.2. The distance to the centre of well α is given by

$$r_\alpha(\mathbf{x}) = ||\mathbf{x} - \mathbf{x}_\alpha^{inj}|| \tag{6.2}$$

where $\mathbf{x}_\alpha^{inj}$ are the spatial coordinates of the injection wells. In the range of typical well radii the method is insensitive to r_w.

The XFEM approximation of pressure is given by

$$p^h(\mathbf{x}) = \sum_{I \in \mathcal{N}} N_I(\mathbf{x}) p_I + \sum_{\alpha=1}^{n_{inj}} w_\alpha^b(\mathbf{x}) \psi_\alpha(\mathbf{x}) \sum_{J \in S_\alpha} N_J(\mathbf{x}) \overline{p}_{\alpha J}, \mathbf{x} \in \Omega \tag{6.3}$$

where $\mathcal{N}$ is the set of all nodes, p_I is the pressure at node I, n_{inj} is the number of injection wells, S_α is the set of nodes in the enriched domain of well α (see Figure 6.1), $w_\alpha^b(\mathbf{x})$ is a weighting function that blends the enriched and unenriched parts of the domain ([114], [45]), $\overline{p}_{\alpha J}$ are the enriched degrees of freedom, and $N_I(\mathbf{x})$ are the standard finite element

basis functions.

The pressure approximation can be written in matrix form as:

$$p^h(\mathbf{x}) = \mathbf{N}\mathbf{p_{bot}} + \overline{\mathbf{N}}\overline{\mathbf{p}} \tag{6.4}$$

where $\mathbf{N}$ is the matrix of standard FEM shape functions and $\overline{\mathbf{N}}$ is the matrix of the enriched shape functions. $\mathbf{p_{bot}}$ and $\overline{\mathbf{p}}$ are vectors containing the standard FEM pressure degrees of freedom and the enriched degrees of freedom respectively.

$$\mathbf{p_{bot}}^{\mathsf{T}} = \{p_1, p_2, ..., p_{nn}\} \tag{6.5}$$

$$\overline{\mathbf{p}}^{\mathsf{T}} = \{\overline{p}_1, \overline{p}_2, ..., \overline{p}_{mm}\} \tag{6.6}$$

where nn and mm are the number of nodes in the mesh and the number of enriched nodes, respectively.

The blending weight function is defined as:

$$w^b_\alpha(\mathbf{x}) = \sum_{I \in \mathcal{N}} N_I(\mathbf{x}) w^b_I \tag{6.7}$$

where w^b_I is one for an enriched node within the enrichment radius, r_{enr}, and w^b_I is zero for an enriched node outside the enrichment radius.

The XFEM discretization of the pressure equations are:

$$\mathbf{K}_{aquifer} \begin{Bmatrix} \mathbf{p_{bot}} \\ \\ \overline{\mathbf{p}} \end{Bmatrix} = \begin{Bmatrix} \mathbf{F_p} \\ \\ \overline{\mathbf{F}}_\mathbf{p} \end{Bmatrix} \tag{6.8}$$

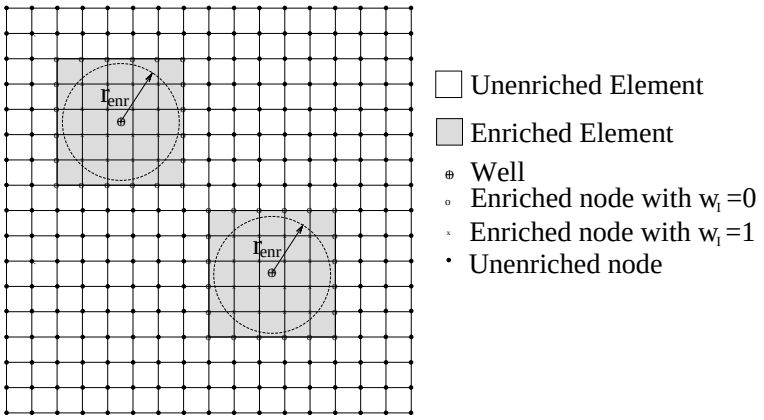

Figure 6.1: Enriched domain. $\mathcal{S}_\alpha$ is the set of nodes within the enrichment radius of well α [7].

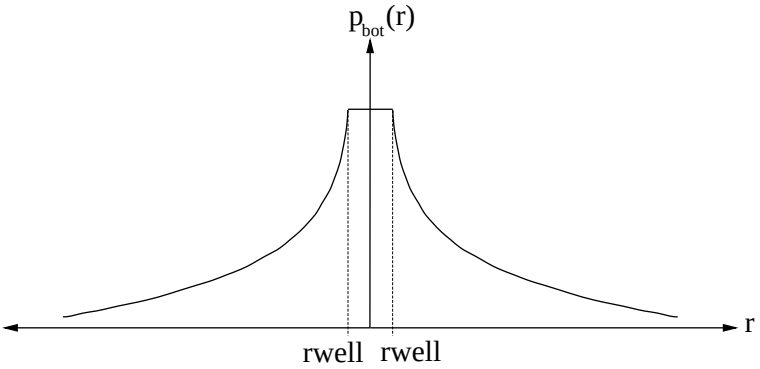

Figure 6.2: Illustration of the enrichment function [7].

$$\mathbf{F_p} = \mathbf{F_{p1}} + \mathbf{F_{p2}} + \mathbf{F_{p3}} + \mathbf{F_{p4}} \tag{6.9}$$

$$\overline{\mathbf{F}}_\mathbf{p} = \overline{\mathbf{F}}_\mathbf{p1} + \overline{\mathbf{F}}_\mathbf{p2} + \overline{\mathbf{F}}_\mathbf{p3} + \overline{\mathbf{F}}_\mathbf{p4} \tag{6.10}$$

$$\mathbf{K}_{aquifer} = \begin{bmatrix} \mathbf{K} & \overline{\mathbf{K}} \\ \overline{\mathbf{K}}^\mathsf{T} & \overline{\overline{\mathbf{K}}} \end{bmatrix} \tag{6.11}$$

where $\mathbf{K_p}$ is the stiffness matrix, $\mathbf{F_{p1}}$ is the injection vector, $\mathbf{F_{p2}}$ is the boundary flux vector, $\mathbf{F_{p3}}$ is the buoyancy vector, and $\mathbf{F_{p4}}$ is the aquifer slope vector. $\overline{\mathbf{K}}_\mathbf{p}$ and $\overline{\overline{\mathbf{K}}}_\mathbf{p}$ are enriched stiffness matrices, $\overline{\mathbf{F}}_\mathbf{p1}$ is the enriched injection vector, $\overline{\mathbf{F}}_\mathbf{p2}$ is the enriched boundary flux vector, $\overline{\mathbf{F}}_\mathbf{p3}$ is the enriched buoyancy vector, and $\overline{\mathbf{F}}_\mathbf{p4}$ is the enriched aquifer

slope vector.

The matrices and vectors are

$$K_{p,IJ} = \int_{\Omega} \mathbf{B}_I^{\mathsf{T}} \left(\frac{hk_{REL,C}}{\mu_C} + \frac{H-h}{\mu_B} \right) \mathbf{k}\mathbf{B}_J d\Omega, \forall I, J \in \mathcal{N} \tag{6.12}$$

$$\overline{K}_{p,IJ} = \int_{\Omega} \overline{\mathbf{B}}_I^{\mathsf{T}} \left(\frac{hk_{REL,C}}{\mu_C} + \frac{H-h}{\mu_B} \right) \mathbf{k}\mathbf{B}_J d\Omega, \forall I \in \mathcal{N}, \forall J \in \mathcal{S}_\alpha \tag{6.13}$$

$$\overline{\overline{K}}_{p,IJ} = \int_{\Omega} \overline{\mathbf{B}}_I^{\mathsf{T}} \left(\frac{hk_{REL,C}}{\mu_C} + \frac{H-h}{\mu_B} \right) \mathbf{k}\overline{\mathbf{B}}_J d\Omega, \forall I \in S_\alpha, \forall J \in \mathcal{S}_\beta \tag{6.14}$$

$$F_{p1,I} = \int_{\Omega} \mathbf{N}_I^{\mathsf{T}} q_{C,inj} d\Omega, \forall I \in \mathcal{N} \tag{6.15}$$

$$\overline{F}_{p1,I} = \int_{\Omega} \overline{\mathbf{N}}_I^{\mathsf{T}} q_{C,inj} d\Omega, \forall I \in \mathcal{S}_\alpha \tag{6.16}$$

$$F_{p2,I} = -\oint_{\Gamma} \mathbf{N}_I^{\mathsf{T}} (\hat{\mathbf{q}}_{\mathbf{B}} + \hat{\mathbf{q}}_{\mathbf{C}}) \mathbf{n} d\Gamma, \forall I \in \mathcal{N} \tag{6.17}$$

$$\overline{F}_{p2,I} = -\oint_{\Gamma} \overline{\mathbf{N}}_I^{\mathsf{T}} (\hat{\mathbf{q}}_{\mathbf{B}} + \hat{\mathbf{q}}_{\mathbf{C}}) \mathbf{n} d\Gamma, \forall I \in \mathcal{S}_\alpha \tag{6.18}$$

$$F_{p3,I} = -\int_{\Omega} \mathbf{B}_I^{\mathsf{T}} \frac{\mathbf{k}k_{rel,C}}{\mu_C} \Delta\rho g h \nabla h d\Omega, \forall I \in \mathcal{N} \tag{6.19}$$

$$\overline{F}_{p3,I} = -\int_{\Omega} \overline{\mathbf{B}}_I^{\mathsf{T}} \frac{\mathbf{k}k_{rel,C}}{\mu_C} \Delta\rho g h \nabla h d\Omega, \forall I \in \mathcal{S}_\alpha \tag{6.20}$$

$$F_{p4,I} = \int_{\Omega} \mathbf{B}_I^{\mathsf{T}} (h \frac{\mathbf{k}k_{rel,C}}{\mu_C} (\rho_B g \nabla H - \rho_C g \nabla z_{top}) - (H-h) \frac{\mathbf{k}}{\mu_B} \rho_B g \nabla z_{bot}) d\Omega, \forall I \in \mathcal{N} \tag{6.21}$$

$$\overline{F}_{p4,I} = \int_{\Omega} \overline{\mathbf{B}}_I^{\mathsf{T}} (h \frac{\mathbf{k}k_{rel,C}}{\mu_C} (\rho_B g \nabla H - \rho_C g \nabla z_{top}) - (H-h) \frac{\mathbf{k}}{\mu_B} \rho_B g \nabla z_{bot}) d\Omega, \forall I \in \mathcal{S}_\alpha \tag{6.22}$$

where $\mathbf{B}$ and $\overline{\mathbf{B}}$ are matrices of the derivatives of the standard and enriched shape functions, respectively.

Numerical Integration

Numerical integration of the unenriched elements in the pressure equation is performed using 2×2 Gauss quadrature. Enriched elements that do not contain a well are integrated using 4×4 Gauss quadrature. Enriched elements containing wells are integrated using an iterative bisection scheme as described in [45]. The subcells are then integrated using 3×3 Gauss quadrature if they are located outside the well radius, and using 1×1 Gauss quadrature if they are located within the well radius. The number of subcells was determined so that the integration errors are sufficiently small to not affect the results.

6.4 Streamline Upwind (SU) Stabilized FEM discretization of the Saturation Equation

The strong form is given by (5.18) and the weak form is given by (5.22) from Chapter 5. An SU-FEM-FDM approximation is used to discretize the saturation equation. Space is discretized using an SU-FEM approach. SU is implemented as an added artificial diffusion term that counteracts the negative diffusion that occurs due to the Galerkin FEM discretization of the hyperbolic saturation equation (i.e., the advection equation). A Crank-Nicolson FDM is used to discretize the time domain.

The average saturation of the brine is approximated in space by:

$$h^h(\mathbf{x}, t) = \sum_{I \in \mathcal{N}} N_I(\mathbf{x}) h_I(t) \tag{6.23}$$

The semi-discrete FEM saturation equations are given by:

$$[\mathbf{C_s}]\{\dot{\mathbf{h_B}}\} + [\mathbf{K_s}]\{\mathbf{h_B}\} = \{\mathbf{F_s}\} \tag{6.24}$$

$$\mathbf{C}_s^e = \int_{\Omega^e} \mathbf{N^{e\mathsf{T}}} \phi (1 - S_{RES,B}) \mathbf{N^e} d\Omega^e \tag{6.25}$$

$$\mathbf{K}_{adv}^e = \int_{\Omega^e} \mathbf{B^{e\mathsf{T}}} \frac{\mathbf{k}}{\mu_B} (\nabla p_{bot} + \rho_B g \nabla z_{bot}) \mathbf{N^e} d\Omega^e \tag{6.26}$$

$$\mathbf{F}_{s^e} = \oint_{\Gamma_q^e} \mathbf{N^{e\mathsf{T}}} \hat{\mathbf{q}}_\mathbf{B} \mathbf{n} d\Gamma_q^e \tag{6.27}$$

where $\{\mathbf{h_B}\}$ is the unknown vector of brine depth in the aquifer and $h_B(\mathbf{x}, t) = H(\mathbf{x}) - h(\mathbf{x}, t)$, $\mathbf{C}_s$ is the storage matrix, $\mathbf{K}_{adv}$ is the advection matrix , $\mathbf{F}_s$ is the boundary flux vector. $\mathbf{N^e}$ are the shape functions for each element and $\mathbf{B^e}$ are the derivatives of the shape functions. The XFEM pressure approximation is utilized in the advection matrix, $\mathbf{K}_{adv}$ above. The Streamline Upwind (SU) method is used to stabilize the saturation equation, which is a pure advection equation. SU is implemented using artificial diffusion as described in [73] and [86]. Artificial diffusion acts to offset the negative diffusion that is created due to the Galerkin FEM approach. The artificial diffusion to the system, which for the pure advection case simplifies to

$$\mathbf{K}_{SU}^e = \int_{\Omega^e} \mathbf{B^{e\mathsf{T}}} \tau \frac{H}{\phi(1 - S_{res,B})} \frac{\mathbf{k}}{\mu_B} |\nabla p_{bot} + \rho_B g \nabla z_{bot}| \mathbf{B^e d\Omega^e} \tag{6.28}$$

where τ is a parameter to control the amount of diffusion applied and is meant to replace the constant multiplier of $\frac{1}{\sqrt{(15)}}$ that was used in [73]. The amount of artificial diffusion is element dependent since it is a function of the pressure gradient in each cell. This approach in not consistent with respect to the transient term and the boundary flux

vector, therefore τ must be selected carefully to avoid overly diffuse solutions [73]. An improved stabilization approach for this formulation is described in Chapter 5.

In the saturation equation, time is discretized using the FDM. This can be written as

$$\begin{aligned}&([\mathbf{C_s}] + \Delta t\theta[\mathbf{K_s}]^{n+1})\{\mathbf{h_B}\}^{n+1} = \\ &(([\mathbf{C_s}] - \Delta t(1-\theta)[\mathbf{K_s}]^{n})\{\mathbf{h_B}\}^{n} + \Delta t(\theta\{\mathbf{F_s}\}^{n+1} + (1-\theta)\{\mathbf{F_s}\}^{n}))\end{aligned} \tag{6.29}$$

where $[\mathbf{K_s}] = [\mathbf{K}_{adv}] + [\mathbf{K}_{SU}]$. In the above equation, $\theta = 0.5$ gives the Crank-Nicolson (CN) method.

6.5 Example 1 - Injection of CO_2 into a Deep Saline Aquifer

In this example CO_2 is injected into a brine filled aquifer. The setup of this problem is shown in Figure 6.3. The system properties are given in Table 6.1. The aquifer is bounded above and below by impermeable caprock layers (aquicludes). Initially, the aquifer is filled with brine. The water table begins at the top boundary of the aquifer. CO_2 is injected at a constant rate of 1600 m^3/day. As the injection progresses, the CO_2 plume spreads throughout the aquifer.

Dirichlet boundary conditions of hydrostatic pressure are applied for the pressure equation along the whole boundary of the domain. An initial condition of $h(\mathbf{x}, 0) = 0$ throughout the domain is used (i.e. brine only). Dirichlet boundary conditions of $h(\mathbf{x}, t) = 0$ are imposed at all boundaries, and as such the domain must be large enough so that the CO_2 plume remains far enough away from the domain boundaries. The simulation is conducted for a time of 3 *days*.

Figure 6.4 compares the pressures distributions for two XFEM and two FEM simu-

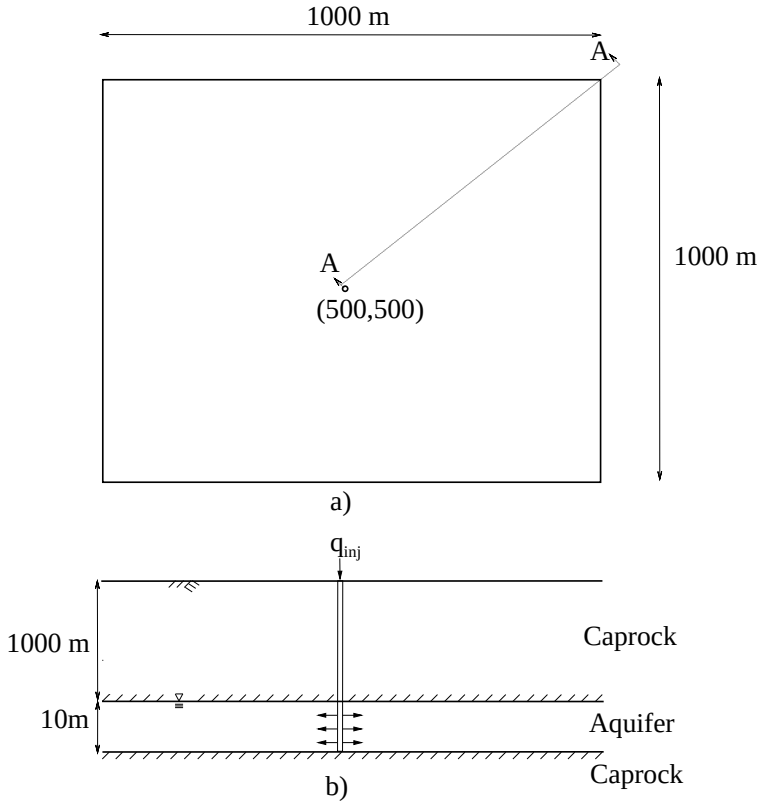

Figure 6.3: Set up of example 1 [7].

lations with different mesh densities. The pressure is plotted against a radius centered at the centre of the well along section A-A, as shown in Figure 6.3. Near the injection well the XFEM solutions give higher localized pressures. The pressure near the injection well increases along with refinement of the FEM and XFEM meshes. At further distances away from the well XFEM and FEM give similar pressure fields. Figure 6.5 shows the average CO_2 saturation distribution along a radius that follows section A-A (Figure 6.3). The XFEM and FEM pressure approximations give similar results. The depth of CO_2 at the injection well converges to the depth of the aquifer as element size is reduced.

A study of the relative error in the pressure at the well is shown in Figure 6.6. The relative error is obtained by comparison to the pressure at the well using a fine FEM mesh (3.6×10^5 elements) with the injection at a node. This compares to a maximum of 2.3×10^4 elements used in the study. For the coarsest meshes the FEM with the injection

Table 6.1: System properties for example 1 [7].

Property	Value	Units
μ_B	5.11e-4	Ns/m^2
μ_C	6.11e-5	Ns/m^2
ρ_B	1099	kg/m^3
ρ_C	400	kg/m^3
$S_{res,B}$	0	-
ϕ	0.15	-
k_x	1e-15	m^2
k_y	1e-15	m^2
$k_{rel,C}$	1	-
q_{inj}	1600	m^3/day
r_w	0.15	m

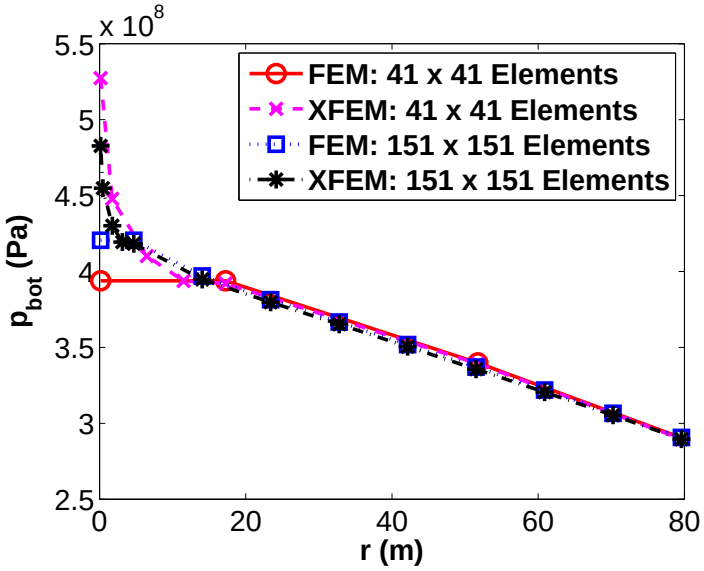

Figure 6.4: Comparison of XFEM and FEM pressure distributions along a radius centered at injection well and along line A-A using bilinear quadrilateral elements [7].

at a node provides the least relative error. This relative error decreases rather slowly. XFEM reaches a 1 % relative error much sooner than both FEM approaches. Therefore to achieve a relative error less than 1 % is computationally more efficient to use XFEM. XFEM can achieve low relative errors even when the injection takes place mid-element. FEM performs poorly when the injection takes place mid-element.

The effect of the amount of stabilization (τ) on the average saturation profile is studied using XFEM in Figure 6.7. At low values of τ the saturation profile is non-physical. The

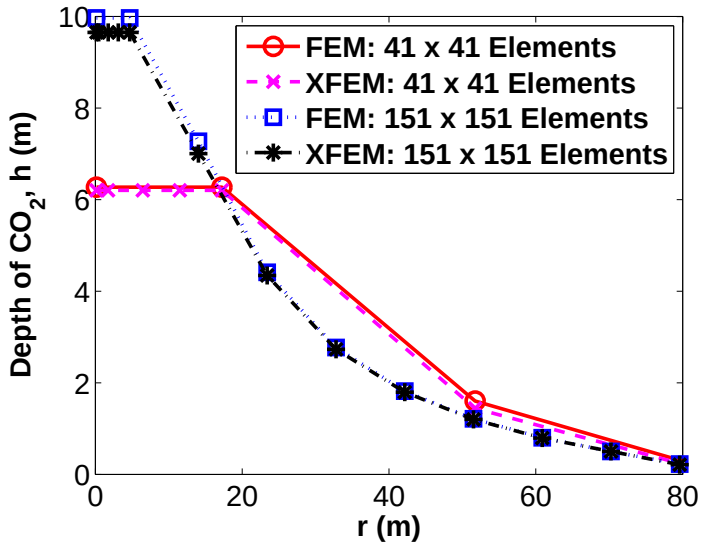

Figure 6.5: Comparison of XFEM and FEM average CO_2 saturation distributions along a radius centered at injection well and along line A-A using bilinear quadrilateral elements [7].

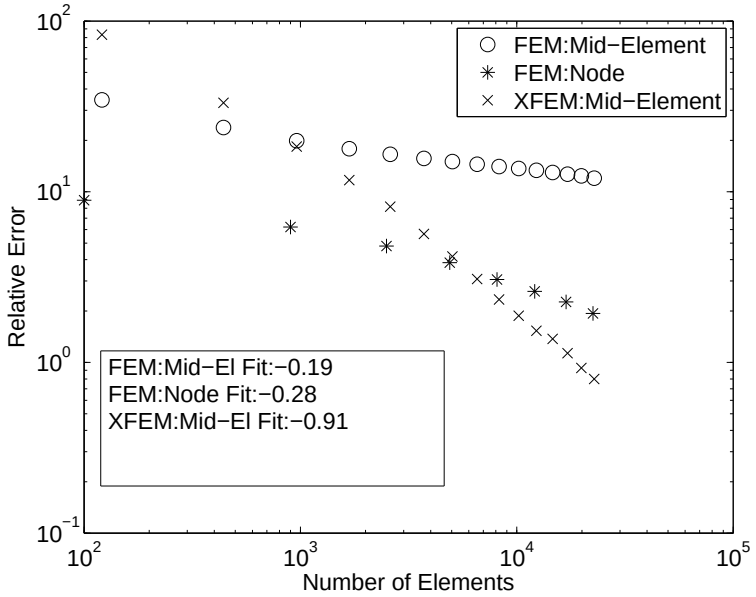

Figure 6.6: Comparison of relative error in pressure at the injection well for XFEM and FEM [7].

approximation becomes smoother as τ is increased. One side effect of increased damping is the reduction of the depth of CO_2 at the injection well. Care must be taken in the selection of τ to avoid overdamping. The effect of τ on the pressure is shown in Figure 6.8. Once τ is large enough to eliminate the non-physical values, increasing τ increases the

pressure near the well, and reduces the pressure further away from the well. Therefore, a careful selection of τ is important. A more detailed consideration of τ can be found in Chapter 4 and Chapter 5.

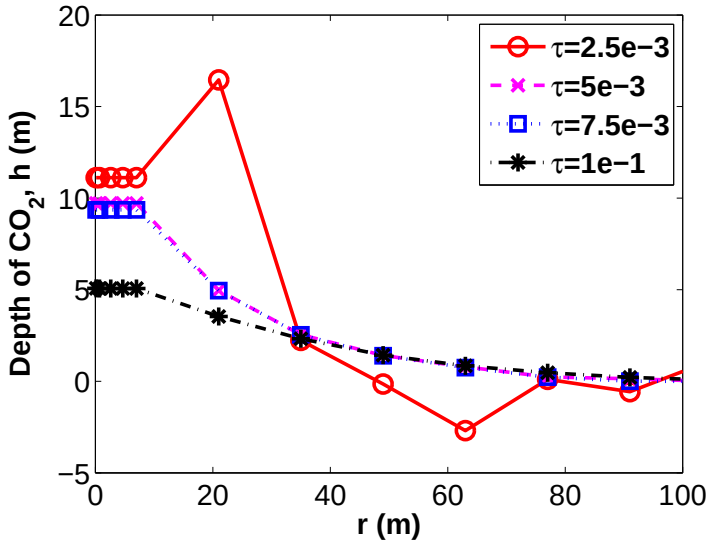

Figure 6.7: Effect of the stabilization parameter on average CO_2 saturation profile along a radius centered at injection well and along line A-A [7].

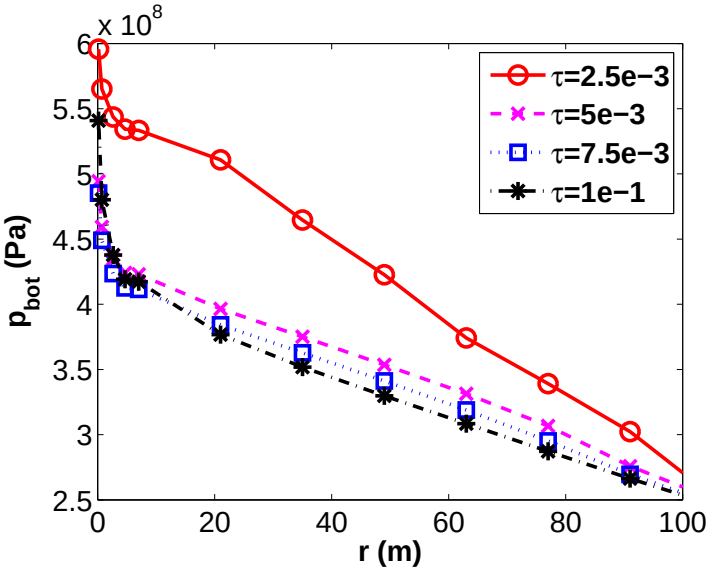

Figure 6.8: Effect of the stabilization parameter on pressure along a radius centered at injection well and along line A-A [7].

6.6 Example 2 - Injection of CO_2 into a Sloping Aquifer

In this example CO_2 is injected into a sloping aquifer. The problem is illustrated in Figure 6.9 and the system properties are described in Table 6.2. The aquifer is bounded above and below by impermeable layers. The top boundary of the aquifer slopes upwards to the right and the bottom boundary slopes downwards to the right. Therefore, the depth of the aquifer is a function of the x and y coordinates.

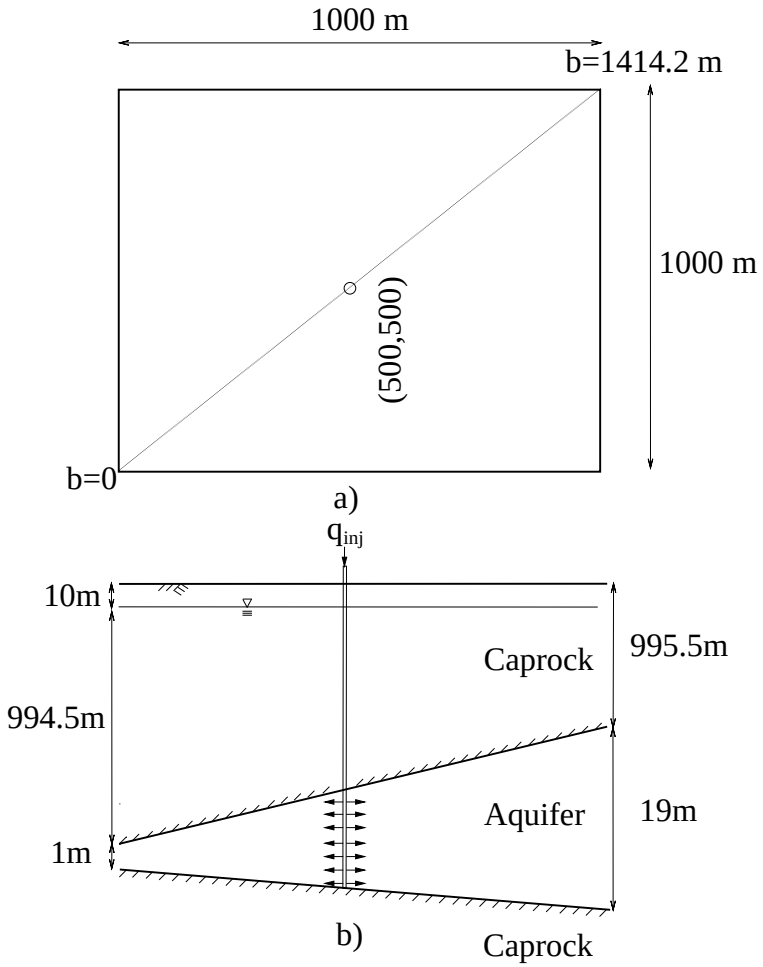

Figure 6.9: Set up of example 2 [7].

Table 6.2: System properties for example 2 [7].

Property	Value	Units
μ_B	5.11e-4	Ns/m^2
μ_C	6.11e-5	Ns/m^2
ρ_B	1099	kg/m^3
ρ_C	400	kg/m^3
$S_{res,B}$	0	-
ϕ	0.15	-
k_x	1e-15	m^2
k_y	1e-15	m^2
$k_{rel,C}$	1	-
q_{inj}	1600	m^3/day
r_w	0.15	m

Dirichlet boundary conditions are specified for the pressure equations as the hydrostatic pressure caused by the brine that exists between the top of the water table and the bottom of the aquifer. For the saturation equation Dirichlet boundary conditions are specified such that at the boundaries of the domain the full depth of the aquifer is filled with brine. Initial conditions of a completely brine-filled aquifer are applied.

The average CO_2 saturation profile is shown in Figure 6.10. Since the CO_2 has a lower density than the host brine fluid, the CO_2 should preferentially flow to the right, following the up-sloping top boundary of the aquifer.

Figure 6.10 shows the average saturation after 60 *days* of injection for the system shown in Figure 6.9 compared to the system shown in Figure 6.3. The average saturation is shown along axis b, defined in Figure 6.9. Comparing the evolution of the CO_2 plume in the horizontal aquifer case and the sloping aquifer one can see that the for the sloping aquifer, the CO_2 preferentially flows up the slope. This preferential flow is caused by the buoyant drive resulting from the lower density of the CO_2 compared to brine. Thus the current formulation adequately captures the updip effect of CO_2 migration.

Figure 6.11 shows the pressure distribution along along axis b, defined in Figure 6.9 after 60 *days* of injection. The pressure to the left of the well is larger than to the right of

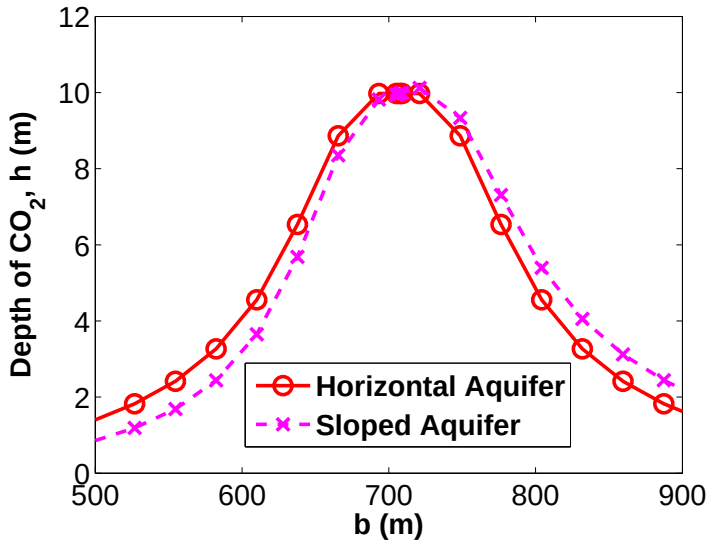

Figure 6.10: XFEM average CO_2 saturation distribution after 60 *days* of injection [7].

the well due to the sloping aquifer. The larger pressure on the left drives the flow updip to the right. During the early stages of injection the saturation of CO_2 is significantly impacted by the sloping aquifer geometry due to buoyancy forces.

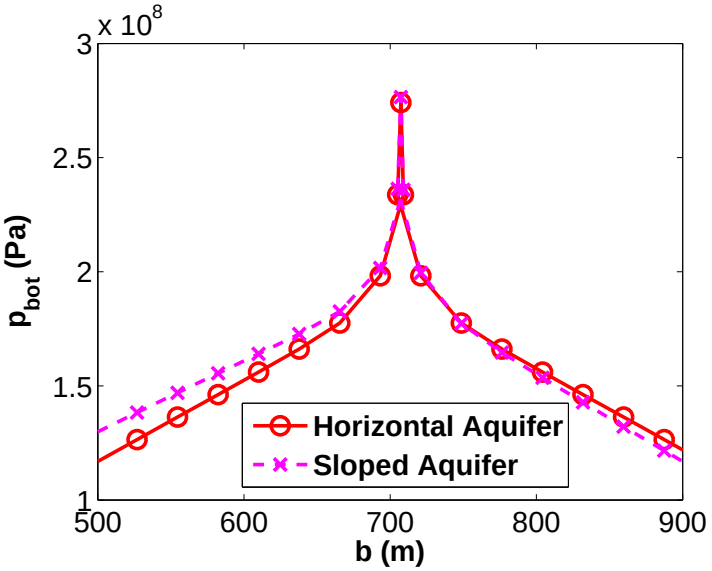

Figure 6.11: XFEM pressure distribution after 60 *days* of injection [7].

6.7 Chapter Conclusions

A computationally efficient model of carbon sequestration, where carbon dioxide (CO_2) is injected into deep saline aquifers is presented. Objective 5 (see Chapter 1) of this thesis has been accomplished in this chapter by an effective computational scheme that combines the efficiency of a vertically averaged formulation and the enrichment of the pressure approximation using the eXtended Finite Element Method (XFEM). The XFEM-based formulation is used to improve the approximation of the singular pressure field in the vicinity of an injection well. The XFEM pressure approximation is combined with a Streamline Upwind/Finite Element Method/Finite Difference Method (SU-FEM-FDM) framework to approximates the average CO_2 saturation through the thickness of the aquifer. Using the XFEM-SU-FEM-FDM framework two examples were considered. In the first, it was shown that XFEM is able to achieve low relative errors in the pressure near injection wells at a lower computational cost, when compared to an FEM approximation. The SU stabilization parameter, τ must be selected carefully to avoid over diffuse saturation distributions. In the second example, the XFEM-SU-FEM-FD simulator is demonstrated to be able to capture the important effect of buoyancy driven flow of CO_2 in a sloping aquifer.

Chapter 7

Conclusions

Carbon sequestration is a means to reduce CO_2 emissions by injecting CO_2 into deep saline aquifers for permanent storage. Due to a great deal of uncertainty involved in these systems, computationally efficient numerical methods are needed for stochastic simulations. In this thesis a framework for a computationally efficient numerical method to study the large scale plume evolution associated with carbon sequestration was presented.

In Chapter 1 an introduction to carbon sequestration was given. Carbon Capture and Storage (CCS) was described as a means to reduce greenhouse gas emissions from point emitters of CO_2, such as coal fired power plants. Carbon sequestration, which is the storage phase of CCS was then introduced. Deep saline aquifers were mentioned as a particularly promising storage location. Solution approaches applicable to carbon sequestration systems were discussed. Challenges related to numerical modelling of carbon sequestrations were provided as a motivation to the objectives of the thesis, which were presented at the end of Chapter 1.

Chapter 2 provided an introduction to the numerical modelling of flow in porous media. Basic definitions and governing equations were explained for single phase flow and

multiphase flow. The governing equations that are the focus of this thesis were provided towards the end of this chapter.

Chapter 3 examined the use of stabilized FEMs for advection-reaction equations. These equations can result in non-physical spurious oscillations when discretized using the Galerkin FEM. Five stabilized FEMs were introduced and applied to four variations of the advection-reaction equation in order to gain insight in how the stabilized FEMs behaved in uncoupled advection-reaction equations. The stabilized FEMs that were considered were SU, SUPG, LSFEM, SGS, and GLS. The examples demonstrate that Galerkin approximations of an advection-reaction equation can have small scale oscillations that do not occur with the stabilized FEMs. In certain cases the oscillations can introduce instabilities in the approximations. This is particularly true for the Galerkin FEM, however instabilities can also occur when using the stabilized FEMs. Care must be taken to select the proper stabilization method in order to achieve acceptable approximations to any problem.

In Chapter 4 five different stabilized FEMs (SU, SUPG, LSFEM, SGS, and GLS) are used to discretize the governing equations of vertically averaged multiphase flow and compared with the Galerkin FEM discretization. Three examples were used to compare several solution strategies for the saturation equation using linear one-dimensional elements. First order convergence of the saturation error with respect to the L_2 norm was achieved for both the SS (Single-Step) and PC (Predictor-Corrector) solution strategies using Backward Euler (BE) time integration. It was demonstrated that, in general, a fully implicit Backward Euler (BE) time integration scheme provides superior stability properties compared to the Forward Euler (FE) and Crank-Nicholson (CN) time integration methods.

In general, when FE ($\theta = 0$) or CN ($\theta = 0.5$) time integration is used, small Courant numbers (e.g., $Cr_{max} \leq 0.005$) are required to obtain smooth solutions with the various stabilization methods.

BE ($\theta = 1$) provides the most reliable approximations in general. In addition to being stable and non-oscillatory for small timesteps, for large timesteps ($Cr_{max} \geq 3 - 5$) it can also produce smooth solutions depending on the sequential solution strategy and stabilization method. When the CO_2 plume encounters the Dirichlet domain boundaries oscillations can contaminate the brine saturation solution. In addition, oscillations can occur when two plumes meet. If SU stabilization is combined with 8τ or 10τ (eight or ten times a standard stabilization parameter definition) smooth solutions can be obtained for large timesteps when the plume encounters a boundary and when plumes merge. No other stabilization scheme gives acceptable solutions using large timesteps when two plumes merge.

A PC scheme can be used to reduce oscillations at large timesteps with the BE method ($\theta = 1$), but comes with a significant increase in computational cost. The SS method gives a similar result as the PC scheme, but at a much lower computational cost.

Care that must be taken when using Dirichlet boundaries on the outflow boundaries or the simulation of multiple merging CO_2 plumes. It was demonstrated that a Galerkin FEM discretization of the saturation equation should not be used if the CO_2 plume encounters a Dirichlet boundary or if multiple injection wells are present and large timesteps are used. SU combined with an increased value of the stabilization parameter (8τ or 10τ) is the most robust stabilization method examined. When combined with BE time integration it can achieve smooth solutions at large timesteps, and gives reasonable results even with a simple SS sequential solution strategy, which yields a computationally effi-

cient framework to solve the vertically averaged multiphase flow equations presented in this work.

The SU-8τ approximation did not change significantly when quadratic elements were used. At large timesteps SU-8τ best matches the solutions obtained by all methods at the smallest Cr. It is hypothesized that the increased stabilization parameter provides sufficient artificial diffusion to compensate for the negative diffusion introduced by the Galerkin FEM approximation of the saturation equation.

Linear elements cannot fully represent the stabilization terms for SUPG and LSFEM. Quadratic elements allow the full stabilization terms of SUPG and LSFEM to be represented. SUPG and LSFEM approximations were more diffuse with quadratic elements. Quadratic elements were shown improve the stabilization properties of SUPG and LSFEM in some cases. Furthermore, quadratic elements permit the use of SGS and GLS. Two examples were provided that examine stabilization with higher order (quadratic) elements.

SGS and GLS offer stable approximations over a larger range of timesteps compared to Galerkin, SU, SUPG, and LSFEM. SGS and GLS can provide smooth oscillation-free approximations for small Courant numbers ($Cr \leq 0.05$) and large Courant numbers ($Cr \geq 3$). SU-8τ provides smooth solutions when $Cr \geq 0.05$. SGS and GLS seem to be the preferable option for small Cr values, while SU-8τ seems to be the best option for large Cr values.

In general, quadratic elements improve the ability of the stabilized FEMs to achieve smooth solutions compared with linear elements when multiple CO_2 plumes merge. However, quadratic elements introduce a greater tendency (compared to linear elements) for oscillations when the CO_2 exits the domain.

SU-8τ was in general found to exhibit the best stabilization properties over the range of conditions examined using the one dimensional (linear and quadratic) studies. At large timesteps the advantages of SU-8τ are the most apparent.

In Chapter 5 the SU-8τ formulation was compared to a benchmark study that simulates the arrival of a CO_2 plume at a leaky well 100 m away from the injection well. The results fell in the range of solutions from the various simulators examined in [8]. The results agreed very well with numerical (FDM) - analytical discretization that was based on similar assumptions to the formulation presented here. It was also demonstrated that the current model is able to generate smooth solutions when an abrupt change in permeability is encountered.

An example with five injection wells in close range was used to illustrate that the formulation can handle complicated injection scenarios. The long term upslope migration was studied using the given formulation and it was shown that the proposed formulation is able to adequately capture the updip movement of CO_2 due to the buoyant drive that results from the density difference between the brine and the supercritical CO_2. Finally an example of injection into a dome structure was considered. The current formulation was shown to capture the effect of the injected CO_2 flowing downward despite the buoyancy drive since the CO_2 has nowhere else to go.

Computationally efficiency of the underlying numerical solver is essential for practical value in stochastic simulations. The current formulation improves the computational efficiency from Chapter 4 by an adaptive timestepping scheme that allows larger timesteps as the simulation progresses. In the examples considered in this chapter the adaptive timesteps reduced the computational cost of the simulations by a range of approximately 75-82 %.

In Chapter 6 the eXtended Finite Element Method (XFEM) was used to improve the approximation of the singular pressure field that occurs at an injection well. An effective computational scheme is obtained by combining the efficiency of a vertically averaged formulation and the enrichment of the pressure approximation using XFEM. The XFEM pressure approximation is combined with a Streamline Upwind/Finite Element Method/Finite Difference Method (SU-FEM-FDM) framework to approximate the average CO_2 saturation through the thickness of the aquifer. Using the XFEM-SU-FEM-FDM framework two examples were examined. In the first, it was shown that XFEM is able to achieve low relative errors in the pressure near injection wells at a lower computational cost, when compared to an FEM approximation. The SU stabilization parameter, τ must be selected carefully to avoid over diffuse saturation distributions. In the second example, the XFEM-SU-FEM-FD simulator is demonstrated to be able to capture the important effect of buoyancy driven flow of CO_2 in a sloping aquifer.

Chapter 8

Future Work

In this chapter several recommendations are given for future work related to extending the formulations provided in this thesis:

- Further validation of numerical models using field data (e.g., Ketzin);
- Fully coupled solutions, as an alternative to the sequentially coupled solution strategy presented in this thesis, should be considered as they may have different stabilization properties;
- Solution of CO_2 equation as saturation equation, instead of the brine equation;
- XFEM implementation of leaky wells and multi-aquifer systems for multiphase flow as in [45, 46];
- Brine may be extracted to reduced pressure as CO_2 is injected, therefore in the formulation a brine extraction source term could be considered;
- Determination or proof of correct approximation spaces for pressure and saturation equations;

- Alternative approaches for stabilized approximations (e.g., the Discontinuous Galerkin (DG) method or the Finite Volume Method (FVM)) of the saturation equations should be explored.

Copyright Permissions

JOHN WILEY AND SONS LICENSE TERMS AND CONDITIONS

Apr 11, 2016

This Agreement between Chris Ladubec ("You") and John Wiley and Sons ("John Wiley and Sons") consists of your license details and the terms and conditions provided by John Wiley and Sons and Copyright Clearance Center.

License Number	3846151307571
License date	Apr 11, 2016
Licensed Content Publisher	John Wiley and Sons
Licensed Content Publication	International Journal for Numerical Methods in Engineering
Licensed Content Title	An extended finite element method model for carbon sequestration
Licensed Content Author	Chris Ladubec,Robert Gracie,James Craig
Licensed Content Date	Jul 24, 2014
Pages	16
Type of use	Dissertation/Thesis
Requestor type	Author of this Wiley article
Format	Print and electronic
Portion	Full article
Will you be translating?	No
Title of your thesis / dissertation	Computationally Efficient Extended and Stabilized Finite Element Methods for Multiphase Carbon Sequestration Modelling
Expected completion date	Jun 2016
Expected size (number of pages)	200
Requestor Location	Chris Ladubec University of Waterloo 200 University Ave W Waterloo, ON N2L 3G1 Canada Attn: Chris Ladubec
Billing Type	Invoice
Billing Address	Chris Ladubec University of Waterloo 200 University Ave W Waterloo, ON N2L 3G1 Canada Attn: Chris Ladubec
Total	0.00 USD
Terms and Conditions	

TERMS AND CONDITIONS

and the right to reproduce the Wiley Materials pursuant to Section 2 herein during the continuance of this Agreement. You agree that you own no right, title or interest in or to the Wiley Materials or any of the intellectual property rights therein. You shall have no rights hereunder other than the license as provided for above in Section 2. No right, license or interest to any trademark, trade name, service mark or other branding ("Marks") of WILEY or its licensors is granted hereunder, and you agree that you shall not assert any such right, license or interest with respect thereto

- NEITHER WILEY NOR ITS LICENSORS MAKES ANY WARRANTY OR REPRESENTATION OF ANY KIND TO YOU OR ANY THIRD PARTY, EXPRESS, IMPLIED OR STATUTORY, WITH RESPECT TO THE MATERIALS OR THE ACCURACY OF ANY INFORMATION CONTAINED IN THE MATERIALS, INCLUDING, WITHOUT LIMITATION, ANY IMPLIED WARRANTY OF MERCHANTABILITY, ACCURACY, SATISFACTORY QUALITY, FITNESS FOR A PARTICULAR PURPOSE, USABILITY, INTEGRATION OR NON-INFRINGEMENT AND ALL SUCH WARRANTIES ARE HEREBY EXCLUDED BY WILEY AND ITS LICENSORS AND WAIVED BY YOU.

- WILEY shall have the right to terminate this Agreement immediately upon breach of this Agreement by you.

- You shall indemnify, defend and hold harmless WILEY, its Licensors and their respective directors, officers, agents and employees, from and against any actual or threatened claims, demands, causes of action or proceedings arising from any breach of this Agreement by you.

- IN NO EVENT SHALL WILEY OR ITS LICENSORS BE LIABLE TO YOU OR ANY OTHER PARTY OR ANY OTHER PERSON OR ENTITY FOR ANY SPECIAL, CONSEQUENTIAL, INCIDENTAL, INDIRECT, EXEMPLARY OR PUNITIVE DAMAGES, HOWEVER CAUSED, ARISING OUT OF OR IN CONNECTION WITH THE DOWNLOADING, PROVISIONING, VIEWING OR USE OF THE MATERIALS REGARDLESS OF THE FORM OF ACTION, WHETHER FOR BREACH OF CONTRACT, BREACH OF WARRANTY, TORT, NEGLIGENCE, INFRINGEMENT OR OTHERWISE (INCLUDING, WITHOUT LIMITATION, DAMAGES BASED ON LOSS OF PROFITS, DATA, FILES, USE, BUSINESS OPPORTUNITY OR CLAIMS OF THIRD PARTIES), AND WHETHER OR NOT THE PARTY HAS BEEN ADVISED OF THE POSSIBILITY OF SUCH DAMAGES. THIS LIMITATION SHALL APPLY NOTWITHSTANDING ANY FAILURE OF ESSENTIAL PURPOSE OF ANY LIMITED REMEDY PROVIDED HEREIN.

- Should any provision of this Agreement be held by a court of competent jurisdiction to be illegal, invalid, or unenforceable, that provision shall be deemed amended to achieve as nearly as possible the same economic effect as the original provision, and the legality, validity and enforceability of the remaining provisions of this Agreement shall not be affected or impaired thereby.

- The failure of either party to enforce any term or condition of this Agreement shall not constitute a waiver of either party's right to enforce each and every term and condition of this Agreement. No breach under this agreement shall be deemed waived or excused by either party unless such waiver or consent is in writing signed by the party granting such waiver or consent. The waiver by or consent of a party to a breach of any provision of this Agreement shall not operate or be construed as a waiver of or consent to any other or subsequent breach by such other party.

- This Agreement may not be assigned (including by operation of law or otherwise) by you without WILEY's prior written consent.

- Any fee required for this permission shall be non-refundable after thirty (30) days from receipt by the CCC.

- These terms and conditions together with CCC's Billing and Payment terms and conditions (which are incorporated herein) form the entire agreement between you and WILEY concerning this licensing transaction and (in the absence of fraud) supersedes all prior agreements and representations of the parties, oral or written. This Agreement may not be amended except in writing signed by both parties. This Agreement shall be binding upon and inure to the benefit of the parties' successors, legal representatives, and authorized assigns.

- In the event of any conflict between your obligations established by these terms and conditions and those established by CCC's Billing and Payment terms and conditions, these terms and conditions shall prevail.

- WILEY expressly reserves all rights not specifically granted in the combination of (i) the license details provided by you and accepted in the course of this licensing transaction, (ii) these terms and conditions and (iii) CCC's Billing and Payment terms and conditions.

- This Agreement will be void if the Type of Use, Format, Circulation, or Requestor Type was misrepresented during the licensing process.

- This Agreement shall be governed by and construed in accordance with the laws of the State of New York, USA, without regards to such state's conflict of law rules. Any legal action, suit or proceeding arising out of or relating to these Terms and Conditions or the breach thereof shall be instituted in a court of competent jurisdiction in New York County in the State of New York in the United States of America and each party hereby consents and submits to the personal jurisdiction of such court, waives any objection to venue in such court and consents to service of process by registered or certified mail, return receipt requested, at the last known address of such party.

WILEY OPEN ACCESS TERMS AND CONDITIONS

Wiley Publishes Open Access Articles in fully Open Access Journals and in Subscription journals offering Online Open. Although most of the fully Open Access journals publish open access articles under the terms of the Creative Commons Attribution (CC BY) License

References

[1] J. Dooley, *Carbon Dioxide Capture Geologic Storage: A Core Element of a Global Energy Technology Strategy to Address Climate Change*. Battelle, Joint Global Change Research Institute, 2006.

[2] B. Metz, *IPCC special report on carbon dioxide capture and storage*. Cambridge University Press, 2005.

[3] M. A. Celia and J. M. Nordbotten, "Practical modeling approaches for geological storage of carbon dioxide," *Ground Water*, vol. 47, no. 5, pp. 627–638, 2009.

[4] C. Ladubec and R. Gracie, "Vertically averaged multiphase flow simulations for carbon sequestration using stabilized finite element methods and quadratic elements," Submitted, 2016.

[5] C. Ladubec and R. Gracie, "Quasi-three dimensional multiphase carbon sequestration simulation with the finite element method," In Preparation.

[6] C. Ladubec and R. Gracie, "Stabilized finite element methods for vertically averaged multiphase flow in carbon sequestration," Submitted, 2015.

[7] C. Ladubec, R. Gracie, and J. Craig, "An extended finite element method model for carbon sequestration," *International Journal for Numerical Methods in Engineering*, vol. 102, no. 3-4, pp. 316–331, 2015.

[8] H. Class, A. Ebigbo, R. Helmig, H. Dahle, J. Nordbotten, M. Celia, P. Audigane, M. Darcis, J. Ennis-King, Y. Fan, B. Flemisch, S. Gasda, M. Jin, S. Krug, D. Labregere, A. Naderi Beni, R. Pawar, A. Sbai, S. Thomas, L. Trenty, and L. Wei, "A benchmark study on problems related to CO_2 storage in geologic formations," *Computational Geosciences*, vol. 13, no. 4, pp. 409–434, 2009.

[9] B. Smit, J. R. Reimer, C. M. Oldenburg, and I. C. Bourg, *Introduction to Carbon Capture and Sequestration*, vol. 1. World Scientific, 2014.

[10] S. Wong and R. Bioletti, "Carbon dioxide separation technologies," *Carbon and Energy Management, Alberta Research Council*, 2002.

[11] J. M. Nordbotten and M. A. Celia, *Geological storage of CO_2: modeling approaches for large-scale simulation.* John Wiley & Sons: Hoboken, NJ, 2011.

[12] S. Bachu, "Sequestration of CO_2 in geological media: criteria and approach for site selection in response to climate change," *Energy Conversion and Management*, vol. 41, no. 9, pp. 953–970, 2000.

[13] M. A. Celia, S. Bachu, J. M. Nordbotten, and K. W. Bandilla, "Status of CO_2 storage in deep saline aquifers with emphasis on modeling approaches and practical simulations," *Water Resources Research*, vol. 51, no. 9, pp. 6846–6892, 2015.

[14] J. T. Birkholzer, C. M. Oldenburg, and Q. Zhou, "CO_2 migration and pressure evolution in deep saline aquifers," *International Journal of Greenhouse Gas Control*, vol. 40, pp. 203–220, 2015.

[15] J. Streit and R. Hillis, "Estimating fault stability and sustainable fluid pressures for underground storage of CO_2 in porous rock," *Energy*, vol. 29, no. 9, pp. 1445–1456, 2004.

[16] J. Rutqvist, J. Birkholzer, F. Cappa, and C. Tsang, "Estimating maximum sustainable injection pressure during geological sequestration of CO_2 using coupled fluid flow and geomechanical fault-slip analysis," *Energy Conversion and Management*, vol. 48, no. 6, pp. 1798–1807, 2007.

[17] J. Nordbotten and M. Celia, "Analysis of plume extent using analytical solutions for CO_2 storage," in *Proceedings of the 16th Conference on Computational Methods in Water Resources*, 2006.

[18] J. Nordbotten and M. Celia, "Similarity solutions for fluid injection into confined aquifers," *Journal of Fluid Mechanics*, vol. 561, pp. 307–327, 2006.

[19] J. Nordbotten, M. Celia, S. Bachu, and H. Dahle, "Semianalytical solution for CO_2 leakage through an abandoned well," *Environmental Science and Technology*, vol. 39, no. 2, pp. 602–611, 2005.

[20] J. Nordbotten, D. Kavetski, M. Celia, and S. Bachu, "A semi-analytical model estimating leakage associated with CO_2 storage in large-scale multi-layered geological systems with multiple leaky wells," *Environmental Science and Technology*, vol. 43, no. 3, pp. 743–749, 2009.

[21] S. Silliman and D. Higgins, "An analytical solution for steady-state flow between aquifers through an open well," *Ground Water*, vol. 28, no. 2, pp. 184–190, 1990.

[22] C. Avci, "Flow occurrence between confined aquifers through improperly plugged boreholes," *Journal of Hydrology*, vol. 139, no. 1, pp. 97–114, 1992.

[23] I. Javandel, C. Tsang, P. Witherspoon, and D. Morganwalp, "Hydrologic detection of abandoned wells near proposed injection wells for hazardous waste disposal," *Water Resources Research*, vol. 24, no. 2, pp. 261–270, 1988.

[24] T. Brikowski, "Flow between aquifers through filled cylindrical conduits: analytical solution and application to underground nuclear testing sites," *Journal of Hydrology*, vol. 146, pp. 115–130, 1993.

[25] C. Avci, "Evaluation of flow leakage through abandoned wells and boreholes," *Water Resources Research*, vol. 30, no. 9, pp. 2565–2578, 1994.

[26] J. M. Nordbotten, M. A. Celia, and S. Bachu, "Analytical solutions for leakage rates through abandoned wells," vol. 40,W04204, 2004.

[27] J. Nordbotten, M. Celia, and S. Bachu, "Injection and storage of CO_2 in deep saline aquifers: Analytical solution for CO_2 plume evolution during injection," *Transport in Porous Media*, vol. 58, no. 3, pp. 339–360, 2005.

[28] C. MacMinn, "Analytical modeling of CO_2 migration in saline aquifers for geological CO_2 storage," Master's thesis, Massachusetts Institute of Technology, Department of Mechanical Engineering, 2008.

[29] M. Dentz and D. Tartakovsky, "Abrupt-interface solution for carbon dioxide injection into porous media," *Transport in Porous Media*, vol. 79, no. 1, pp. 15–27, 2009.

[30] S. Mathias, P. Hardisty, M. Trudell, and R. Zimmerman, "Approximate solutions for pressure buildup during CO_2 injection in brine aquifers," *Transport in Porous Media*, vol. 79, no. 2, pp. 265–284, 2009.

[31] J. Nordbotten and H. Dahle, "Impact of capillary forces on large-scale migration of CO_2," in *XVIII International Conference on Water Resources, Barcelona, Spain*, pp. 21–24, 2010.

[32] M. Zeidouni, M. Pooladi-Darvish, and D. Keith, "Analytical models for determining pressure change in an overlying aquifer due to leakage," *Energy Procedia*, vol. 4, pp. 3833–3840, 2011.

[33] A. Selvadurai, "Fluid leakage through fractures in an impervious caprock embedded between two geologic aquifers," *Advances in Water Resources*, vol. 41, pp. 76–83, 2012.

[34] E. Kreyszig, *Advanced engineering mathematics*. Wiley: Toronto, ON, Canada, 1999.

[35] S. C. Chapra and R. P. Canale, *Numerical methods for engineers*. McGraw-Hill: Toronto, ON, Canada, 1998.

[36] M. A. Celia, S. Bachu, J. M. Nordbotten, S. E. Gasda, and H. K. Dahle, "Quantitative estimation of CO_2 leakage from geological storage: Analytical models, nu-

merical models and data needs," in *Proceedings of 7th International Conference on Greenhouse Gas Control Technologies*, pp. 663–672, 2004.

[37] J. Nordbotten, D. Kavetski, M. Celia, and S. Bachu, "Model for CO_2 leakage including multiple geological layers and multiple leaky wells," *Environmental Science and Technology*, vol. 43, no. 3, pp. 743–749, 2009.

[38] S. Gasda, J. Nordbotten, and M. Celia, "Vertical equilibrium with sub-scale analytical methods for geological CO_2 sequestration," *Computational Geosciences*, vol. 13, no. 4, pp. 469–481, 2009.

[39] K. Pruess and J. Garcia, "Multiphase flow dynamics during CO_2 disposal into saline aquifers," *Environmental Geology*, vol. 42, no. 2, pp. 282–295, 2002.

[40] A. Riaz and H. Tchelepi, "Dynamics of vertical displacement in porous media associated with CO_2 sequestration," *SPE Journal*, vol. 13, no. 3, pp. 305–313, 2008.

[41] S. Gasda, *Numerical Models for Evaluating CO_2 Storage in Deep Saline Aquifers: Leaky Wells and Large-scale Geological Features*. PhD thesis, Princeton, 2008.

[42] G. Garmeh, R. Johns, and L. Lake, "Pore-scale simulation of dispersion in porous media," *SPE Journal*, vol. 14, no. 4, pp. 559–567, 2009.

[43] J. Neufeld and H. Huppert, "Modelling carbon dioxide sequestration in layered strata," *Journal of Fluid Mechanics*, vol. 625, p. 353, 2009.

[44] P. Humez, P. Audigane, J. Lions, C. Chiaberge, and G. Bellenfant, "Modeling of CO_2 leakage up through an abandoned well from deep saline aquifer to shallow fresh groundwaters," *Transport in Porous Media*, pp. 1–29, 2011.

[45] R. Gracie and J. Craig, "Modelling well leakage in multilayer aquifer systems using the extended finite element method," *Finite Elements in Analysis and Design*, vol. 46, no. 6, pp. 504–513, 2010.

[46] J. Craig and R. Gracie, "Using the extended finite element method for simulation of transient well leakage in multilayer aquifers," *Advances in Water Resources*, vol. 34, no. 9, pp. 1207–1214, 2011.

[47] S. Yin, M. Dusseault, and L. Rothenburg, "Coupled THMC modeling of CO_2 injection by finite element methods," *Journal of Petroleum Science and Engineering*, vol. 80, pp. 53–60, 2012.

[48] R. J. LeVeque, *Finite difference methods for ordinary and partial differential equations: steady-state and time-dependent problems*. Siam: Philadelphia, PA, 2007.

[49] J. Fish and T. Belytschko, *A first course in finite elements*. John Wiley & Sons: Mississauga, ON, Canada, 2007.

[50] G. F. Pinder and W. G. Gray, *Finite element simulation in surface and subsurface hydrology*, vol. 295. Academic Press: New York, NY, 1977.

[51] C. Johnson, *Numerical solution of partial differential equations by the finite element method*. Dover Publications: Mineola, New York, 2009.

[52] K. J. Bathe, *Finite element procedures*. Prentice-Hall: Toronto, ON, Canada, 2006.

[53] O. Zienkiewicz and Z. Taylor, *The finite element method: its basis and fundamentals*. Butterworth-Heinemann: Boston, MA, 2000.

[54] B. Jiang, *The Least-Squares Finite Element Method: Theory and Applications in Computational Fluid Dynamics and Electromagnetics*. Springer: New York, NY, 1998.

[55] T. Belytschko and T. Black, "Elastic crack growth in finite elements with minimal remeshing," *International Journal for Numerical Methods in Engineering*, vol. 45, no. 5, pp. 601–620, 1999.

[56] N. Moes, J. Dolbow, and T. Belytschko, "A finite element method for crack growth without remeshing," *International Journal for Numerical Methods in Engineering*, vol. 46, pp. 131–150, 1999.

[57] J. Chessa, P. Smolinski, and T. Belytschko, "The extended finite element method (XFEM) for solidification problems," *International Journal for Numerical Methods in Engineering*, vol. 53, pp. 1959–1977, 2002.

[58] P. Exner and J. Březina, "Partition of unity methods for approximation of point water sources in porous media," *Applied Mathematics and Computation*, vol. 273, no. C, pp. 21–32, 2016.

[59] J. Bear, "Dynamics of fluids in porous media," *Elsevier: New York, NY*, 1988.

[60] J. Bear, *Hydraulics of groundwater*. Dover: Mineola, NY, 2007.

[61] G. F. Pinder and M. A. Celia, *Subsurface hydrology*. John Wiley & Sons: Hoboken, NJ, 2006.

[62] R. A. Freeze and J. Cherry, *Groundwater*. Prentice-Hall: Englewood Cliffs, NJ, 1979.

[63] M. Hesse, H. Tchelepi, B. Cantwel, and F. Orr, "Gravity currents in horizontal porous layers: transition from early to late self-similarity," *Journal of Fluid Mechanics*, vol. 577, no. 1, pp. 363–383, 2007.

[64] M. Hesse, F. Orr, and H. Tchelepi, "Gravity currents with residual trapping," *Journal of Fluid Mechanics*, vol. 611, no. 1, pp. 35–60, 2008.

[65] R. Helmig, B. Flemisch, M. Wolff, A. Ebigbo, and H. Class, "Model coupling for multiphase flow in porous media," *Advances in Water Resources*, 2012.

[66] M. Preisig and J. H. Prevost, "Coupled multi-phase thermo-poromechanical effects. case study: CO_2 injection at In Salah, Algeria," *International Journal of Greenhouse Gas Control*, vol. 5, no. 4, pp. 1055–1064, 2011.

[67] J. Kim, H. A. Tchelepi, R. Juanes, *et al.*, "Stability, accuracy, and efficiency of sequential methods for coupled flow and geomechanics," *SPE Journal*, vol. 16, no. 2, pp. 249–262, 2011.

[68] H. Stone and A. Garder Jr, "Analysis of gas-cap or dissolved-gas drive reservoirs," *SPE Journal*, vol. 1, no. 2, pp. 92–104, 1961.

[69] J. Rutqvist, D. Vasco, and L. Myer, "Coupled reservoir-geomechanical analysis of CO_2 injection and ground deformations at In Salah, Algeria," *International Journal of Greenhouse Gas Control*, vol. 4, no. 2, pp. 225–230, 2010.

[70] B. Orlic, J. ter Heege, and B. Wassing, "Assessing the integrity of fault and top seals at CO_2 storage sites," *Energy Procedia*, vol. 4, pp. 4798–4805, 2011.

[71] J. Donea and A. Huerta, *Finite element methods for flow problems*. John Wiley & Sons: Etobicoke, ON, Canada, 2003.

[72] O. Zienkiewicz, R. Taylor, and P. Nithiarasu, *The Finite Element Method for Fluid Dynamics*. Elsevier: Boston, MA, 2005.

[73] A. N. Brooks and T. J. Hughes, "Streamline upwind/Petrov-Galerkin formulations for convection dominated flows with particular emphasis on the incompressible Navier-Stokes equations," *Computer Methods in Applied Mechanics and Engineering*, vol. 32, no. 1, pp. 199–259, 1982.

[74] G. Carey and B. Jiang, "Least-squares finite element method and preconditioned conjugate gradient solution," *International Journal for Numerical Methods in Engineering*, vol. 24, no. 7, pp. 1283–1296, 1987.

[75] G. Carey and B. Jiang, "Least-squares finite elements for first-order hyperbolic systems," *International Journal for Numerical Methods in Engineering*, vol. 26, no. 1, pp. 81–93, 1988.

[76] B. Jiang and L. Povinelli, "Least-squares finite element method for fluid dynamics," *Computer Methods in Applied Mechanics and Engineering*, vol. 81, no. 1, pp. 13–37, 1990.

[77] T. J. Hughes, "Multiscale phenomena: Green's functions, the Dirichlet-to-Neumann formulation, subgrid scale models, bubbles and the origins of stabilized methods," *Computer Methods in Applied Mechanics and Engineering*, vol. 127, no. 14, pp. 387–401, 1995.

[78] T. J. Hughes, G. R. Feijo, L. Mazzei, and J. B. Quincy, "The variational multiscale methoda paradigm for computational mechanics," *Computer Methods in Applied Mechanics and Engineering*, vol. 166, no. 12, pp. 3–24, 1998.

[79] T. J. Hughes, L. P. Franca, and G. M. Hulbert, "A new finite element formulation for computational fluid dynamics: VIII. the Galerkin/least-squares method for advective-diffusive equations," *Computer Methods in Applied Mechanics and Engineering*, vol. 73, no. 2, pp. 173–189, 1989.

[80] I. Christie, D. F. Griffiths, A. R. Mitchell, and O. C. Zienkiewicz, "Finite element methods for second order differential equations with significant first derivatives," *International Journal for Numerical Methods in Engineering*, vol. 10, no. 6, pp. 1389–1396, 1976.

[81] J. C. Heinrich, P. S. Huyakorn, O. C. Zienkiewicz, and A. R. Mitchell, "An upwind finite element scheme for two-dimensional convective transport equation," *International Journal for Numerical Methods in Engineering*, vol. 11, no. 1, pp. 131–143, 1977.

[82] J. Donea, "A Taylor Galerkin method for convective transport problems," *International Journal for Numerical Methods in Engineering*, vol. 20, no. 1, pp. 101–119, 1984.

[83] C. Baiocchi, F. Brezzi, and L. P. Franca, "Virtual bubbles and Galerkin-least-squares type methods (Ga.L.S.)," *Computer Methods in Applied Mechanics and Engineering*, vol. 105, no. 1, pp. 125–141, 1993.

[84] E. Onate, "Derivation of stabilized equations for numerical solution of advective-diffusive transport and fluid flow problems," *Computer Methods in Applied Mechanics and Engineering*, vol. 151, no. 12, pp. 233–265, 1998.

[85] W. H. Reed and T. Hill, "Triangular mesh methods for the neutron transport equation," *Los Alamos Report LA-UR-73-479*, 1973.

[86] T. J. Hughes and A. N. Brooks, "A multidimensional upwind scheme with no cross-wind diffusion," *Finite Element Methods for Convection Dominated Flows, AMD*, vol. 34, pp. 19–35, 1979.

[87] F. Shakib, T. J. Hughes, and Z. Johan, "A new finite element formulation for computational fluid dynamics: X. The compressible Euler and Navier-Stokes equations," *Computer Methods in Applied Mechanics and Engineering*, vol. 89, no. 13, pp. 141–219, 1991.

[88] A. Soulamani and M. Fortin, "Finite element solution of compressible viscous flows using conservative variables," *Computer Methods in Applied Mechanics and Engineering*, vol. 118, no. 34, pp. 319–350, 1994.

[89] R. Codina, "Comparison of some finite element methods for solving the diffusion-convection-reaction equation," *Computer Methods in Applied Mechanics and Engineering*, vol. 156, no. 14, pp. 185–210, 1998.

[90] M. Sarkarfarshi, F. A. Malekzadeh, R. Gracie, and M. B. Dusseault, "Parametric sensitivity analysis for CO_2 geosequestration," *International Journal of Greenhouse Gas Control*, vol. 23, pp. 61–71, 2014.

[91] F. Shakib and T. J. Hughes, "A new finite element formulation for computational fluid dynamics: IX. Fourier analysis of space-time Galerkin/least-squares algorithms," *Computer Methods in Applied Mechanics and Engineering*, vol. 87, no. 1, pp. 35–58, 1991.

[92] S. Canada, "http://www.shell.ca/en/aboutshell/our-business-tpkg/upstream/oil-sands/quest/technology.html."

[93] R. Ghosh, M. K. Sen, and N. Vedanti, "Quantitative interpretation of CO_2 plume from sleipner (north sea), using post-stack inversion and rock physics modeling," *International Journal of Greenhouse Gas Control*, vol. 32, pp. 147 – 158, 2015.

[94] H. Class, L. Mahl, W. Ahmed, B. Norden, M. Kuhn, and T. Kempka, "Matching pressure measurements and observed CO_2 arrival times with static and dynamic modelling at the ketzin storage site," *Energy Procedia*, vol. 76, pp. 623–632, 2015.

[95] P. Bergmann, M. Diersch, J. Gtz, M. Ivandic, A. Ivanova, C. Juhlin, J. Kummerow, A. Liebscher, S. Lth, S. Meekes, B. Norden, C. Schmidt-Hattenberger, F. M. Wagner, and F. Zhang, "Review on geophysical monitoring of CO_2 injection at ketzin, germany," *Journal of Petroleum Science and Engineering*, vol. 139, pp. 112 – 136, 2016.

[96] T. Belytschko, R. Gracie, and G. Ventura, "A review of extended/generalized finite element methods for material modeling," *Modelling and Simulation in Materials Science and Engineering*, vol. 17, no. 4, p. 043001, 2009.

[97] T. P. Fries and T. Belytschko, "The extended/generalized finite element method: an overview of the method and its applications," *International Journal for Numerical Methods in Engineering*, vol. 84, no. 3, pp. 253–304, 2010.

[98] S. Pommier, A. Gravouil, N. Moes, and A. Combescure, *Extended finite element method for crack propagation*. Wiley: Hoboken, NJ, 2013.

[99] S. Mohammadi, *XFEM Fracture Analysis of Composites*. Wiley: West Sussex,UK, 2012.

[100] J. Dolbow, N. Moës, and T. Belytschko, "Modeling fracture in Mindlin–Reissner plates with the extended finite element method," *International Journal of Solids and Structures*, vol. 37, no. 48, pp. 7161–7183, 2000.

[101] Z. Liu, T. Menouillard, and T. Belytschko, "An XFEM/spectral element method for dynamic crack propagation," *International Journal of Fracture*, vol. 169, no. 2, pp. 183–198, 2011.

[102] T. Menouillard and T. Belytschko, "Smoothed nodal forces for improved dynamic crack propagation modeling in XFEM," *International Journal for Numerical Methods in Engineering*, vol. 84, no. 1, pp. 47–72, 2010.

[103] H. Nguyen-Vinh, I. Bakar, M. Msekh, J. Song, J. Muthu, G. Zi, P. Le, S. Bordas, R. Simpson, S. Natarajan, *et al.*, "Extended finite element method for dynamic fracture of piezo-electric materials," *Engineering Fracture Mechanics*, vol. 92, pp. 19–31, 2012.

[104] M. Holl, S. Loehnert, and P. Wriggers, "An adaptive multiscale method for crack propagation and crack coalescence," *International Journal for Numerical Methods in Engineering*, vol. 93, no. 1, pp. 23–51, 2013.

[105] P. Aubertin, J. Rethore, and R. de Borst, "Dynamic crack propagation using a combined molecular dynamics/extended finite element approach," *International Journal for Multiscale Computational Engineering*, vol. 8, no. 2, pp. 72–88, 2010.

[106] R. Gracie and T. Belytschko, "An adaptive concurrent multiscale method for the dynamic simulation of dislocations," *International Journal for Numerical Methods in Engineering*, vol. 86, no. 4-5, pp. 575–597, 2011.

[107] J. Oswald, E. Wintersberger, G. Bauer, and T. Belytschko, "A higher-order extended finite element method for dislocation energetics in strained layers and epitaxial islands," *International Journal for Numerical Methods in Engineering*, vol. 85, no. 7, pp. 920–938, 2011.

[108] X. Liu, H. Waisman, and J. Fish, "A new crack tip enrichment function in the extended finite element method for general inelastic materials," *International Journal for Multiscale Computational Engineering*, vol. 10, no. 4, pp. 343–360, 2012.

[109] O. Skiba, R. Gracie, and S. Potapenko, "Electromechanical simulations of dislocations," *Modelling and Simulation in Materials Science and Engineering*, vol. 21, no. 3, pp. 35003–35018, 2013.

[110] J. Chessa and T. Belytschko, "An extended finite element method for two-phase fluids," *Journal Of Applied Mechanics-Transactions of the ASME*, vol. 70, no. 1, pp. 10–17, 2003.

[111] K. Cheng and T. P. Fries, "XFEM with hanging nodes for two-phase incompressible flow," *Computer Methods in Applied Mechanics and Engineering*, vol. 245246, pp. 290–312, 2012.

[112] H. Sauerland and T. P. Fries, "The stable XFEM for two-phase flows," *Computers and Fluids*, vol. 87, pp. 41–49, 2013.

[113] T. Mohammadnejad and A. Khoei, "An extended finite element method for fluid flow in partially saturated porous media with weak discontinuities; the convergence analysis of local enrichment strategies," *Computational Mechanics*, vol. 51, no. 3, pp. 327–345, 2013.

[114] T. P. Fries, "A corrected XFEM approximation without problems in blending elements," *International Journal for Numerical Methods in Engineering*, vol. 75, no. 5, pp. 503–532, 2008.